X-ray Study of Heavy Element Evolution in Hot Plasmas Associated with Clusters of Galaxies
(X線による銀河団ガス中の重元素進化の研究)

Yuya Shimoda

Department of Physics, Graduate School of Science and Engineering,
Saitama University,
255 Shimo-Okubo, Sakura, Saitama 338-8570, Japan

February 10, 2014

Abstract

Clusters of galaxies are the largest virialized structures in the universe, and the intracluster medium (ICM) keeps the information since the early universe. Especially, the gravitationally bounded thermal hot plasmas have been enriched with metals (such as Ne, Mg, Si, S, Fe, Ni) having been synthesized in stars and supernovae in the member galaxies. This study conducts a systematic analysis of the metal abundances in the ICM of 62 clusters of galaxies ($0.02 < z < 1.16$) with the Japanese X-ray observatory *Suzaku*. *Suzaku* provides a good sensitivity for the atomic lines in the X-ray spectra with the good line spread function and low particle background level. All clusters of galaxies in the presented sample are also observed with *Chandra*, the X-ray observatory developed and launched by the United States.

Employing the excellent spatial resolution capability of the *Chandra*, contaminant sources are identified and subtracted from the field of view of *Suzaku*. Thus carefully analyzed X-ray spectra revealed that iron abundance in the ICM are almost constant value, ~ 0.5 solar abundance. On the other hand, α elements (such as Ne, Mg, Si, and S) abundance range $0.4 < \alpha$ elements abundance < 1.0. Since ~ 0.3 solar abundance of each elements is realized in nearby ICMs, this discrepancy suggests that iron family elements and α elements have enriched in different paths.

By comparison of various correlation study between the metal abundances and parameters thought to trace the age of clusters of galaxies, such as redshift, temperature, total gravitational mass, Abell's richness classes, Bautz-Morgan type, and galaxy luminosity, it is shown that α elements abundance increase as a function of the size of the system (age of the system). The large end system among the presented sample shows two times larger α elements abundance than that of the small end of the sample. On the other hand, iron abundance shows negative trend toward larger systems by $\sim 30\%$. In addition to those, the status resolved metal abundances study requires significant discrepancy between relaxed (cool core/AGN) and merging (non-cool core/non-AGN) type cluster of galaxies.

According to the observed results, the metal enrichment history is to be concluded as follows: SN Ia products enriched the ICM mostly at $z > 1$ for the relaxed clusters and exhibit almost constant metal abundance of $Z_{\rm Fe} \sim 0.5$, while those of the merging clusters increases even in $z < 1$ because of the possible continuous starburst activity; The large abundance of SN II are observed in the larger clusters. It suggests that the product elements escape from shallower potentials of smaller systems; The redshift dependence of SN II products are not clearly observed because of our selection bias. Above scenario explains well the observed results that the α elements abundance are proportional to the size of clusters while Fe abundance are almost constant value according to the size of systems.

Contents

List of Tables

List of Figures

Chapter 1

INTRODUCTION

Clusters of galaxies are the largest virialized structures in the universe, and they gravitationally bind hot thin-thermal plasma (intracluster medium; ICM). The main part of the ICM is H and He which were produced by recombination. The high temperature reaching up to several 10^7 K makes the ICM to produce X-rays via thermal bremsstrahlung. The ICM is enriched with metals having been synthesized in stars and supernova (SN) explosions to be injected into the intra-galactic space by SN explosions (e.g. Arnaud et al.(1992); Renzini et al. 1993). The metals produced in galaxies are thought to be exported to the ICM via galaxy wind (Mathews & Baker 1971) and/or ram pressure stripping (Gunn & Gott 1972). These metals are highly ionized in collisional ionization equilibrium and the excited metal ions emit atomic lines in the X-ray range.

The majority of supernovae are classified into type Ia (SN Ia) or core collapse type (SN cc). The former is the explosion of a white dwarf with gas accretion from the companion star, in which nuclides are in the thermal equilibrium and provides a lot of iron family elements (Iwamoto et al. 1999). In the latter the iron core of a massive star are photodisintegrated into helium nuclei and mainly alpha elements are synthesized in the explosion (Nomoto et al. 2006). Thus the emission line properties observed in the X-ray spectrum reflect integrated activities of both types of supernovae in the galaxies, and enable us to study chemical enrichment evolution history of the ICM, which is a major component of the known baryon in the universe. The metal abundances to H in the ICM are measured from X-ray spectrum comparing line emissions with thermal bremsstrahlung emission.

Observational studies of the ICM metals were greatly advanced by *ASCA* (Tanaka, Inoue, & Holt 1994), in particular, in measuring the spatial distributions of the metals such as Si and Fe in the ICM (Ezawa et al. 1997; Fukazawa et al. 1998, 2000; Finoguenv et al. 2000, 2001). Recently, *XMM-Newton* and *Chandra*, thanks to their large effective areas and high angular resolutions, have expanded the metal abundance study to higher redshift clusters, where the metal abundance is mainly determined by using Fe-L and Fe-K lines. Using *XMM-Newton* and *Chandra* data of 56 clusters at $0.3 \leq z \leq 1.3$, Balestra et al. (2007) measured the iron abundance $Z_{\rm Fe}$ within a spatial region of 0.15 r_{200} – 0.3 r_{200}. They found that the clusters at $z > 0.5$ exhibit similar abundance of $Z_{\rm Fe} \approx 0.25$ solar, while clusters at $z < 0.5$ exhibit a significantly larger abundance of $Z_{\rm Fe} \approx 0.4$ solar.

Maughan et al. (2008) also reported the same trend using 115 clusters at $0.1 < z < 1.3$ observed with *Chandra*. They found significant evolution in the metal abundance which drops by 50% from $z = 0.1$ to $z \sim 1$. Anderson et al. (2009) found the similar drop in the metal abundance from $z = 0.1$ to $z \sim 1$ using 29 clusters observed with *XMM-Newton*, together with the 115 clusters of Maughan et al. (2008) and 70 clusters at $z < 0.3$ in Snowden et al. (2008). Baldi et al. (2012) tried to reveal the expected dependence of the metal evolution on distance from the center by spatially resolved analysis, but they obtained no statistically significant conclusion about the different evolutionary path that the different regions of the clusters may have traversed.

After the launch of *Suzaku* (Mitsuda et al. 2007), studies of alpha elements have been promoted. The X-ray Imaging Spectrometer (XIS: Koyama et al. 2007) onboard *Suzaku* has good sensitivity for lines in lower energies thanks to good line spread function and low particle background level (section 3.1.4). The metal abundances synthesized mainly in SNe cc, such as Mg, Si and S, in the ICM outside cool-core regions up to $\sim 0.3\ r_{200}$ have been measured for several nearby clusters and groups ($z \sim 0.001$) with *Suzaku* (Matsushita et al. 2007; Komiyama et al. 2009; Sato et al. 2007a, 2008, 2009a, 2010; Sakuma et al. 2011). Combining the *Suzaku* results with SNe nucleosynthesis model, Sato et al. (2007b) calculated integrated numbers of SNe Ia and SNe cc explosions in nearby clusters. They showed that the number ratio of SNe cc to Ia is ~ 3.5 and Fe has been synthesized predominantly by SNe Ia. A similar result is reported in de Plaa et al. (2007) using data of *XMM-Newton*.

In order to conclude the metal enrichment history of the ICM observationally, it is crucial to measure metal abundances of α elements and iron families separately in clusters at high redshifts. This is beyond the ability of X-ray observatories currently in orbit, and would be one of major sciences in future X-ray missions with huge effective areas. However, *Suzaku* has the ability to pilot that survey for bright sources at medium redshifts.

In this paper, we report results of *Suzaku* observation of the cluster of galaxies. Throughout this paper, cosmological parameters of $H_0 = 71$ km s^{-1} Mpc^{-1}, $\Omega_{\rm M} = 0.27$, and $\Omega_\Lambda = 0.73$ are adopted. The virial radius is by substituting the average temperature (table B.1) into equation 2 of Henry et al. (2009), the results of virial radius is listed in table B.1 where the virial radius r_{200} is the radius within which the average density is 200 times the critical density at the redshift of the cluster. The Galactic hydrogen column density in the direction of clusters is taken from Dickey & Lockman 1990 and summarized in table B.1. The definition of one solar abundance is taken from Lodders (2003). Errors are given at the 90% confidence level unless otherwise stated.

Chapter 2

REVIW OF METAL ENRICHMENT HISTORY

2.1 Overview

Clusters of galaxies contain hundreds of galaxies, spreading over the size of ∼Mpc, have a total mass of $\sim 10^{14} M_{\odot}$. They were firstly studied in detail by Wolf (1906), and X-ray emission from the Virgo cluster was discovered in 1966 (e.g. Byram et al. 1966).

The two most famous catalogs of rich clusters of galaxies are compiled by Abell et al. (Abell 1958; Abell, Corwin, Olowin 1989) and Zwicky et al. (1961–1968). These catalogs contain a few thousand clusters. Over the last 10 years, the numbers of identified clusters of galaxies has increased up to several tens of thousands by utilizing the advanced optical CCD cameras (e.g. Sloan Digital Sky Survey: SDSS) and advanced X-ray sky surveys (e.g. *Rosat* All Sky Survey: RASS). In this century, deep X-ray surveys by *Chandra* and *XMM-Newton* have added the distant clusters of galaxies ($z > 1$) by utilizing their excellent sensitivity.

2.2 Optical Properties of Clusters of Galaxies

2.2.1 Velocity distribution

The redshift of each cluster of galaxies is determined by the mean radial velocity which is the line of sight component of member galaxies. On the other hand, the gravitational potential of each cluster of galaxies are characterized by the standard deviation of the radial velocities (or velocity dispersion) of member galaxies, which is defined as

$$\sigma_r = \langle (v_r - \langle v_r \rangle)^2 \rangle^{1/2}, \tag{2.1}$$

where v_r is the radial velocity of each member galaxy. Assuming virial equilibrium of the system, virial mass is derived from σ_r as

$$\begin{aligned} M_{\rm virial} &= \frac{3\pi}{2G}\sigma_r^2 R \\ &\sim 10^{15}\ M_{\odot} \left(\frac{\sigma_r}{10^3\ {\rm km/s}}\right)^2 \left(\frac{R}{\rm Mpc}\right), \end{aligned} \tag{2.2}$$

Table 2.1: Cluster population and richness classes (Abell 1958).

Population	Class	Population	Class
30–49	0	130–199	3
50–79	1	200–299	4
80–129	2	300 $\leq$	5

where R is the radius of clusters and G is the gravitational constant. Using a typical velocity dispersion of galaxies and radius of cluster, the typical total mass (including stellar, ICM, and dark matter) become $10^{15} M_{\odot}$. The crossing time of typical galaxy in a cluster indicates a lower limit to the relaxation time, and is derived as

$$\begin{aligned} t_{\rm cross} &= \frac{2R}{\sqrt{3}\sigma_r} \\ &\sim 10^9 \text{ yr} \left(\frac{\sigma_r}{10^3 \text{ km/s}} \right)^{-1} \left(\frac{R}{\text{Mpc}} \right). \end{aligned} \tag{2.3}$$

Hence, a typical clusters of galaxies can become dynamically relaxed within the Hubble time ($\sim$ 13.7 Gyr). Physical quantity — such as clusters radius and velocity dispersion — in the above equations are derived from optical observations.

2.2.2 Morphology

Several schemes have been used to classify clusters of galaxies, based on their optical morphology including the spatial and magnitude distributions of their member galaxies. Among them, Bautz–Morgan type (B–M type; Bautz & Morgan 1970) is one of commonly used classifications. The B–M system classifies clusters into three types by the degree of domination by bright galaxies. B–M type I is assigned to those clusters in which a single central cD galaxy, which is very bright and huge elliptical galaxy, dominates. B–M type II clusters host brightest galaxies which are not a cD, but intermediate between cD's and ordinary giant ellipticals. B–M type III clusters have no dominating galaxies. Classifications of type I–II and type II–III are also used for intermediate objects.

2.2.3 Richness

Richness means the galaxy populations of the cluster. Abell (1958) defined the Abell's richness classes for the statistical study of clusters of galaxies. Galaxy count versus richness class is shown in table 2.1. Abell's richness classes are useful to estimate the scale of the clusters of galaxies.

2.3 Properties of Intracluster Medium

2.3.1 X-ray emission mechanism

The high temperature reaching up to several 10^7 K make the ICM to produce X-rays via thermal bremsstrahlung (free-free) emission with line emission from heavy elements. The emissivity of the

bremsstrahlung radiation at a frequency of ν from a hot plasma with an electron temperature of $T_{\rm e}$ is given by

$$\epsilon_\nu = \frac{2^5\pi {\rm e}^6}{3m_{\rm e}c^3}\left(\frac{2\pi}{2m_{\rm e}k}\right)^{1/2} n_{\rm e}\sum_i Z_i^2 n_i g_{ff}(T_{\rm e},Z,\nu)\times T_{\rm e}^{-1/2}\exp(-h\nu/kT_{\rm e}), \quad (2.4)$$

where Z_i and n_i are the charge and number density of the ion i, respectively, and $n_{\rm e}$ is the electrons number density (e.g. Rybichi & Lightman 1979). The Gaunt factor, g_{ff}, is a correction factor for quantum mechanical effects and is approximately $g_{ff}\sim 0.9(h\nu/kT)^{-0.3}$. Thus, the emissivity in a given bandpass, $\nu_1<\nu<\nu_2$, is then

$$\epsilon^{ff} = \int_{\nu_1}^{\nu_2} e_\nu^{ff} d\nu \quad (2.5)$$

$$= \Lambda(T,Z)n_{\rm e}^2 \quad (2.6)$$

The $\Lambda(T,Z)$ is the cooling function, with T and Z representing the plasma temperature and the heavy element abundance, respectively (e.g. Sutherland & Dopita 1993).

If we assume that ICM has a spatially-uniform temperature and abundance in the volume V, and that the ICM density is constant over the sky area, then the X-ray luminosity $L_{\rm X}$ is given as

$$L_{\rm X} = \int_{\nu_1}^{\nu_2}\epsilon^{ff}dV \quad (2.7)$$

$$= \Lambda(T,Z)\int_{\nu_1}^{\nu_2} n_{\rm e}^2 dV. \quad (2.8)$$

According to above discussion, X-ray spectrum is described by bremsstrahlung with emission of atomic lines. Since the temperature of the ICM is same order as the K-shell ionization potentials of heavy elements such as O, Ne, Mg, Si, S, Fe, and Ni, these elements become mainly He-/H-like ions or completely ionized. These ions are collisionally excited, and emit their K-lines. X-ray spectra for various temperature is shown in figure 2.1.

The emission lines and continuum spectra form the ionization equilibrium plasma have been calculated by various authors (e.g. Raymond & Smith 1977: *raymond*; Kaastra & Mewe 1993: *mekal*). We utilize the *apec* code v1.2.0 (Smith et al. 2001), which reproduces emission spectra from collisionally-ionized diffuse gas, included in the XSPEC data analysis package in this thesis.

The value of metal abundances of model fitting is described by solar abundance unit. One solar abundance is defined such that the number ratios of elements to that of hydrogen is the same as the solar composition. The definition of solar composition is however ambiguous to some extent, because some use data from the solar photosphere, and others refer to those determined from meteorites (e.g. Anders & Grevesse 1989; Grevesse & Sauval 1998; Lodders 2003). In this paper we adopt the photospheric values from Lodders (2003), which is the latest ones of the solar composition.

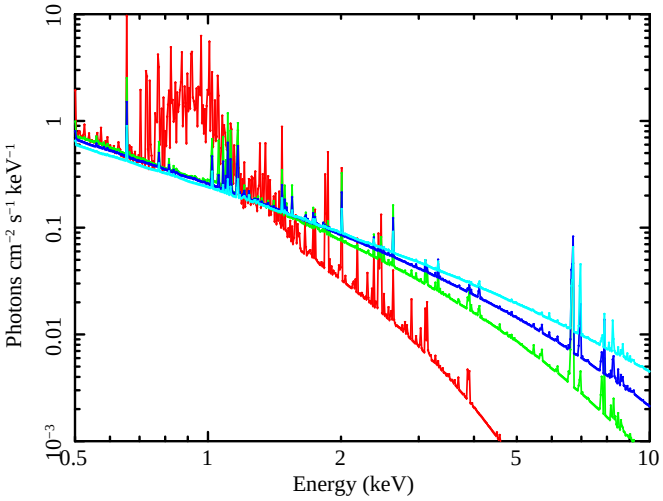

Figure 2.1: Calculated X-ray spectra from optically thin thermal plasma using *apec* code. A metal abundance are fixed to 0.5 $Z_{\rm solar}$. Red, green, blue and cyan show the $kT = 1, 3, 5, 9$ keV thermal plasma.

2.3.2 Hydrostatic equilibrium

Since the collision time scales for ions and electrons in the ICM are much shorter than the time scales of heating or cooling, we can treat the gas as fluid (Sarazin 1988). In general, the time required for a sound wave in the ICM to cross a cluster is shorter than the probable age of a cluster. Thus the gas is considered to be in hydrostatic equilibrium. In addition, if the cluster is spherically distributed, the hydrostatic equation leads

$$\frac{dP_{\rm gas}}{dr} = -\mu n_{\rm gas} m_{\rm p} \frac{d\phi}{dr}, \tag{2.9}$$

where $P_{\rm gas}$ is the ICM pressure, r is the three dimensional radius, $\mu = 0.62$ is the mean molecular weight, $n_{\rm gas}$ is the number density including electrons and ions, $m_{\rm p}$ is the proton mass, and ϕ is the gravitational potential. Because of the low density ($n_{\rm gas} < 10^{-2}$ cm^{-3}), the ICM can be treated as an ideal gas that follows the equation of state as

$$P_{\rm gas} = n_{\rm gas} k T_{\rm gas}. \tag{2.10}$$

Then, assuming the hydrostatic equilibrium and using equation 2.10, the total gravitational mass within r is given by

$$M(<r) = -\frac{r^2}{\mu n_{\rm gas} m_{\rm p} G} \frac{dP_{\rm gas}}{dr} \tag{2.11}$$

$$= -\frac{k T_{\rm gas} r}{\mu m_{\rm p} G} \left(\frac{d \ln \rho_{\rm gas}}{d \ln r} + \frac{d \ln T_{\rm gas}}{d \ln r} \right). \tag{2.12}$$

Where $\rho_{\rm gas}$ is the gas density which can be written as $\rho_{\rm gas} = \mu n_{\rm gas} m_{\rm p}$ and G is the gravitational constant.

2.3.3 β-model

Here, I rewrite the hydrostatic equilibrium equation assuming constant temperature,

$$\frac{d\ln n_{\rm gas}}{dr} = -\frac{\mu m_{\rm p}}{kT_{\rm gas}}\frac{d\phi}{dr}. \tag{2.13}$$

Assuming the hydrostatic equilibrium as well as the ICM, the hydrostatic equation of the galaxies is written as,

$$\frac{d\ln n_{\rm gal}}{dr} = -\frac{1}{\sigma^2}\frac{d\phi}{dr}, \tag{2.14}$$

where $n_{\rm gal}$ is the number density of the member galaxies. From equations 2.13 and 2.14, we find

$$n_{\rm gas} \propto n_{\rm gal}^{\beta}, \tag{2.15}$$

where β is an energy ratio between ICM and gravitational matter in the unit mass and defined as

$$\beta \equiv \frac{\mu m_{\rm p}\sigma^2}{kT_{\rm gas}} = 0.751\left(\frac{\sigma}{10^3{\rm km/s}}\right)^2\left(\frac{T_{\rm gas}}{10^8{\rm K}}\right)^{-1}. \tag{2.16}$$

King (1962) has derived an analytic approximation to the isothermal sphere of self-gravitational isothermal collisionless particles. The density profiles of galaxies have been found to be well approximated with the King profile,

$$\rho_{\rm gal} \sim \rho_{\rm King} = \rho_{0,\rm gal}\left(1+\left(\frac{r}{r_{\rm core}}\right)^2\right)^{-\frac{3}{2}}, \tag{2.17}$$

where $\rho_{\rm gal}$ is the galaxy density. Then the isothermal gas distribution may be represented as

$$\rho_{\rm gas} = \rho_{0,\rm gas}\left(1+\left(\frac{r}{r_{\rm core}}\right)^2\right)^{-\frac{3}{2}\beta}. \tag{2.18}$$

The surface brightness profile of an isothermal spherical plasma with a radial density profile given by equation 2.18 is calculated by integrating the local emission per unit volume given by equation 2.6 and the density along the line of sight. We obtain the X-ray surface brightness S at a projected radius r,

$$S = S_0\left(1+\left(\frac{r}{r_{\rm core}}\right)^2\right)^{-3\beta+\frac{1}{2}} \tag{2.19}$$

$$S_0 \equiv n_{0,\rm e}n_{0,\rm H}\Lambda(T,Z)\frac{\sqrt{\pi}r_{\rm core}}{4\pi D_{\rm L}^2}\frac{\Gamma(3\beta-1/2)}{\Gamma(3\beta)}. \tag{2.20}$$

It is known that the observed cluster X-ray surface brightness is well fitted with the above function with the average β value of ~ 0.7 (e.g. Jones & Forman 1984).

For some clusters, systematic residuals are seen in the results of single β-model fitting. The excess component is often represented by another β-model component (Jones & Forman 1984; Xu et al. 1998; Mohr et al. 1999). In this case, We used the double β-model composed of different core radii and β value,

$$S = \sum_{i=1}^{2} S_i\left(1+\left(\frac{r}{r_{{\rm core},i}}\right)^2\right)^{-3\beta_i+\frac{1}{2}}. \tag{2.21}$$

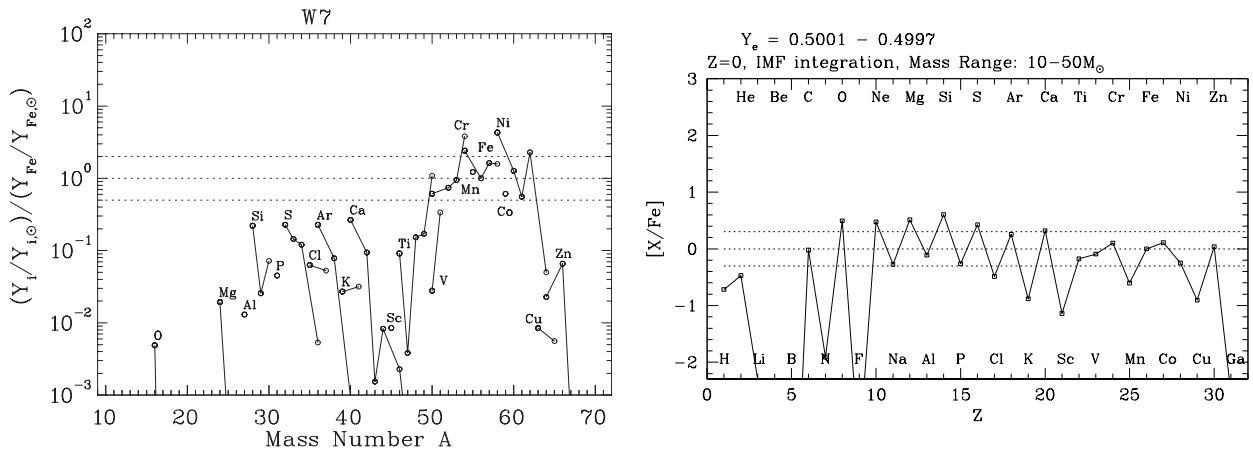

Figure 2.2: left: Calculated nucleosynthesis yields of various elements for SN Ia using W7 model (Iwamoto et al. 1999). right: The same as the left panel, but for SN cc (Nomoto et al. 2006).

2.3.4 The origin of metals

The ICM is enriched with metals having been synthesized in the Big Bang, stars and SN explosions and ejected to the intra-galactic space by SN explosions (e.g. Arnaud et al. 1992; Renzini et al. 1993). These processes have been studied theoretically and observationally. The majority of supernovae are classified into SN Ia (e.g. Iwamoto et al. 1999; Travaglio et al. 2004), and SN cc (including SN Ib, Ic, II; e.g. Nakamura et al. 2001; Nomoto et al. 2006) (detailed in Chapter 1). Here, core collapse are classified based on the optical spectra as follows. SNe II are defined by the presence of hydrogen, which implies that the progenitors are red (or blue) supergiants keeping their hydrogen-rich envelope. SNe Ib are characterized by the lack of hydrogen but the presence of prominent He lines, so that their progenitors are Wolf-Rayet or He stars losing their H-rich envelope in a stellar wind or by Roche lobe overflow in binary systems. SNe Ic show no prominent He lines as well as H, which implies that their progenitors have lost even most of He layers to become WC/WO Wolf-Rayet stars or C+O stars in binary systems.

The metals are highly ionized in collisional ionization equilibrium and excited metal ions emit atomic lines in the X-ray range (section 2.3.1). Thus the emission lines observed in the X-ray spectrum reflect integrated activities of both types of supernovae in the galaxies, and enable us to study chemical enrichment history of the ICM, which is a major component of the known baryon in the universe.

2.3.5 Metal transportation

The metals in galaxies are thought to be exported to the ICM. The possible transport processes of the metals to the ICM include three mechanisms; galaxy wind (Mathews & Baker 1971), gas stripping from ram-pressure (Gunn & Gott 1972) and galaxy-galaxy interactions (e.g. Clemens et al. 2000; Mihos et al. 2005), and the Active Galactic Nuclei (AGN) outflows. Further processes like a effect of an intra-cluster stellar population (e.g. Arnaboldi 2004) might also contribute a small

fraction to the metal enrichment of the ICM.

The galactic winds are observed as outflows of interstellar gas with velocities of 10^{1-2} km s^{-1}. The interaction of galaxies is occurred when another galaxy pass the close area of the galaxy, and can trigger a starburst which subsequently can lead to a galactic wind.

As a galaxy is passing through the ICM, it feels an external pressure. Consequently, gas is stripped off the galaxy. This process depends on the pressure of the ICM, the relative velocity of ICM and galaxy, and the depth of the potential of the galaxy. Galactic winds are driven by thermal energy which are provided from repeated supernova explosions. The amount of metals transported depends on various galaxy parameters: total mass of the galaxy, the disk scale length, and the environmental conditions.

There are two types of AGN outflows. One of them is jet consisting of relativistic particles. The jets can entrain some of the surrounding metal-rich gas (De Young 1986). The other is winds-like outflow which are estimated to have a high metallicity of a few times solar (Hasinger et al. 2002), high velocities of several thousands of km/s (Chartas et al. 2002) and considerable mass outflow rates of several $10^9 M_{\rm solar}$ (Crenshaw et al. 2003; Veilleux et al. 2005; Nesvadba et al. 2006).

2.3.6 Metals in the ICM

Since strong Fe-K line emission from the ICM was discovered in rich clusters by early X-ray observations (e.g. Mitchell et al 1976 with *Ariel 5*), the study of metals in the ICM has proceeded steadily. *Tenma*, Japanese second X-ray observatory, clearly detected Fe-K$_\alpha$ (6.7 keV) and Fe-K$_\beta$ (7.9 keV) lines separately from the Perseus, Ophiuchus, and Coma clusters (Okumura et al. 1988). *Ginga*, Japanese third X-ray observatory, found evidence that Fe in the ICM is more abundant in a central region of the Virgo cluster (Koyama et al. 1991). This Fe concentration indicates that the central ICM may have been enriched by mass loss from the central galaxy M 87.

Observational studies of metals in the ICM were greatly promoted by *ASCA*, which is Japanese forth X-ray observatory. The spatial distribution measurement of Si and Fe in the ICM (e.g. Finoguenv et al. 2000, 2001) has revealed Fe concentration at the central region (three times larger than outer region) in the Centaurus cluster (Fukazawa et al. 1994), as described in Chapter 1, or relatively moderate large-scale Fe gradient in the AWM 7. According to a number of observations of clusters, the $Z_{\rm Fe}$ generally declines from $\sim$0.5 $Z_{\rm solar}$ at the center to < 0.2 $Z_{\rm solar}$ at the 500 kpc (Ezawa et al. 1997; Fukazawa et al. 2000). Especially, this tendency is remarkable for clusters with single cD galaxies at their center.

$Z_{\rm Si}$ is important in that considerable portion of it is considered to have been provided via SN cc. Thus, by comparing $Z_{\rm Si}$ and $Z_{\rm Fe}$, we can estimate the relative contribution of SN Ia and SN cc to the metal enrichment of the ICM. Fukazawa et al. (1998) analyzed 40 nearby ($z < 0.062$) clusters of galaxies with various degrees of richness with *ASCA*. They found that spatially averaged $Z_{\rm Fe}$ is mostly concentrated in a range of 0.2–0.3 $Z_{\rm solar}$, regardless of temperature of the ICM, while $Z_{\rm Si}$

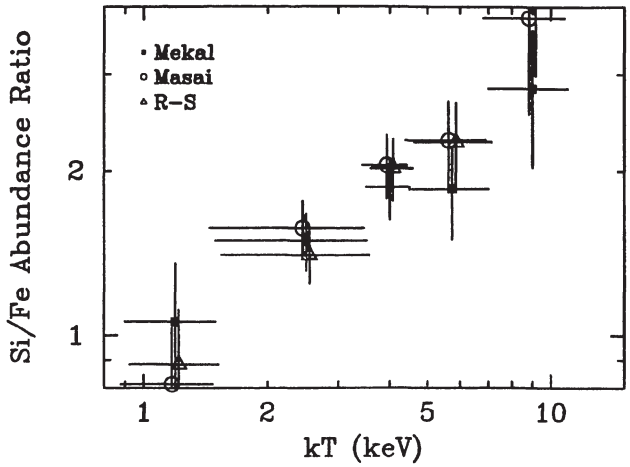

Figure 2.3: $Z_{\rm Si}/Z_{\rm Fe}$ ratios averaged over clusters with similar temperatures, plotted as a function of the ICM temperature. The different symbols denote different plasma codes (Fukazawa et al. 1998).

increases from 0.3 to 0.6–0.7 $Z_{\rm solar}$ toward richer systems. They explained the observed variation in the Si/Fe ratio with the ICM temperature by the escape of SNe cc products (figure 2.3). If the SNe cc products have higher specific energies than the SNe Ia products, the larger fraction of SNe cc products will escape from the shallower gravitational potential of poorer systems.

After the launch of *Suzaku*, which is Japanese fifth X-ray observatory, studies of alpha elements have made progress. The X-ray Imaging Spectrometer (XIS; Koyama et al. 2007) onboard *Suzaku* has good sensitivity for lines in lower energies, thanks to a good line spread function and low particle background level. The alpha elements, which were synthesized mainly in SNe cc, in the ICM outside cool-core regions up to $\sim$0.3 r_{200} have been measured from several nearby clusters and groups ($z \sim 0.001$) with *Suzaku* (e.g. Matsushita et al.2007; Komiyama et al. 2009; Sato et al. 2007a, 2008, 2009a, 2010; Sakuma et al. 2011). The observed metal abundance patterns to $Z_{\rm Fe}$ are summarized in figure 2.4 (Matsushita et al. 2012). Most of the observed abundance patterns are close to the solar abundance ratio. Namely, there is no significant difference in the abundance pattern between the clusters and groups of galaxies, and the observed abundance patterns for O, Mg, Si, and S over Fe all lie between the SN Ia and SN cc values. Therefore, both types of the supernova are considered to have enriched the ICM of the clusters. Since the metals synthesized in the galaxies in clusters are all considered to have been kept within the cluster systems, the cumulative numbers of SN Ia and SN cc explosions is to be estimated from the mass of metals contained in clusters. The two types of supernovae are significantly different in their metal yields. Most of O and Mg are synthesized by SN cc, while Fe is mostly produced by SN Ia. Combining the *Suzaku* results with the SNe nucleosynthesis model, Sato et al. (2007b) calculated integrated numbers of SNe Ia and SNe cc explosions in nearby clusters. They showed that the number ratio of SNe cc to Ia is $\sim$3.5, and Fe has been synthesized predominantly by SNe Ia. A similar result is reported in de Plaa et al. (2007)

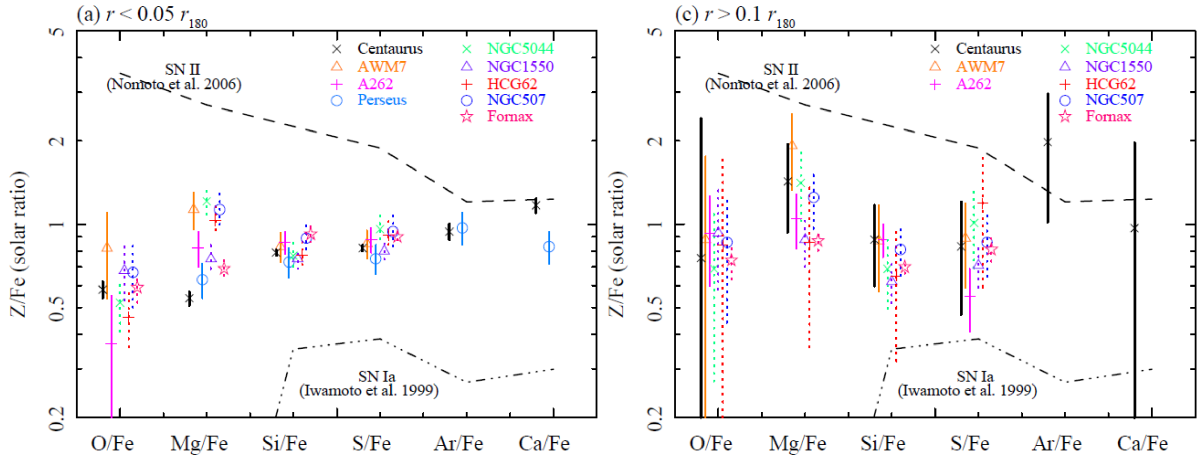

Figure 2.4: The abundance patterns of O, Mg, Si, S, Ar, and Ca to Fe for $< 0.05 r_{180}$ (left) and $> 0.1 r_{180}$ (right) of the Centaurus cluster (Sakuma et al. 2011), AWM7 cluster (Sato et al. 2008), Abell 262 (Sato et al. 2009b), the Perseus cluster (Tamura et al. 2009), the NGC 5044 group (Komiyama et al. 2009), the NGC 1550 group (Sato et al. 2010), HCG 62 (Tokoi et al. 2008), the NGC 507 group (Sato, Matsushita & Gastaldello 2009), and the Fornax cluster (Matsushita et al. 2007; Murakami et al. 2011).

based on data of *XMM-Newton*.

The radial profiles of $Z_{\rm Fe}$ of the ICM in nearby ($z < 0.08$) clusters were derived from the *XMM-Newton* observations. In the left panel of figure 2.5, the weighted average of the radial profiles of $Z_{\rm Fe}$ was shown according to whether they are cD or non-cD clusters. In cluster core regions ($< 0.1 r_{180}$), the observed $Z_{\rm Fe}$ of cD clusters show significant excess compared with those of non-cD clusters. In the outer regions more than $0.1 r_{180}$, $Z_{\rm Fe}$ shows similar profiles between cD and non-cD clusters. The right panel of figure 2.5 compares the radial profiles of the Fe abundances in the ICM of groups and clusters of galaxies observed with *Suzaku* and *XMM-Newton*. The groups of galaxies have similar $Z_{\rm Fe}$ profiles, and higher the Fe abundance than those of cD clusters.

2.3.7 Observational studies of Fe abundance evolution

Recently, *XMM-Newton* and *Chandra* have measured metal abundance of the ICM in high-redshift clusters mainly determined by dusing Fe-L and Fe-K lines as described Chapter 1. Using *XMM-Newton* and *Chandra* data, some literature reported that the clusters at $z > 0.5$ have a constant average abundance $Z_{\rm Fe} \approx 0.25$ solar, while clusters at $z < 0.5$ exhibit a significantly larger abundance of $Z_{\rm Fe} \approx 0.4$ solar (figure 2.6; Balestra et al. 2007; Maughan et al. 2008; Snowden et al. 2008; Anderson et al. 2009). Baldi et al. (2012) tried to study dependence of the metal evolution on distance from the center by spatially resolved analysis, but they obtained no statistically significant conclusion about the different evolutionary path that the different regions of the clusters may have traversed.

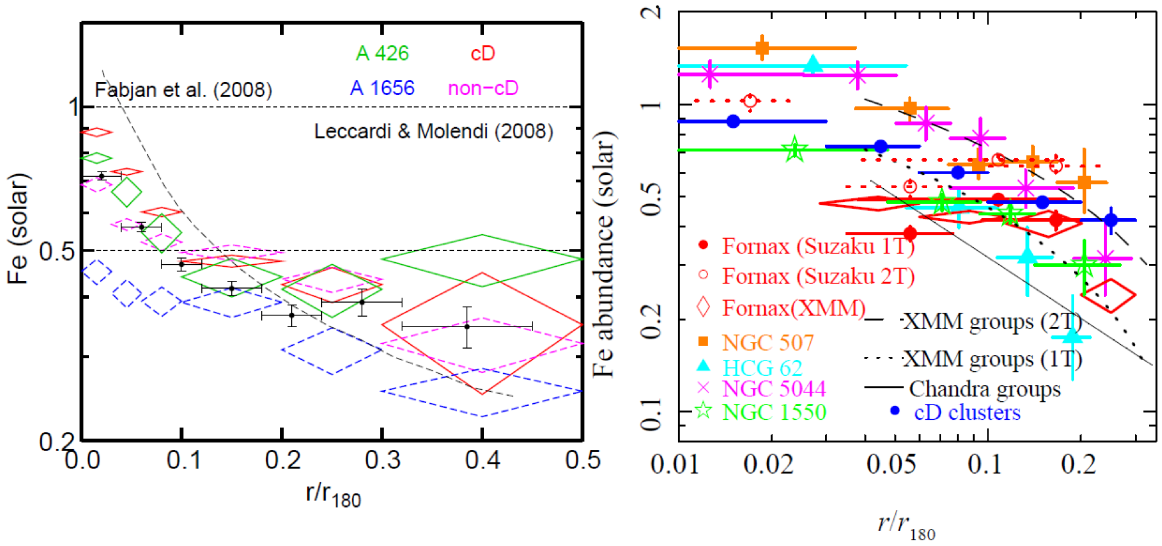

Figure 2.5: left: Fe abundance profiles of the Perseus cluster (green), the Coma cluster (blue), and the averages of those of cD clusters (red solid dia) and non-cD clusters (magenta dashed dia) (Matsushita et al. 2012) with the average profile of $z = 0.1 \sim 0.3$ clusters (black clised circles: Leccardi & Molendi 2008). right: Radial profiles of $Z_{\rm Fe}$ in the Fornax cluster (Murakami et al. 2011), NGC 507 group (Sato, Matsushita & Gastaldello 2009), HCG 62 group (Tokoi et al. 2008), NGC 5044 group (Komiyama et al. 2009), and a NGC 1550 group (Sato et al. 2010).

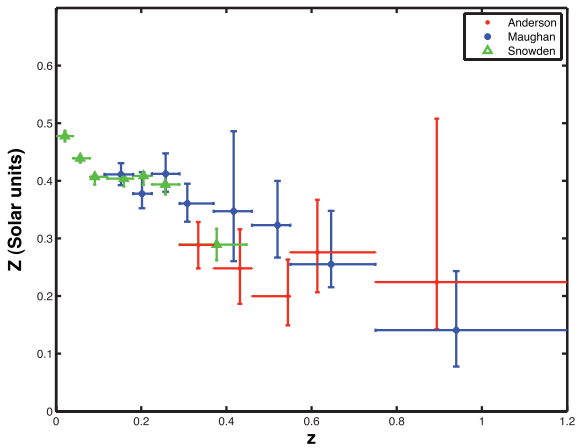

Figure 2.6: The Fe abundance evolution as a function of redshift (Anderson et al. 2009).

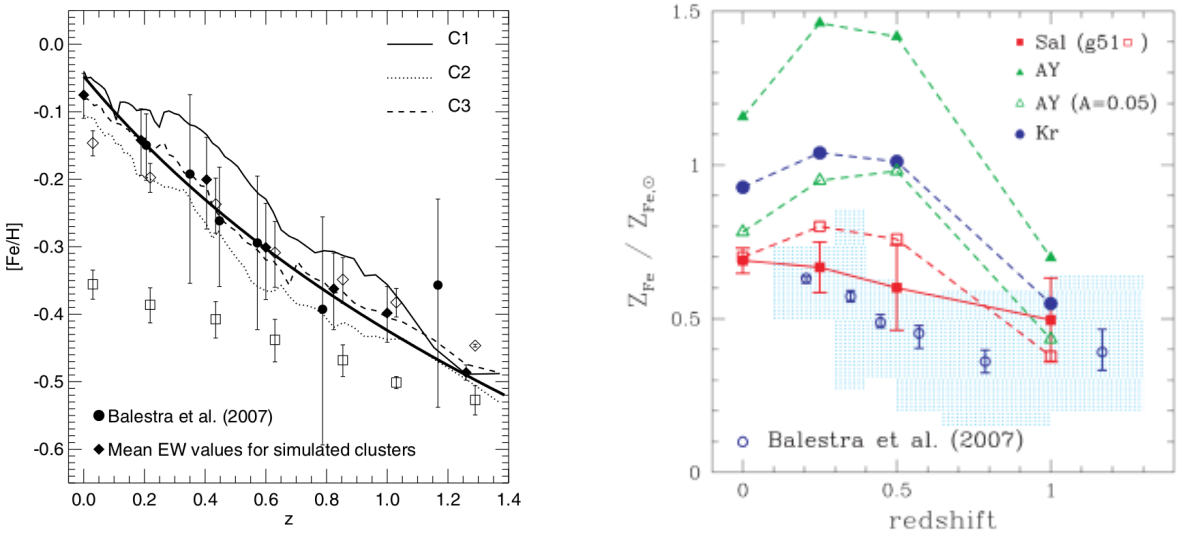

Figure 2.7: The comparison between observations and simulations for the evolution of the $Z_{\rm Fe}$. left: Thin lines denote the meal iron abundance of the three simulated clusters (Cora et al. 2008). Filled circles indicate the observational data from Balestra et al. (2007). right: The dependence of the simulation results on the stellar IMF (Fabjan et al. 2008). Open circles denote observational results of Balestra et al. (2007).

2.3.8 Theorical studies of Fe abundance evolution

Many kind of theoretical approaches have been used so far aimed at studyind the processes of metal enrichment of the ICM (e.g. Nagashima et al. 2005; Cora et al. 2008; Fabjan et al. 2008). For instance, Cora et al. (2008) simulated the metal enrichment of the ICM with the model combining hydrodynamical cosmological simulations of clusters of galaxies and a semi-analytic model of galaxy formation. They explained the observed metalicity by the sinking of clumps of low-entropy highly enriched gas in the central cluster regions (left panel of figure 2.7).

Fabjan et al. (2008) utilized the smoothed particle hydrodynamical simulations to characterizing the evolution of the metal enrichment of the ICM, and reported that the Salpeter initial mass function (IMF; Salpeter 1955) provided an enrichment consistent with observations (right panel of figure 2.7).

Chapter 3

INSTRUMENTATION

3.1 *Suzaku*

3.1.1 Mission description

Suzaku is the Japanese 5th X-ray astronomical satellite, and was launched on July 10 2005 from the Uchinoura Space Center (Kagoshima) by the M-V rocket (Mitsuda et al. 2007). The satellite has a mass of 1680 kg and a length of 6.5 m. Figure 3.1 shows the appearance and configuration of *Suzaku*. The most prominent feature of *Suzaku* is the excellent X-ray sensitivity covering a broad energy range of 0.2 to 600 keV with three onboard detectors. The telescopes have an angular resolution of $\sim 2'$ in half-power-diameter (HPD). This is better than that of ASCA ($\sim 3'$), although not as good as that of *Chandra* ($\sim 0.''5$) and *XMM-Newton* ($\sim 6''$) which are the US and the European missions, respectively.

The four of five telescopes are equipped with four X-ray CCD cameras on their focal plane, named the X-ray Imaging Spectrometer (XIS: Koyama et al. 2007). Each CCD camera works as a photon counting detector, by measuring the position and energy of each individual X-ray photon. It thus provides images over a $18'$ field of view (FOV) with good spectral resolution ($E/\Delta E \sim 50$).

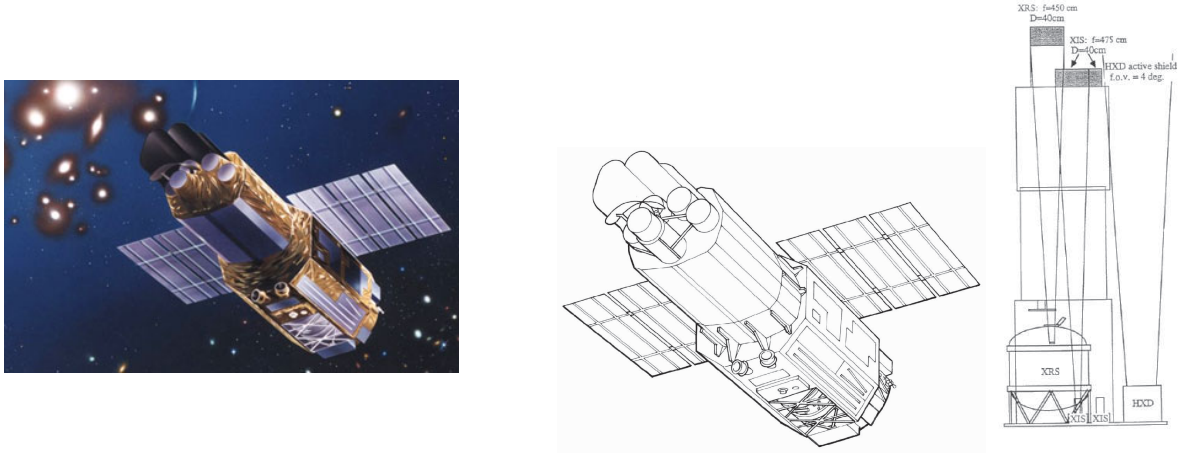

Figure 3.1: (Left) An artist's impression of *Suzaku* in orbit. (right) Schematic picture of the bottom of the *Suzaku* and a side configuration view of the instrument and telescopes onboard *Suzaku*.

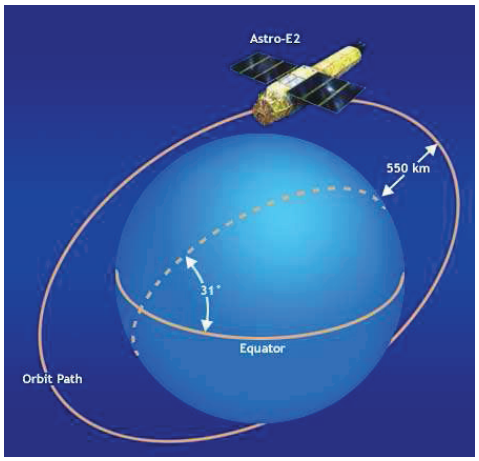

Figure 3.2: A schematic view of the *Suzaku*'s orbit.

The characteristics of the XIS are described in § 3.1.3. The other instruments are the non-imaging, collimated Hard X-ray Detector (HXD: Takahashi et al. 2007; Kokubun et al. 2007), which extends the bandpass of the observatory to 600 keV. The rest one telescope is equipped with an X-ray microcalorimeter, named X-Ray Spectrometer (XRS: Kelley et al. 2007), which had an excellent energy resolution capability but was terminated due to unexpected cryogen evaporation.

As shown in figure 3.2, the orbit of *Suzaku* is near-circular with an altitude of 550 km, an inclination of 31°.9, and an orbital period of about 96 minutes. The maximum slew rate of the spacecraft is 6°/min, and settling to the final attitude takes $\sim$ 10 minutes, using the equipped star trackers.

3.1.2 X-Ray Telescopes (XRTs)

Configuration

The five X-ray telescopes (XRT: Serlemitsos et al. 2007) of *Suzaku* adopt grazing-incidence Wolter I optics, like previous high throughput X-ray imaging missions such as *ROSAT*, *ASCA*, and *XMM-Newton*. Four XRTs (XRT-I) are used for the XIS, and the other XRT (XRT-S) is for the XRS. The XRT-I and XRT-S are mostly the same but are slightly different in their focal length and number of nesting. Figure 3.3 shows a photograph of a mirror assembly, and schematic view of a telescope. Each telescope consists of 175 gold-coated nested mirror shells with a common optical axis and a common focal plane.

In grazing-incidence optics, the effective area is determined not only by the X-ray energy and the telescope aperture, but also by the number of nested mirrors and hence by the filling factor of the mirrors relative to the front aperture. The thinner the mirror shells and the high density nesting is the key to realize the larger collecting area. As summarized in table 3.1, the thickness of the mirror is $\sim$ 178 μm (Substrate thickness is 155 μm).

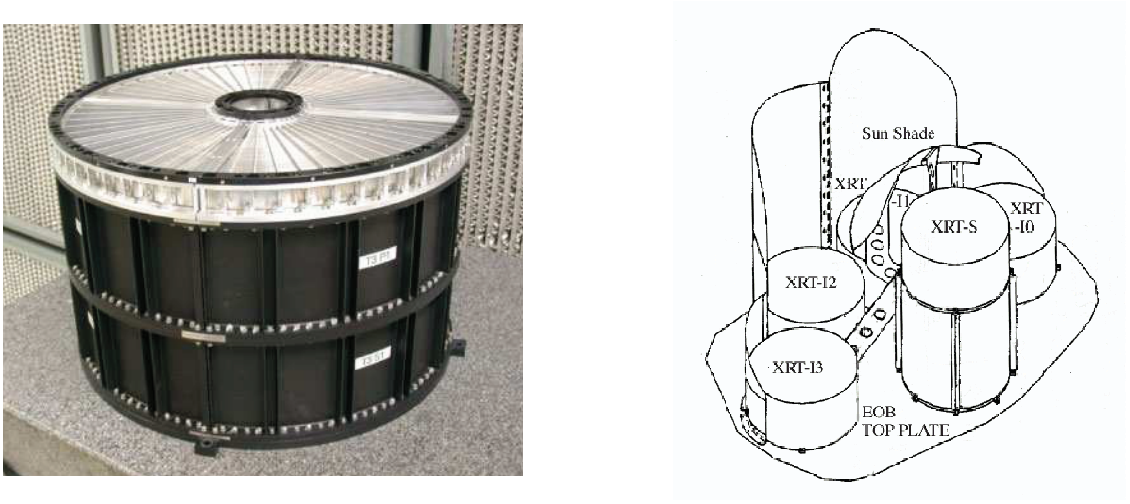

Figure 3.3: (left) A *Suzaku* XRT. (right) Layout of the XRTs on the *Suzaku* spacecraft.

Table 3.1: Telescope dimensions and design parameters of XRT-I.

Number of telescopes	4
Focal length	4.75 m
Inner Diameter	118 mm
Outer Diameter	399 mm
Height	279 mm
Mass/Telescope	19.5 kg
Number of nested shells	175
Reflectors/Telescope	1400
Geometric area/Telescope	873 cm^2
Reflecting surface	Gold
Substrate material	Aluminum
Substrate thickness	155 μm
Mirror thickness	178 μm
Reflector slant height	101.6 mm

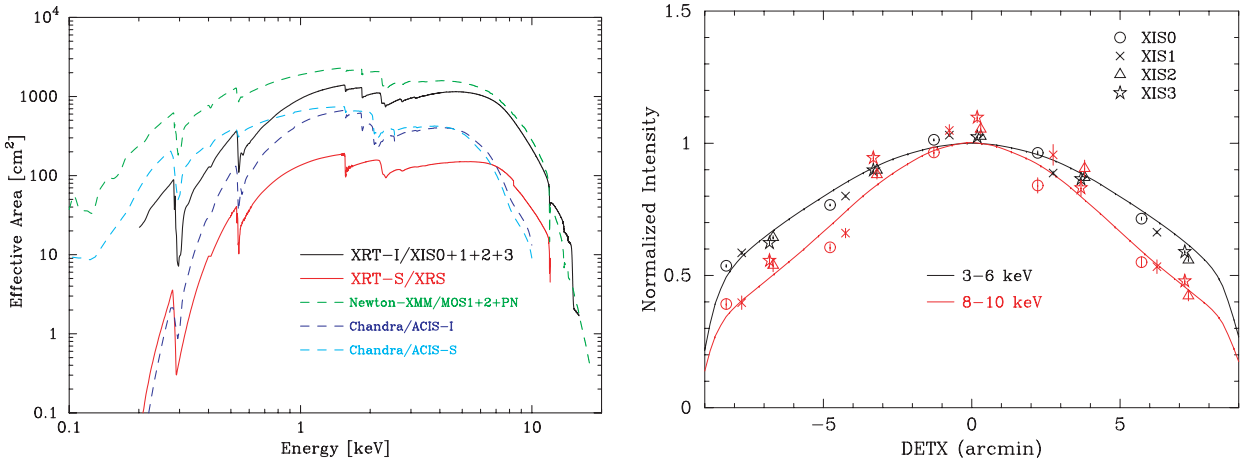

Figure 3.4: (left) Total effective area of the four XRT-I modules compared with that of *XMM-Newton* and *Chandra*. Transmissions of the thermal shield and the optical blocking filter, and the quantum efficiency of the CCD are all taken into account (Serlemitsos et al. 2007). (right) Vignetting of the four XRT-I modules using the data of Crab Nebula taken during 2005 August 22–27 in the two energy bands 3–6 keV and 8–10 keV (Serlemitsos et al. 2007).

Effective area

Left panel of figure 3.4 shows the total effective area of the four XRT-I modules, including the detector efficiency, compared with that of *XMM-Newton* (PN + 2MOS) and *Chandra* (ACIS-I and ACIS-S). The effective areas for *Chandra* were calculated from the ARF files provided for AO cycle 2 proposal, while those for *XMM-Newton* were taken from the ARF for the nominal position using CALINDEX #0122. Although the total weight is only ≤ 80 kg, the effective area of the four XRT-I modules at 7 keV is comparable to that of *XMM-Newton* mirrors, whose total weight is as much as 1311 kg.

In general, the critical angle of X-ray mirrors depends on the incident X-ray energy E and the density of reflective matter ρ as $\theta_c \propto \sqrt{\rho}/E$. Thus, the critical angle become smaller linearly toward higher energies, making photon collection progressively harder. In the case of *Suzaku*, the grazing angle is designed to be $\sim 0^\circ.6$ for the XRT-I. Note that $0^\circ.6$ corresponds to the critical grazing angle of gold for total reflection of the 7.65 keV X-rays. The effective area of an X-ray telescope decreases as the off-axis angle increases, because the grazing angle to the mirror shells increases, and hence exceeds the critical angle of the outer shells. This effect, called "vignetting", of *Suzaku* is shown in right panel of figure 3.4 for X-axis. Toward the edge of the FOV, the telescope effective area decreases down to ~ 30 % of the on-axis value. The vignetting effect becomes stronger for higher energy photons.

Point-spread function

Generally, the response function (particularly, the radial brightness distribution on the focal plane) of a telescope to a point source at infinite distance is called Point-Spread Function (PSF). The PSF

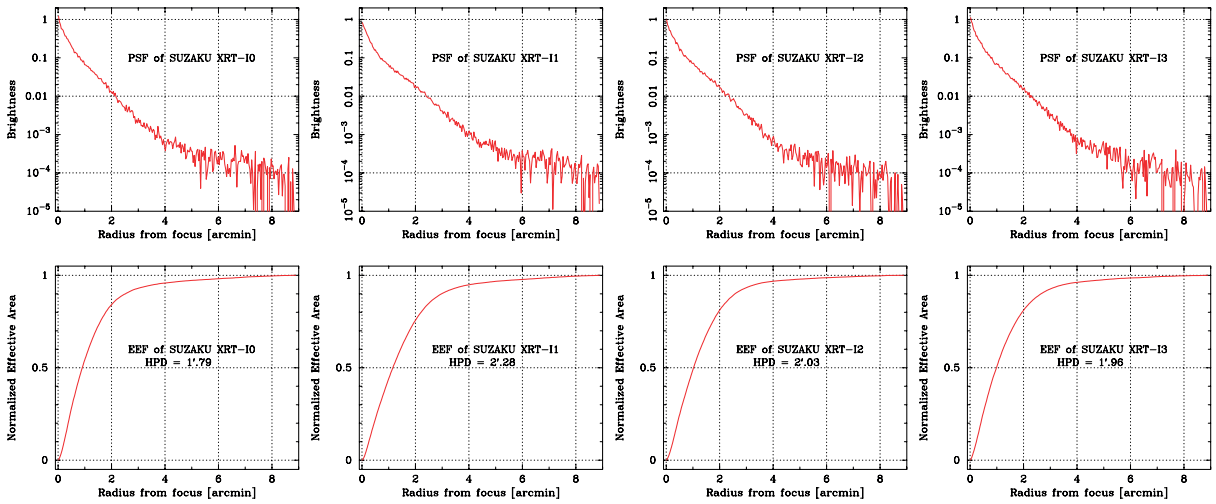

Figure 3.5: (PSF (upper) and EEF (lower) of the four XRT-I modules in the focal plane. The EEF is normalized to unity at the edge of the CCD chip (a square of $17'.8$ on a side).

of an X-ray telescope depends on the X-ray energy and the off-axis angle. The on-axis PSF and encircled-energy fraction (EEF) of the XRT are shown in figure 3.5. The HPD is thus $\sim 2'$ in terms of FWMH.

3.1.3 X-ray Imaging Spectrometer (XIS)

Basic properties

As already mentioned in subsection 3.1.1, the XIS consist of four X-ray CCD cameras. The XIS, like other X-ray CCDs with single-photon readouts, detects an X-ray photon by photoelectric absorption in the depletion layer, and determines the photon energy by measuring electric charges created in proportion to the incident photon energy.

The four XISs are named XIS0, XIS1, XIS2, and XIS3. Each CCD camera has a single CCD chip with an array format of 1024×1024 pixels, and covers an $17'.8 \times 17.8'$ region on the sky with the XRT-I. Each pixel size is 24 μm square, and the size of the CCD is 25 mm$\times$25 mm. XIS1 uses a back-side illuminated (BI) CCDs, while the other three use front-side illuminated (FI) CCDs. The specification of the XIS CCD combined with the optical blocking filter (OBF) and the XRT is summarized in table 3.2.

FI CCD detects X-ray photons that penetrates through its "front side" gate structures. Because of the dead layer due to the inevitable photoelectric absorption at the gate structure, the low-energy quantum detection efficiency (QDE) of the FI CCD is rather limited. Conversely, a BI CCD receives photons from the side without the gate structures. For this purpose, the undepleted layer of the CCD is completely removed in the BI CCD, and a thin layer to enhance the electron collection efficiency is added in the back surface. A BI CCD retains a high QDE even in sub-keV energy band because of the absence of gate structure on the photon-detection side. However, a BI CCD tends to

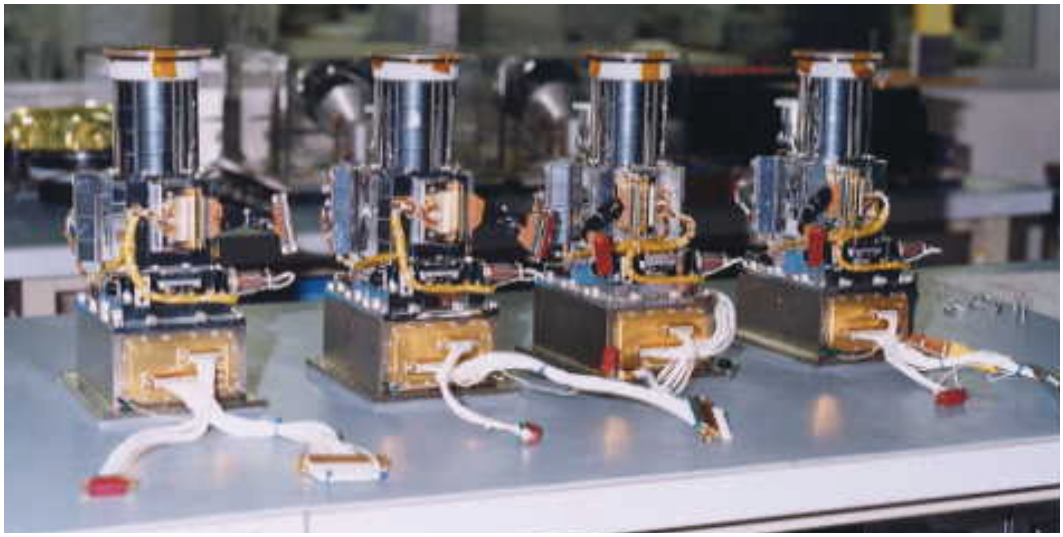

Figure 3.6: The four XIS detectors before installation onto *Suzaku*.

Table 3.2: Specifications/characteristics of the XIS CCD combined with the OBF and the XRT (Koyama et al. 2007).

Field of view	$17'.8 \times 17'.8$
Energy range	0.2–12.0 keV
Format	1024×1024 pixels
Pixel size	24 μm $\times$ 24 μm
Energy resolution	$\sim$ 130 eV (FWHM) at 5.9 keV
Effective area[a]	
1.5 keV	330 cm^2 (FI), 370 cm^2 (BI)
8.0 keV	160 cm^2 (FI), 110 cm^2 (BI)
Readout noise	$\sim$ 2.5 electrons (RMS)
Time resolution	8 s (normal), 7.8 ms (P-sum[b])

[a] On-axis effective area for one sensor including the OBF transmission, the CCD quantum efficiency, and the XRT effective area. The calculations are for a point source integrated over a circular region with a 6 mm ($4'.34$) radius.

[b] Parallel-sum clocking mode.

have a slightly thinner depletion layer, and the QDE is slightly lower than that of a FI CCD in the high energy band.

Filter

The XIS CCDs are sensitive not only to X-ray photons, but also to visible and ultraviolet light. Therefore, if a target has a high optical flux, the X-ray signals are contaminated by these photons, and the observation may suffer from such effects as shot noise, finite offset, fake event splits between pixels, and saturation of electron traps which reduces the charge transfer efficiency. To prevent these, each XIS has an OBF in front of it. The OBF is made of polymide with a thickness of 1000 Å, coated with a total of 1200 Å of aluminium (400 Å on one side and 800 Å on the other side).

3.1.4 XIS backgrounds

In general, the background of X-ray observatories is categorized into X-ray background (XRB) and non-X-ray background (NXB) due to charged particle and instrumental noise.

The XRB is composed of cosmic X-ray background (CXB) and Galactic foreground emission (GFE). The CXB are thought to be a composite of unresolved faint X-ray sources (e.g. distant AGN). It exhibits a power law spectral shape with a photon index of ~ 1.4. The GFE typically consists of an unabsorbed plasma (LHB; representing the local hot bubble and the solar-wind charge exchange) and an absorbed plasma (MWH; representing the Milky Way halo). The LHB and the MWH have temperatures of ~ 0.1 keV and ~ 0.3 keV, respectively. The XRB is rather uniform, with directional intensity variations up to ~ 30 % below ~ 2 keV and up to ~ 5 % above.

The NXB, which is the instrumental background except for the celestial X-ray background, consists of instrumental detector noise, dominant in low energies, and particle background. High-energy particles interact with the detectors and surrounding structure, and create background with a flat continuum and fluorescence lines.

Cosmic ray (charged particle) and other internal background events are effectively removed using the hit patterns on CCD pixels (GRADE), the position (STATUS) and time of an event. The definition of GRADE is shown in figure 3.7. Most of X-ray events take GRADE = 0, 2, 3, 4, or 6. On the other hand, most of the events of other GRADEs are dominated by non-X-ray events, and should be excluded. STATUS parameter stores the information of pixel quality of an event. Known hot pixels, bad charge transfer efficiency, flickering pixels, and pixels on the segment boundaries can be removed by selecting the events with STATUS set to < 131072. The parameters used in good time interval (GTI) selection are shown in table 3.3. The signal to noise ratio can be improved with an appropriate GTI criteria, indicated in table 3.3.

In the XIS, the NXB rate between 1–12 keV is 0.11 cts/s in the FI CCDs and 0.40 cts/s in the BI CCD. Figure 3.8 shows the NXB spectra of FI and BI CCDs when the XIS observes the night

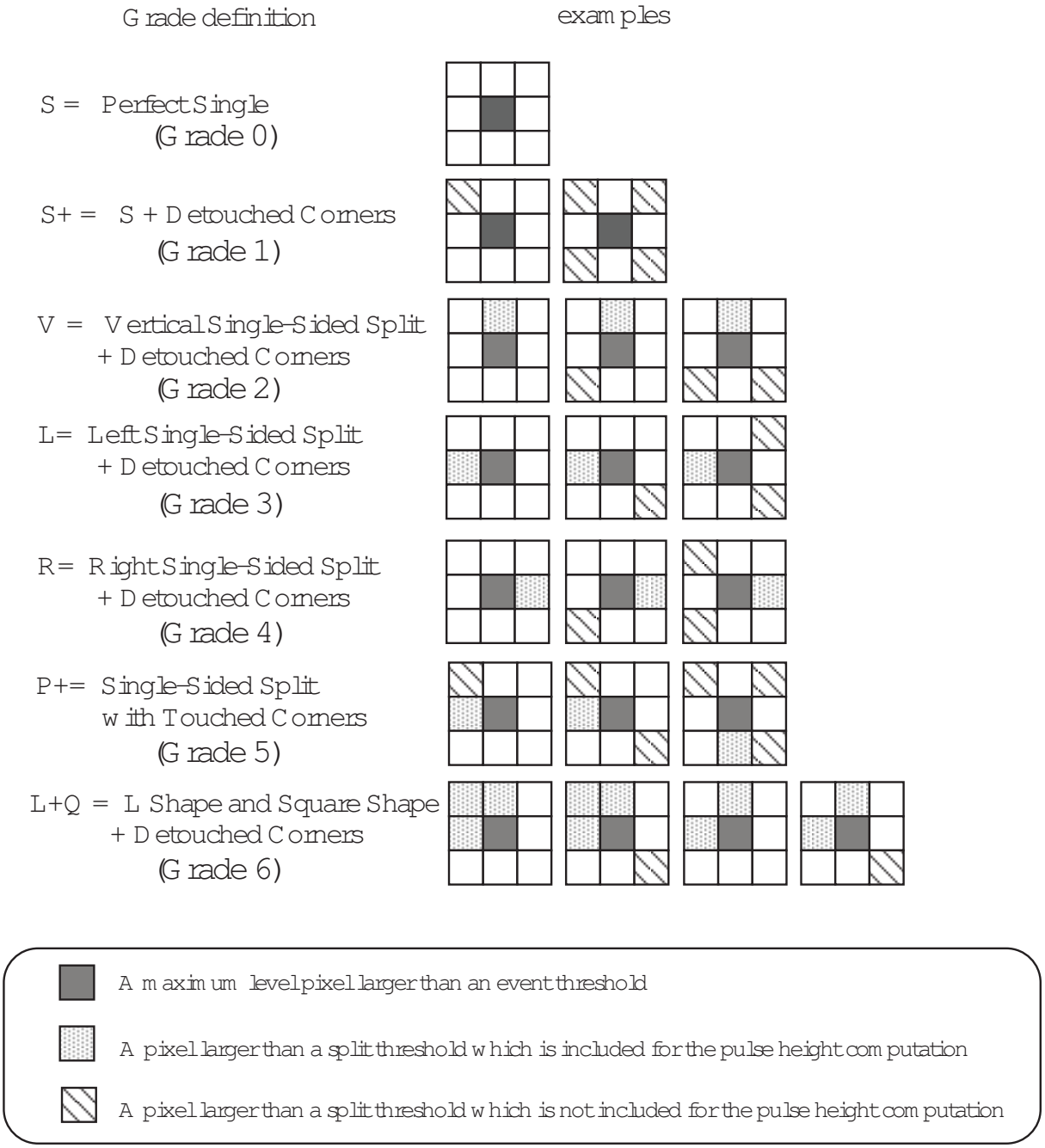

Figure 3.7: Definition of GRADE of CCD events.

Table 3.3: Parameters used in GTI selection of *Suzaku*.

Parameter	Definition	Recommended value
SAA	Whether the satellite was in the SAA[a] or not	eq.0
T_SAA	Time after the last SAA[a] duration (s)	> 255
ELV	Elevation angle from the Earth limb (degree)	> 5
DYE_ELV	Elevation angle from the day Earth limb (degree)	> 20
COR	Cut off rigidity of the cosmic ray (GeV/c/particle)	> 8

[a] South Atlantic Anomaly

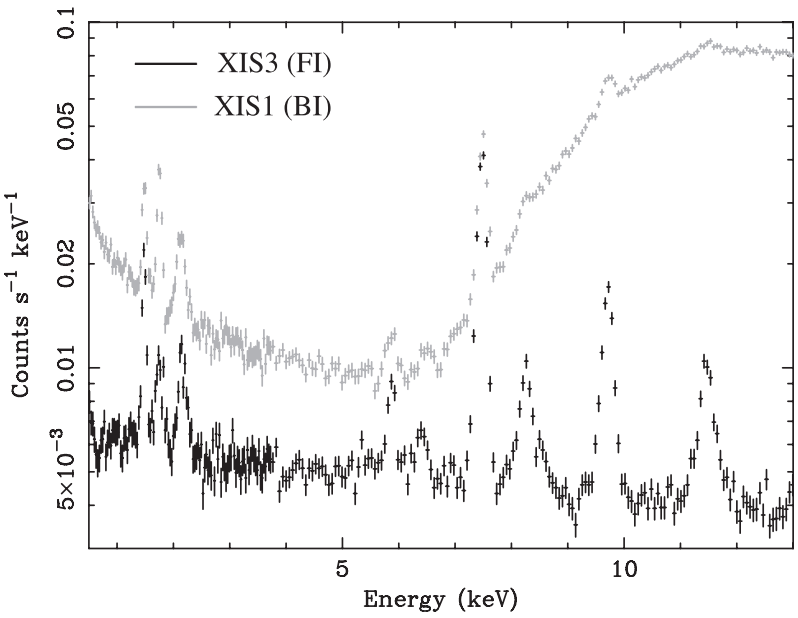

Figure 3.8: The NXB spectra with the BI and FI CCDs (Koyama et al. 2007).

Earth. There are also fluorescence features arising from the calibration source as well as material in the XIS and XRTs. The Mn-K lines are due to the scattered X-rays from the calibration sources.

3.2 *Chandra*

3.2.1 Mission description

Chandra (Weisskopf et al. 2002) is the USA X-ray astronomical satellite, and was launched by NASA on the Space Shuttle Columbia on July 23, 1999. Figure 3.9 shows the schematic view of *Chandra*. The orbit of the satellite is elliptical with the perigee altitude of 16,800 km, the apogee altitude of 132,000 km. The orbital period is about 63.5 hours, which is allowing uninterrupted observing intervals of more than 48 hours.

The most vivid characteristic of *Chandra* is higher angular resolution than all the previous X-ray satellites. The *Chandra* telescope, named High Resolution Mirror Assembly (HRMA), consists of 4 mirrors of Wolter Type-I geometry formed by glass base, and achieved the angular resolution of $0''.5$. The satellite attitude is controlled and determined by Pointing Control and Aspect Determination system with the higher accuracy than angular resolution.

Chandra has two focal plane instruments: a microchannel plate, named High Resolution Camera (HRC), and a X-ray CCD camera, named Advanced CCD Imaging Spectrometer (ACIS). *Chandra* also has two gratings: High-Energy Transmission Grating, and Low-Energy Transmission Grating. To protect the instruments from the particle radiation damage, *Chandra* is equipped with a charged-particle detector.

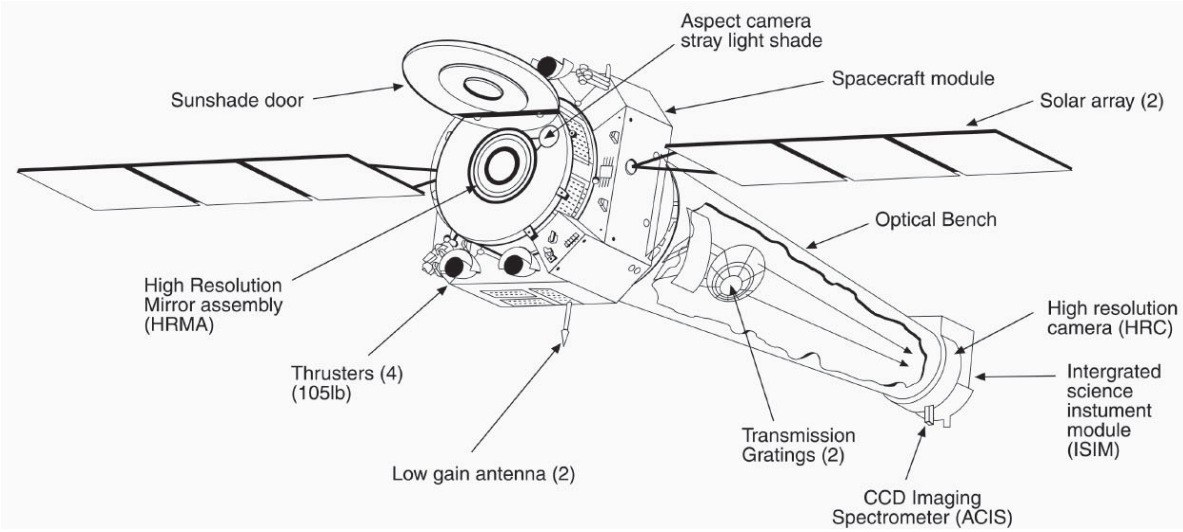

Figure 3.9: Schematic view of the *Chandra* satellite.

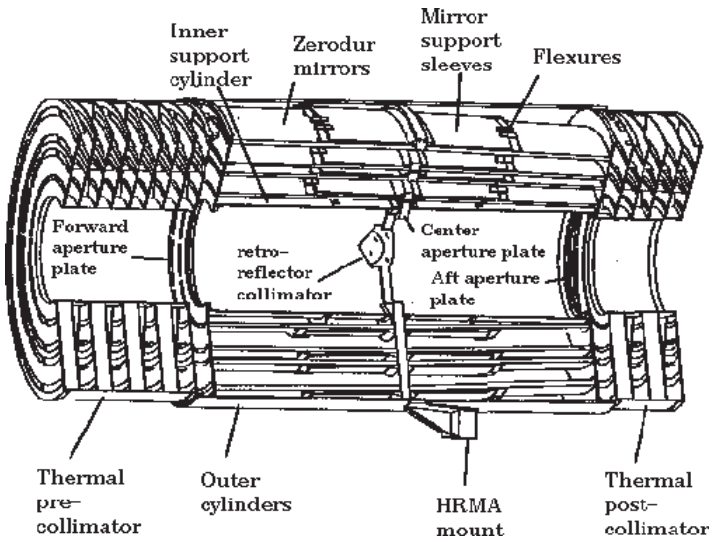

Figure 3.10: Schematic view of the telescope.

3.2.2 High Resolution Mirror Assembly (HRMA)

Configuration

The *Chandra* has four pairs of Wolter Type-I mirrors, which were fabricated from Zerodur glass, polished, and coated with iridium on a binding layer of chromium. X-ray optics are reviewed by Aschenbach (1985). Figure 3.10 shows the schematic view of a telescope. The outer diameters of mirrors are 1.23, 0.99, 0.87, and 0.65 meter, and the focal length is 10.066 meter. As summarized in table 3.4, the coating thickness of the mirror is ~ 330 μm.

Table 3.4: Telescope dimensions and design parameters of HRMA.

Number of telescopes	1
Focal length	10.07 m
Outer Diameter	1.23, 0.99, 0.87, 0.65 m
Height	840 mm
Mass/Telescope	1484 kg
Number of nested shells	4
Reflectors/Telescope	8
Geometric area/Telescope	1145 cm^2
Reflecting surface	Iridium
Substrate material	Zerodur
Coating thickness	330 Å

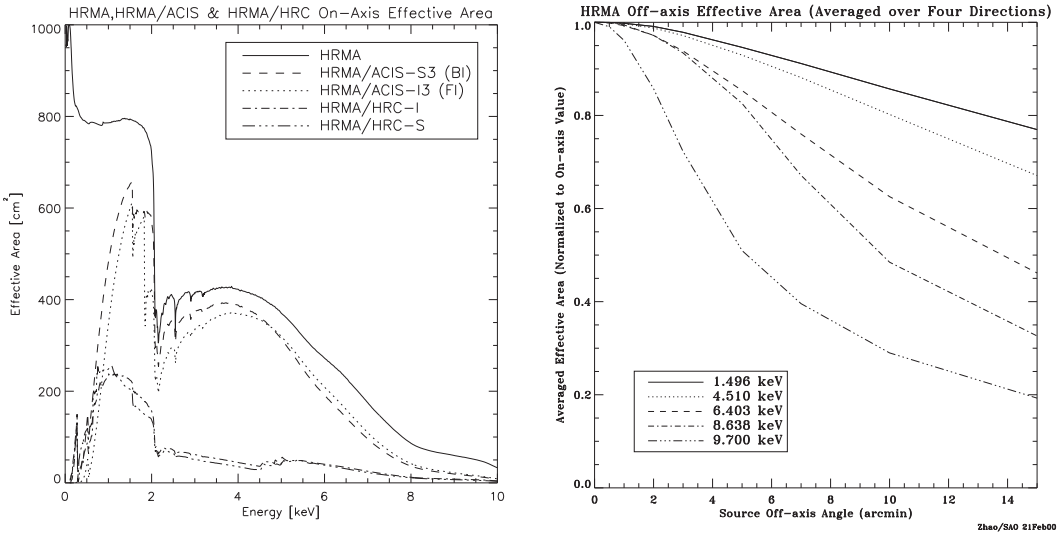

Figure 3.11: (left) The HRMA, HRMA/ACIS, and HRMA/HRC effective areas versus X-ray energy in linear scale. (right) The HRMA effective area versus off-axis angle, averaged over azimuth, for selected energies, normalized to the on-axis area for that energy (by CXO guide HP).

Effective area

The unobscured geometric aperture of the HRMA is 1145 cm^2. The obstruction of the HRMA clear aperture by supporting struts is less than 10%. Since reflectivity depends on energy as well as grazing angle, the HRMA throughput varies with X-ray energy. The left panel of figure 3.11 shows the on-axis HRMA effective area as a function of X-ray energy, as well as the HRMA/ACIS and HRMA/HRC effective areas, in linear scale, and the right panel shows effects of off-axis vignetting on the effective area for various energies; the plotted results are averages over the azimuthal angle.

Point-spread function

The PSF of *Chandra* HRMA has been simulated with numerical ray-trace calculations. One of the most useful parameters is the encircled energy fraction as a function of radius from the PSF center.

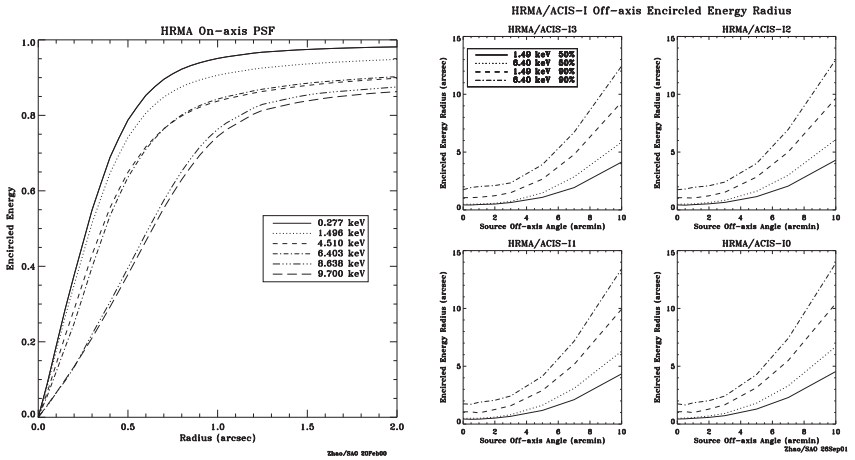

Figure 3.12: (left) Fractional encircled energy as a function of angular radius calculated for an on-axis point-source, at selected X-ray energies. (right) HRMA/ACIS-I encircled energy radii for circles enclosing 50% and 90% of the total energy at 1.49 and 6.40 keV as a function of off-axis angle (by CXO guide HP).

Left panel of figure 3.12 shows the encircled energy fraction of HRMA. The increase in image size with higher energy is apparent. The PSF also broadens for off-axis sources. The increase in image size with off-axis angle is the greatest for the inner shell, and hence is larger for higher X-ray energies. Right panel of figure 3.12 shows the dependence of encircled energy radii on off-axis angle on the four ACIS-I chips. The HPD is typically $\sim 0''.5$ in terms of FWMH.

3.2.3 Advanced CCD Imaging Spectrometer (ACIS)

Basic properties

ACIS offers the capability to simultaneously acquire high-resolution images and moderate resolution spectra. ACIS contains 10 planar, 1024×1024 pixel CCDs (figure 3.13); four arranged in a 2×2 array (ACIS-I) used for imaging, and six arranged in a 1×6 array (ACIS-S) used either for an imaging or grating readout. Two CCDs are BI and eight are FI. The chip-average energy resolution of the BI devices is, currently, better than that of the FI devices. Any combination of up to 6 CCDs may be operated simultaneously. Operating six chips increases the chances of serendipitous science but at the cost of increased total background counting rate and therefore enhanced probability of saturating telemetry. The specification of the ACIS CCD is summarized in table 3.5.

Filter

Similar to the Suzaku XIS case, OBFs are placed just over the CCDs. The filters are composed of polyimide sandwiched between two thin layers of aluminum. The nominal thicknesses of the these components for the two arrays are given in table 3.6 (detailed in web[1]).

[1] http://cxc.harvard.edu/proposer/POG/html/index.html

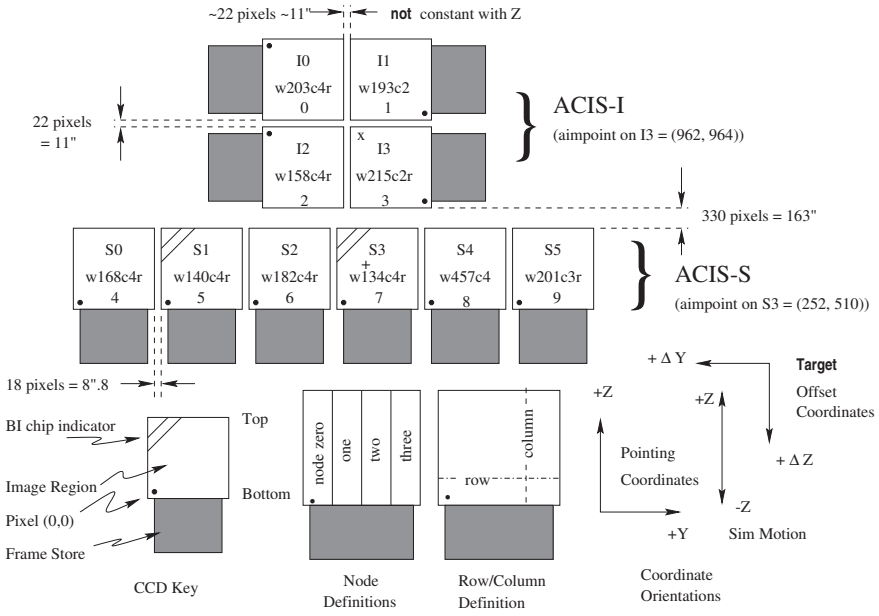

Figure 3.13: Schematic view of the ACIS focal plane (by CXO guide HP).

Table 3.5: Specifications/characteristics of the ACIS CCD.

Field of view	$16'.9 \times 16'.9$ (ACIS-I)
	$8'.3 \times 50'.6$ (ACIS-S)
Energy range	0.2–12.0 keV
Format	1024×1024 pixels
Pixel size	24 μm $\times$ 24 μm
Energy resolution	$\sim$ 130 eV (FWHM) at 5.9 keV
Effective area[a]	
1.5 keV	600 cm^2 (FI)
8.0 keV	40 cm^2 (FI)
Readout noise	$\sim$ 2 electrons (RMS)
Time resolution	3.2 s (normal)

[a] On-axis effective area.

Table 3.6: Nominal OBF composition and thicknesses.

ACIS-I	Al/Polyimide/Al	1200Å/2000Å/400Å
ACIS-S	Al/Polyimide/Al	1000Å/2000Å/300Å

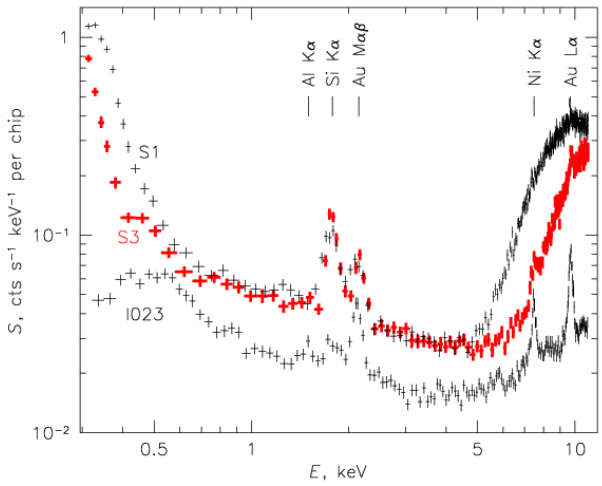

Figure 3.14: The NXB spectra with the BI and FI CCDs.

3.2.4 ACIS backgrounds

In the ACIS, the NXB rate between 0.3—10 keV is $\sim$ 0.4 cts/s in the FI CCDs and $\sim$ 1.0 cts/s in the BI CCD. Figure 3.14 shows the NXB spectra of FI and BI (detailed in web[2]). The event selection criteria is basically same as *Suzaku* (subsection 3.1.4). There are also fluorescence features arising from the calibration source as well as material in the ACIS and XRT.

[2]http://cxc.harvard.edu/proposer/POG/html/chap6.html

Chapter 4

OBSERVATION AND DATA REDUCTION

4.1 Targets

4.1.1 Selection criteria

Suzaku has observed a number of clusters of galaxies, and has archived observation of 116 clusters and groups as of 2013 March. I selected the data of clusters of galaxies to perform the ICM chemical evolution study. I omitted data of four clusters of WBL 088, Hydra Cluster, NGC 0507, NGC 4759 GROUP from this investigation because these clusters have studied in detail in Sato et al. (2007b). Then I reduced targets according to the target selection criteria listed below.

1. *Chandra* should have observed the target to support the angular resolution of *Suzaku* ($\sim 2''$). We utilized *Chandra* data to make ancillary response files (ARFs) of *Suzaku* and extract point sources in the FOV.

2. No luminous objects (like a AGN) should be in the FOV. *Suzaku* cannot exclude effects from the luminous contamination sources because of the limited angular resolution.

3. The coverage of *Suzaku* observation up to 0.3 r_{200} should be larger than the circular area of 50%. It is crucial to estimate a average temperature and metal abundances in the ICM.

By applying criterion 1, the data have been reduced from 113 to 79. The criterion 2 eliminated three objects of 1WGA J2235.3-2557, ABELL 3395, and ABELL 1750. The criterion 3 excluded 14 objects. The final selected sample consists of 62 objects, as shown table B.1. We presented the redshift distribution of our sample of 66 objects in figure 4.1, where the cluster redshifts are provided by NED.

4.1.2 Classification of targets

In order to investigate possible connections between our X-ray studies and cluster morphology or dynamical state, we classified our samples based on B–M type, Abell richness class, merging/relaxed,

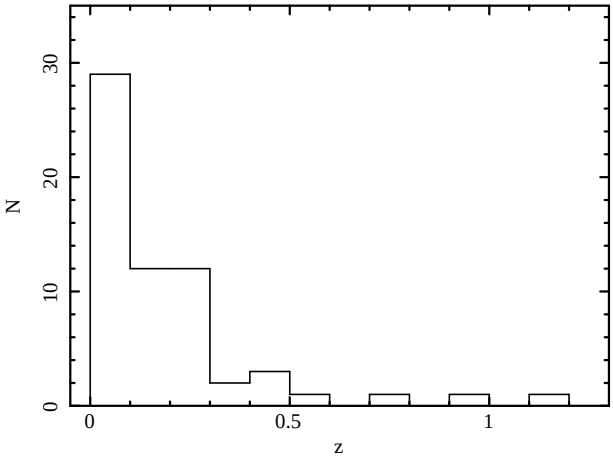

Figure 4.1: Redshift histogram of the 62 clusters of galaxies in our sample.

cool core/non-cool core AGN/non-AGN. The definition of classifications is presented in section 2.2. See table B.1 for each cluster's classification and the associated references.

4.2 Data Reduction

4.2.1 *Suzaku* archive

The information of *Suzaku* observation are summarized in table C.1. In this thesis, we utilize only the XIS data, since no signals are observed by the HXD. Two front-illuminated (FI: XIS 0 and XIS 3) CCD cameras and one back-illuminated (BI: XIS 1) CCD camera were in operation. The average pointing direction of the XIS for the each observations were also summarized in table C.1. All the three XIS detectors were in the normal clocking mode (8 s exposure per frame) with the standard 5×5 and 3×3 editing modes during the data rates of SH/H and M/L, respectively.

We reprocessed unscreened XIS event files using Suzaku software version 20 in HEAsoft 6.13 while referring to the calibration data base (CALDB) of the XIS and the XRT released on 2013 March 5 and 2011 June 30, respectively. The `aepipeline` tool in the HEAsoft package was used for the reprocessing. We applied the standard screening criteria for good time intervals (GTI): the spacecraft is outside the South Atlantic Anomaly (SAA), the time interval after an exit from the SAA is longer than 436 s, the geomagnetic cutoff rigidity (COR) is higher than 8 GV, the source elevation above the rim of bright and night Earth (ELV) is higher than 20° and 5°, respectively, and the XIS data are free from telemetry saturation. We selected XIS events with the *ASCA* grades of 0, 2, 3, 4, or 6 (§ 3.1.4). Effective exposure yielded from these processes are summarized in table C.1.

4.2.2 *Chandra* archive

The information of *Chandra* observations are summarized in table C.2. We utilized this *Chandra* data to make ancillary response files (ARFs) of *Suzaku* and extract point sources.

All the data were reprocessed with `chandra_repro` software to create new level 2 event files using CIAO 4.5 software package, referring to CALDB 4.5.6. The effective exposure of each observation is summarized in table C.2. In the following analysis, the same grade selection as that for the *Suzaku* XIS data (i.e., 0, 2, 3, 4, or 6) was applied. The resulting ACIS image in the 0.5–7.0 keV energy range is shown in figure A.1 with the FOV of XIS.

4.3 Response Files

Redistribution matrix files (RMFs) of the XIS were produced with `xisrmfgen`, and ARFs by `xissimarfgen` version 2010-11-05 (Ishisaki et al. 2007). The effect of contamination by the evaporated material in the spacecraft on the XIS OBF is included in ARFs. Two types of ARFs were generated, $A^{\rm U}$ and $A^{\rm I}$, for the uniform background emission and ICM emission, respectively. The input image of $A^{\rm U}$ is the uniform emission over a circular region of $20'$ radius.

In order to make $A^{\rm I}$, a background subtracted X-ray surface brightness profile of clusters of galaxies were created from an ACIS 0.5–7.0 keV image of the *Chandra* data. At the same time, point sources were detected and removed from the ACIS image, using the `wavdetect` (Freeman et al. 2002) of CIAO with a detection threshold of 5σ. The background was extracted from a region outside the virial radius as far as the virial radius was smaller than ACIS FOV. If it was not the case, the background was extracted from the inner region of virial radius but far enough from the core of clusters. The center of the profiles was determined from the position of X-ray emission centroid in the ACIS image. Then the profile was fitted with β-model (King 1962) of which parameters were determined through the least chi-square method. The resulting parameter set of β-model, $(r_{\rm core}, \beta)$, are summarized in table B.2 where $r_{\rm core}$ is the core radius. The input image of $A^{\rm I}$ is the two dimensional β-model over the entire FOV of XIS, and the extract region of $A^{\rm I}$ is SRC region of figure A.1.

RMFs and ARFs of the ACIS were produced by `specextract` which is included in the CIAO package, together with source and background spectra of the ACIS.

4.4 X-Ray Images

We extracted X-ray images from the reprocessed events files described above section. The X-ray images of XIS and ACIS in the 0.5–7.0 keV energy range are shown in figure A.1.

The observed XIS 0, 1, 3 images were summed on the sky coordinates after removing calibration-source irradiated regions (e.g. 4.2(a)). The exposure map, which contains the effective exposure times of the pixels, was calculated by `xisexpmapgen` (e.g. 4.2(b)). Raw XIS images were divided by exposure map to be reduced to exposure corrected XIS images (e.g. 4.2(c)). The exposure corrected images for each clusters are smoothed with a two dimensional Gaussian function with the kernel of $\sigma = 16$ pixel $\simeq 17''$. The NXB or vignetting were not subtracted or corrected. The scale bar

indicates the X-ray counts per pixel. In the figure A.1, the removed regions of point sources from spectral analysis are indicated by white dashed circles. The source region (SRC) is within the white solid circle. The background region (BGD) has two cases: 1) *Suzaku* observation covered outside of virial radius, 2) *Suzaku* observation did not cover outside of virial radius. In the case 1, BGD is outside the white dashed circle, and in the case 2, BGD is between white solid circle and green dashed circle.

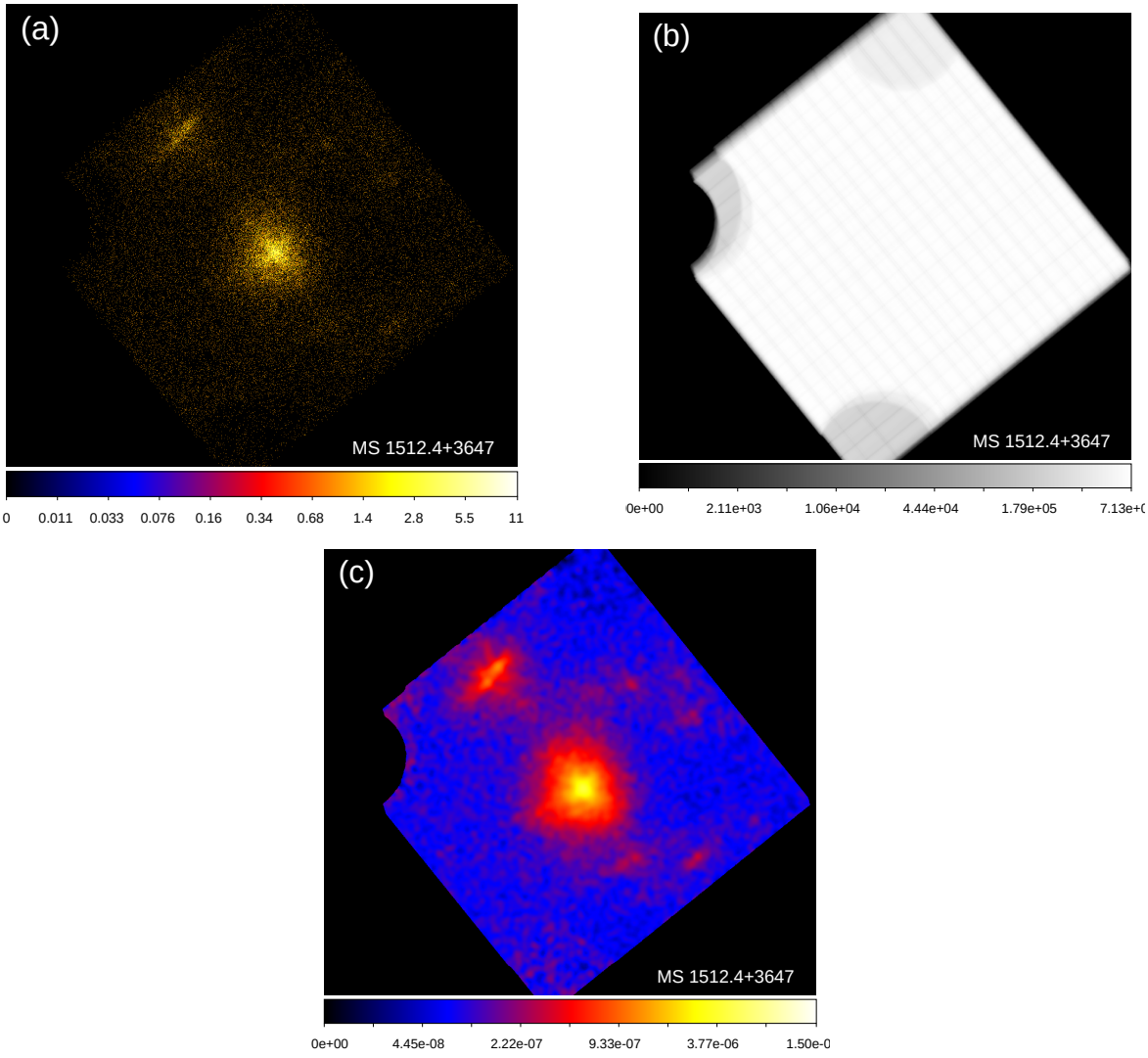

Figure 4.2: (a) Raw observed image for the MS 1512.4+3647. The observed XIS 0, 1, 3 images were summed on the sky coordinates after removing calibration-source regions. (b) Exposure map images for the MS 1512.4+3647. (c) XIS image of MS1512.4+3647 in the 0.5—7.0 keV energy range, smoothed with a two dimensional Gaussian with a kernel of $\sigma = 16$ pixel $\simeq 17''$. The exposure was corrected but the NXB was not subtracted, and the vignetting was not corrected.

ACIS image in 0.5—7.0 keV energy range were smoothed with a Gaussian kernel of $\sigma = 4$ pixel $\simeq 2''$. The Suzaku FOV are shown as the square on the image. The scale bar indicates the X-ray counts per pixel. The point sources detected with `wavdetect` are indicated by black crosses.

4.5 Estimation of Background

Accurate estimation of background is the key to carry out spectral analysis of low surface brightness X-ray emission such as ICM. In the case of distant or small clusters of galaxies, the peripheral region of XIS (outside the virial radius, for example) where no ICM emission is expected can be used for that purpose. In the case of nearby clusters, the virial radius may extend over the XIS FOV. In that case, background was estimated the most outer region of XIS, where the ICM emission is still dominant but the fraction of the background larger then core region of clusters. The XRB levels of in the BGD region is not exactly the same as that in the SRC region, because of the vignetting effect and the PSF of the mirror. Therefore, we estimate NXB and XRB separately which are specific to the region to be analyzed. XRB is composed of CXB and Galactic foreground GFE. We identified point sources with *Chandra* data and excluded them.

4.5.1 Non-X-ray background

The NXB, which is the instrumental background except for the celestial X-ray background, was simulated by `xisnxbgen`, which sorts night Earth data according to COR and integrate the night Earth spectra weighted by the actual COR distribution of the observation (Tawa et al. 2008). Integrated period for the NXB is between ±365 days of the each clusters observation of *Suzaku*. Night Earth events from the same detector area as the region to be analyzed in the XIS image were extracted in `xisnxbgen`. The typical NXB spectra of the XIS are shown in left panel of figure 4.3. The systematic error of the simulated NXB is estimated to be ±3% (Tawa et al. 2008) in 1.0–12.0 keV energy range.

4.5.2 Point sources

The XIS images shown in figure A.1 are thought to be contaminated by a number of point sources, but they are not resolved well due to the moderate spatial resolution of X-ray telescope (a half-power diameter of $\sim 2'$; Serlemitsos et al. 2007). We therefore utilized the *Chandra* data to detect point sources. The CIAO tool `wavdetect` (Freeman et al. 2002) was executed on the 0.5–7.0 keV *Chandra* ACIS images of each observations with a detection threshold of 5σ. The detected point sources are shown in black crosses of ACIS images in figure A.1. In following spectral analysis, point sources are excluded in circular regions of $1 - 2'$ radius depending on source brightness, as shown in the XIS images of figure A.1, where the lowest flux of the excluded point sources are set individually with clusters. The numbers of excluded point sources have roughly consistent numbers with the $\log N$–$\log S$ relation (Kushino et al. 2002).

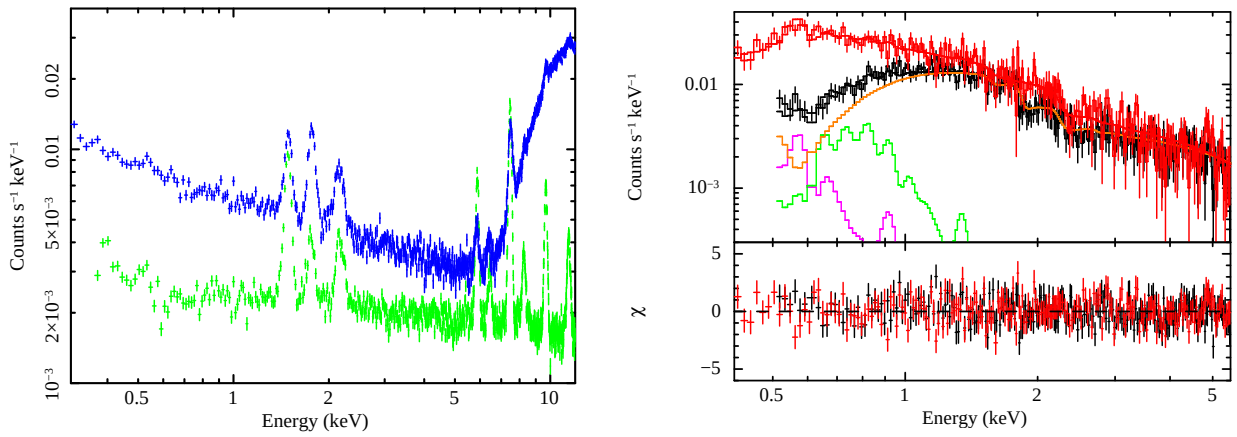

Figure 4.3: (Left) The typical NXB spectra of the XIS. Green and Blue are XIS-FI (averaged over XIS 0 and XIS 3) and XIS-BI spectra, respectively. (right) NXB-subtracted XIS spectra of the BGD region of MS 1512.4+3647, fitted with the X-ray background model. Black and red are 0.5–5.5 keV XIS-FI and 0.4–5.5 keV XIS-BI spectra, respectively. The CXB component is shown in orange line, and the LHB and MWH emissions are indicated by magenta and green lines, respectively.

4.5.3 Cosmic X-ray background

Even after the removal of point sources, there still remains contribution from unresolved extragalactic sources (CXB) to be evaluated as XRB. In the spectral analysis, an absorbed power-law model with a fixed photon index of 1.41 (Kushino et al. 2002) *wabs* × *powerlaw* was used as the CXB model, while the parameter of the normalization is determined by the model fitting (detailed in § 4.5.5).

4.5.4 Galactic foreground emission

GFE typically consists of unabsorbed (LHB; representing the local hot bubble and the solar-wind charge exchange) and absorbed (MWH; representing the Milky Way halo) plasmas. To reproduce the GFE, we employed two-temperature model, $apec_1 + wabs \times apec_2$, according to Tawa et al. (2008), where the *apec* model is a thin thermal plasma emission model detailed in Smith et al. (2001). The abundance of the two *apec* components were fixed to unity.

4.5.5 Spectral analysis of background region

In order to estimate the XRB, we extracted FI and BI spectra from a background region of the XIS image (BGD region in figure A.1). We fitted NXB-subtracted FI and BI spectra of the BGD region simultaneously with a model of $apec_1 + wabs \times (apec_2 + powerlaw)$ that represents the CXB and GFE emissions. Galactic absorption was fixed to the Galactic value (see table B.1). The ARFs of A^U were used for the model fitting.

As an example, the background spectra of MS 1512.4+3647 are shown in right panel of figure 4.3, and the best-fit parameters for the BGD region are summarized in table 4.1. The fit is moderately good with the probability that chi squared value becomes larger than the fitting value is 0.047.

The 2.0–10.0 keV surface brightness of the CXB component is $(5.09 \pm 0.12 \pm 0.27) \times 10^{-8}$ erg s^{-1}

Table 4.1: Results of Model Fittings to XIS spectra of the BGD region of MS 1512.4+3647 (shimoda et al. 2013).

LHB			MWH			CXB		
kT (keV)	$Norm^*$	$S^\dagger$	kT (keV)	$Norm^*$	$S^\dagger$	Γ	$S^\ddagger$	χ^2/dof
$0.12^{+0.04}_{-0.02}$	$1.60^{+1.54}_{-0.68}$	$3.91^{+3.62}_{-1.74}$	$0.26^{+0.05}_{-0.03}$	$0.32^{+0.16}_{-0.20}$	$3.70^{+1.70}_{-2.47}$	1.41 (fix)	$5.09^{+0.12}_{-0.12}$	492.0/441

* Normalization of the *apec* component divided by 400π which is the area of the circular region ($r = 20'$ in radius) used for the uniform-sky ARF calculation. $Norm = 1/400\pi \int n_e n_H dV/[4\pi(1+z)^2 D_A^2] \times 10^{-20}$ cm^{-5} arcmin^{-2}, where D_A is the angular diameter distance to the source.

† The 0.5–1.0 keV surface brightness in units of 10^{-9} erg s^{-1} cm^{-2} sr^{-1}.

‡ The 2.0–10.0 keV surface brightness in units of 10^{-8} erg s^{-1} cm^{-2} sr^{-1}.

cm^{-2} sr^{-1} (90% statistical and systematic errors), where the systematic error of 5.4% is derived by scaling the fluctuation analysis with Ginga (Hayashida 1989) to our flux limit and FOV of 1.6×10^{-14} erg s^{-1} cm^{-2} and 0.06 deg^2, respectively (detailed in Hoshino et al. 2010; Akamatsu et al. 2011). This CXB fluctuation is consistent with Nakazawa et al. (2009) scaled by HEAO-1, -2 results.

The temperature and surface brightness of LHB are $kT = 0.12^{+0.04}_{-0.02}$ keV and $(3.91^{+3.62}_{-1.74}) \times 10^{-9}$ erg s^{-1} cm^{-2} sr^{-1} in 0.5–1.0 keV energy range, respectively. Those of MWH are $kT = 0.26^{+0.05}_{-0.03}$ keV and $(3.70^{+1.70}_{-2.47}) \times 10^{-9}$ erg s^{-1} cm^{-2} sr^{-1} in 0.5–1.0 keV energy range, respectively. The obtained temperatures of LHB and MWH are consistent with typical values of these GFE components (Lumb et al. 2002; Yoshino et al. 2009). The background spectrum of the other clusters is well reproduced by the same model as above discussion.

4.6 Radio Data

In order to obtain total mass of clusters, we referred the results of *Planck* (Tauber et al. 2010; Planck Collaboration 2011a), which is the satellite for all sky survey with radio band. *Planck* was launched 2009 by European Space Agency, and observes the sky in nine frequency bands covering 30–857 GHz with high sensitivity and angular resolution from $31'$ to $5'$.

Planck measured the total mass of 62 nearby ($z < 0.5$) clusters of galaxies using Sunyaev-Zel'dovich effect (Planck Collaboration 2011b). 20 clusters in our samples are included in Planck Collaboration (2011b) and the total mass of them are listed in table B.2. We plotted the total mass of our samples as a function of redshift in figure 4.4. We use the total mass to discuss about metal evolutions with mass-selected samples.

4.7 Optical Data

4.7.1 Sloan Digital Sky Survey

In order to obtain member galaxy information of the clusters, we utilized public data from the SDSS. The SDSS used a dedicated 2.5-meter telescope at Apache Point Observatory, New Mexico.

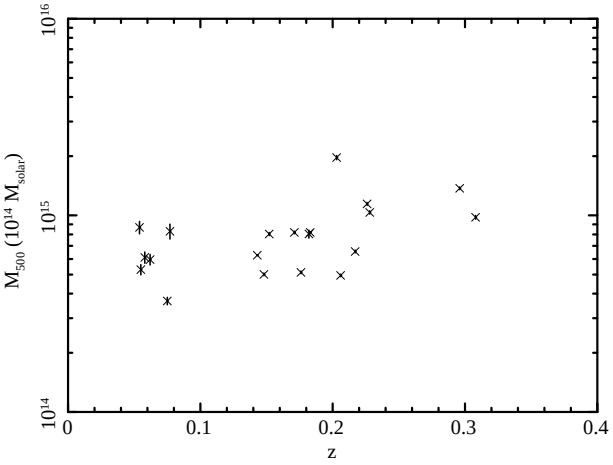

Figure 4.4: Redshift distribution of the total mass, which is measured with *Planck*, in our samples.

The 120-megapixel camera imaged 1.5 square degrees of sky at a time. SDSS is continuing the sky survey from the year 2000 and has released 1,880,584 galaxies data with 35% sky coverage.

I utilize the latest data base of the SDSS, Data Release 10 (DR10). 28 of 62 clusters in our samples were observed with SDSS, and we extracted the information of the member galaxies in the clusters from SkyServer DR10[1].

4.7.2 Calculation of luminosity

I obtain information on i and g bands magnitude and positions of galaxies form the SDSS database. The radius of data extraction is set to virial radius (summarized in table B.1). Figure A.3 shows the color magnitude diagram (CMD) for all samples. Because the CMD shows a tight color-magnitude (CM) sequence of early-type member galaxies (Okabe & Umetsu 2008), I quantify the CM sequence of galaxies with a linear relation in CM space. I set the maximum magnitude to i, $g = 22$. The results of a linear relation are summarized in table B.5 and shown by black dashed lines in figure A.3. For the member galaxies, I transform the apparent magnitude $m_{\rm b}$ of each bands to absolute magnitude $M_{\rm b}$ as

$$M_{\rm b} = m_{\rm b} - 25 - 5\log_{10}\left(\frac{D_{\rm L}}{1\ {\rm Mpc}}\right) - A_{\rm b} - k_{\rm b}, \tag{4.1}$$

where $D_{\rm L}$ is the luminosity distance of the cluster, $A_{\rm b}$ denotes Galactic extinction, and $k_{\rm b}$ is the k-correction of each band. Above equation, I assumed that all galaxies have same redshift. For the k-correction, I utilized k-correction caluculator[2] (Chilingarian, Melchior & Zolotukhin 2010; Chilingarian & Zolotukhin 2012). The Galactic extinction values are obtained from the NED[3]. For the convenience, I converted the absolute magnitude to the luminosity as,

$$\frac{L_{\rm b}}{L_{\rm solar}} = \sqrt[5]{100}^{M_{\rm b}-M_{\rm solar}}, \tag{4.2}$$

[1]http://skyserver.sdss3.org/dr10/en/home.aspx
[2]http://kcor.sai.msu.ru/
[3]http://ned.ipac.caltech.edu/forms/byname.html

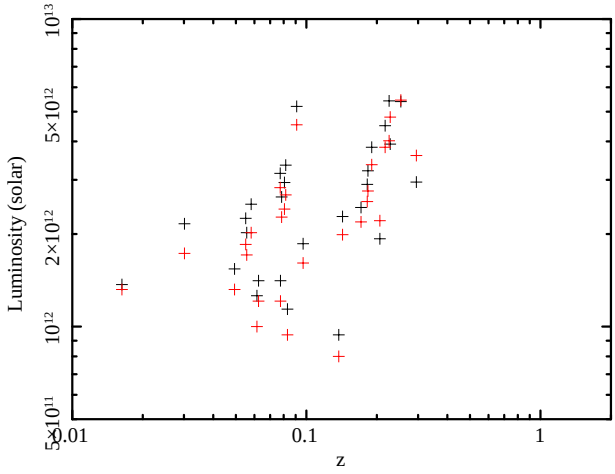

Figure 4.5: Redshift distribution of the optical luminosity. Black and red denote i and g band, respectively.

where $L_{\rm solar}$ is the solar luminosity, and I assume that absolute solar magnitude of i of g band is $M_{i,\rm solar} = 4.58$ or $M_{g,\rm solar} = 5.45$ (Blanton et al. 2003), respectively. I derived the luminosity of the cluster of galaxies to integrate the luminosities of member galaxies.

The luminosity of clusters is thought to be contaminated by field galaxies. I estimated the background luminosity density from an annular region outside of the cluster region (2–4 Mpc annular region from the center), and subtracted the background contribution from the luminosity density of the cluster.

To derive the total luminosity, I need to consider the dark galaxies which are not detected due to the magnitude limit of the observatory. According to the Okabe & Umetsu (2008), I assume that the member galaxies follow a Schechter luminosity function (Scechter 1976) of the form:

$$\phi(L) = \frac{\phi^*}{L^*}\left(\frac{L}{L^*}\right)^{-p}\exp(-L/L^*). \tag{4.3}$$

Where the ϕ^* is a number per unit volume and L^* is a characteristic luminosity (Schechter 1976). By integrating equation 4.3 down to the luminosity cutoff, $L_{\rm limit}$, Okabe & Umetsu (2007) obtained the relation between the total luminosity $L_{\rm total}$ and the observed luminosity $L_{\rm obs}$:

$$\frac{L_{\rm total}}{L_{\rm obs}} = \frac{\Gamma(2-p)}{\Gamma(2-p, L_{\rm limit}/L^*)}, \tag{4.4}$$

where $\Gamma(a,x)$ is the upper incomplete gamma function. I adopt the parameter values for the luminosity function by Goto et al. (2002), $p = 0.70$ and $M^* = -22.31 + 5\log(h_{70})$ in i band or $p = 1.00$ and $M^* = -22.01 + 5\log(h_{70})$ in g band, respectively, where M^* is the absolute magnitude corresponding to the characteristic luminosity L^*. The results of $L_{\rm total}/L_{\rm obs}$ are summarized in table B.5. Finally I derived background subtracted and corrected luminosities of 28 clusters of galaxies and summarized it in table B.5. Figure 4.5 shows redshift distribution of the total luminosities.

Chapter 5

SPECTRAL ANALYSIS AND RESULTS

5.1 Spectral Analysis

In order to investigate the chemical property of individual ICM, we extracted XIS spectra within circular regions of 0.3–0.6r_{200}, indicated as SRC regions (white solid circles) in figure A.1. Each center of circle was placed at the X-ray emission centroid in the *Chandra* ACIS image. The radius of extraction was set 0.6 r_{200} or smaller (0.3 r_{200} at minimum) depending on each size of observed region. The point sources within the SRC region were detected according to the method described in subsection 4.5.2 and masked (white dashed circles in figure A.1). After extracting spectra of the XIS 0, XIS 1, and XIS 3, we created a single XIS-FI spectra by averaging the XIS 0 and XIS 3 spectra for each object. When the *Suzaku* observations are separated because of bigger apparent size than the XIS FOV, we created a single XIS-FI or BI spectra by averaging the XIS-FI or BI spectra of each region.

Left panel of figure 5.1 exemplifies the comparison of raw SRC spectra (black for XIS-FI and red for XIS-BI) with corresponding NXB spectra (green and blue) in case of ABELL 0262. The raw SRC spectra exhibit significant excess in 0.4–7.0 keV (XIS-FI) and 0.3–7.0 keV (XIS-BI), respectively, due to the ICM and XRB emission. In higher energy band than 7.0 keV, the NXB dominates the raw SRC spectra. Right panel of figure 5.1 is NXB-subtracted SRC spectra (black for XIS-FI and red for XIS-BI) with the best-fit XRB model for each BGD region described in subsection 4.5.5. The signal from ICM is significantly detected in 0.5–6.5 keV (XIS-FI) and 0.4–6.5 keV (XIS-BI), respectively, in the case of ABELL 0262. The emission lines from ions, e.g. redshifted Fe-K line, are prominently seen in the spectra of right panel of figure 5.1. These lines are seen clearly in each atomic-line energy of Ne, Mg, Si, S, Fe, and Ni shown in figure 5.2, where we fitted the NXB-subtracted SRC spectra with $wabs \times bremss$+XRB model.

In order to determine metal abundances, the NXB-subtracted XIS-FI and XIS-BI SRC spectra were fitted with an absorbed single-temperature (1T) thin-thermal emission model, $wabs \times vapec$ (*vapec*: Smith et al. 2001) in addition to the XRB model (subsection 4.5.5) as shown in figure A.2.

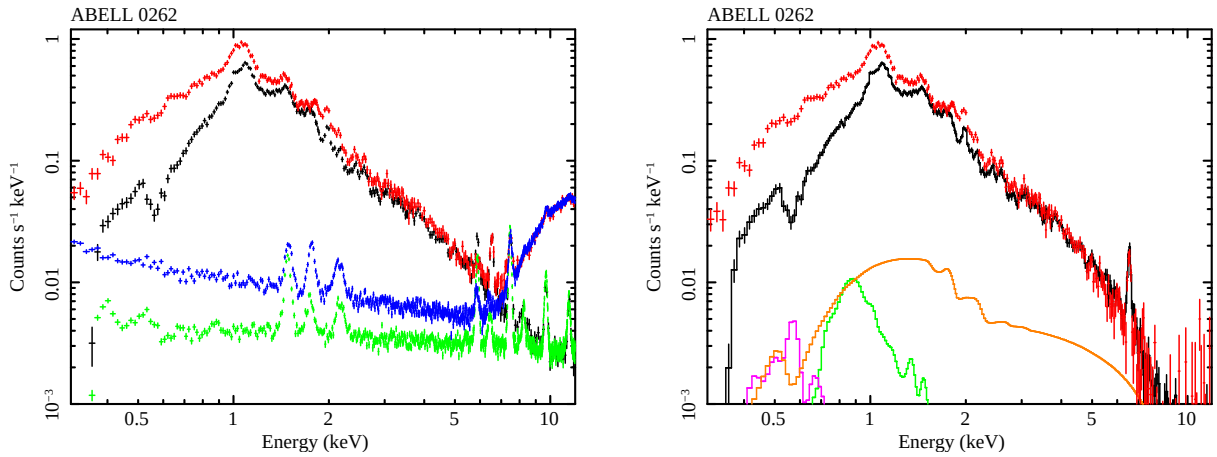

Figure 5.1: (Left) Raw XIS spectra of the SRC region and NXB spectra extracted from the same region. Black and red crosses are 0.3—12.0 keV XIS-FI (averaged over XIS 0 and XIS 3) and XIS-BI raw spectra, respectively, and green and blue crosses are XIS-FI and XIS-BI NXB spectra, respectively. (right) NXB-subtracted spectra of the SRC region with the best-fit X-ray background model described in subsection 4.5.5

The lower energy range for the model fitting was basically set to 0.5 keV for XIS-FI or 0.4 keV for XIS-BI and upper is set to the energy of $\sim 3\sigma$ significance than the NXB spectrum. In this fitting, the BGD spectra (e.g. right panel of figure 4.3) were simultaneously fitted with the same XRB model to determine the XRB in the SRC region. For the SRC spectra, we utilized the NXB and response (RMF and ARF) files of the SRC region (section 4.3), while those of the BGD region were used for the BGD spectra. The discrepancy of integration radii and telescope response for the SRC and XRB emissions are compensated with dedicated ARFs. The β-model ARF, A^{I}, and the uniform sky ARF, A^{U}, were assigned to the XRB and the ICM model components, respectively. Among 12 metal abundance parameters of *vapec*, we set $Z_{\rm He} = Z_{\rm C} = Z_{\rm N} = Z_{\rm O} = Z_{\rm solar}$ ($Z_{\rm metal}$ denote the metal abundance in solar unit) because these emission line energies from these elements are out of range in the case of distant clusters or difficult to determine because of low sensitivity of the XIS below 0.5 keV. Emission lines from Al, Ar, and Ca are not significantly detected (e.g. figure 5.2). Then we set $Z_{\rm S} = Z_{\rm Ar} = Z_{\rm Ca}$, and set $Z_{\rm Al}$ as free parameter, which is no a α element. We also examined two cases: 1) free parameters of $Z_{\rm S}$, $Z_{\rm Ar}$, and $Z_{\rm Ca}$, 2) linked parameters of $Z_{\rm Mg} = Z_{\rm Al}$. For example, the errors of $Z_{\rm S}$ and $Z_{\rm Mg}$ increased about 5% in the case 1) and 10% in the case 2), respectively, in the case of MS 1512.4+3647. The other abundances, $Z_{\rm Ne}$, $Z_{\rm Si}$, $Z_{\rm Fe}$, and $Z_{\rm Ni}$, were left free in the fitting procedure. Consequently, we had seven free metal-abundance parameters. The hydrogen absorption column density was fixed to the Galactic value and redshift was also fixed (table B.1). In the model fitting procedure of XRB, all parameters were left free except for the photon index of the power-law shaped CXB model (section 4.5.3), while the temperature of LHB was fixed to 0.08 keV in a few clusters because of the low statistics. The obtained best-fit parameters temperature, metal abundances, and reduced chi-square, are summarized in table B.3. The Al abundance is not determined significantly. The elements which below 3σ significance are not referred in table B.3

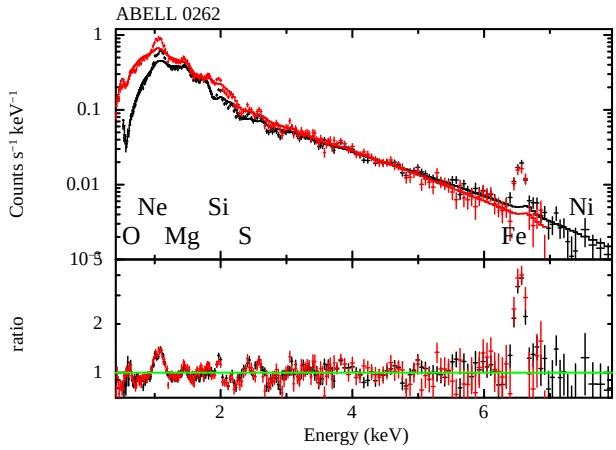

Figure 5.2: XIS-FI (black) and XIS-BI (red) spectra around the O, Ne, Mg, Si, S, Fe and Ni emission lines extracted from the SRC region, with the best-fit $wabs \times bremss$ model (solid lines). The positions of the redshifted metal lines are also indicated. The lower panel shows the ratio of the data to model.

Table 5.1: Fitting results of 2T model.

ID	Cluster	kT_1 [keV]	kT_2 [keV]	Fe [solar]	χ^2/d.o.f.*
12	ABELL 3667	$6.56^{+0.10}_{-0.09}$	$0.59^{+0.02}_{-0.02}$	$0.39^{+0.03}_{-0.02}$	1113.7/883
38	ABELL 0665	$8.43^{+0.63}_{-0.68}$	$1.32^{+0.05}_{-0.04}$	$0.23^{+0.07}_{-0.07}$	1121.0/804
47	ABELL 2667	$7.10^{+0.49}_{-0.51}$	$1.39^{+0.04}_{-0.03}$	1141.8/831	

* degree of freedom.

except for Fe abundance.

The ICM is considered to have temperature structures, especially between the core and outer regions (e.g. Sato et al. 2009a). If this is true, a multi-temperature model may reproduce the SRC spectra better. We tried a two-temperature model (2T), $wabs \times (vapec + vapec)$. In this model, each metal abundance was tied between the two thermal components. Therefore, in the 2T model, only one temperature parameter was added as a new free parameter to the 1T model. We utilized the F-test to check the 2T model at the 5% significance level, and summarized the fitting results in table 5.1 in case that 2T model improved the fitting. Three clusters of galaxies, ABELL 3667, ABELL 0665, and ABELL 2667, are improved the fitting in 2T model. The temperature and the $Z_{\rm Fe}$ were changed less than $< 5\%$ and the normalization of the low temperature component was two orders smaller than that of the high temperature component (also smaller than that of BGD components). Thus we conclude that the low temperature component is not affect the metal abundances and we do not use the results of 2T model fitting in following analysis.

Table 5.2: Results of model fittings including systematic errors in the case of MS 1512.4+3647 (shimoda et al. 2013).

Model	kT (keV)	Si (solar)	S=Ar=Ca (solar)	Fe (solar)	Ni (solar)	χ^2/d.o.f.
1T[a]	$3.28^{+0.09}_{-0.09}$	$0.63^{+0.21}_{-0.20}$	$0.42^{+0.23}_{-0.23}$	$0.64^{+0.08}_{-0.07}$	$1.94^{+1.06}_{-1.02}$	1087.8/1014
CXB−6%[b]	$3.30^{+0.08}_{-0.09}$	$0.64^{+0.21}_{-0.20}$	$0.42^{+0.23}_{-0.23}$	$0.65^{+0.08}_{-0.08}$	$2.02^{+1.07}_{-1.03}$	1095.0/1015
CXB+6%[c]	$3.29^{+0.09}_{-0.04}$	$0.64^{+0.21}_{-0.23}$	$0.42^{+0.21}_{-0.21}$	$0.64^{+0.04}_{-0.07}$	$1.94^{+1.04}_{-0.76}$	1083.3/1015
NXB±3%[d]	$3.28^{+0.08}_{-0.09}$	$0.63^{+0.21}_{-0.20}$	$0.42^{+0.23}_{-0.23}$	$0.64^{+0.08}_{-0.07}$	$1.94^{+1.06}_{-1.02}$	1080.8/1014
CONTAMI−10%[e]	$3.38^{+0.11}_{-0.09}$	$0.74^{+0.23}_{-0.21}$	$0.51^{+0.25}_{-0.24}$	$0.64^{+0.08}_{-0.08}$	$1.99^{+1.09}_{-1.06}$	1092.3/1014
CONTAMI+10%[f]	$3.19^{+0.04}_{-0.09}$	$0.55^{+0.20}_{-0.19}$	$0.35^{+0.22}_{-0.21}$	$0.64^{+0.08}_{-0.07}$	$1.93^{+1.04}_{-1.00}$	1092.8/1014

[a] Single temperature model.
[b] The normalization of CXB model is changed −6%.
[c] The normalization of CXB model is changed +6%.
[d] The systematic error of ±3% is included in the NXB spectra.
[e] The contamination thickness of ARFs is changed −10%.
[f] The contamination thickness of ARFs is changed +10%.

5.2 Systematic Errors

5.2.1 Background and contamination estimation

The systematic errors of above obtained values were evaluated by varying the backgrounds or the contamination on the blocking filter within each accuracy of estimation. We repeated the spectral fit by changing the NXB intensity by ±3%. The error due to the CXB intensity fluctuation was also examined by varying the CXB normalization by 6%, which was derived by scaling the Ginga results with the XIS sensitivity and the field of view (subsection 4.5.5). The systematic error in the contamination thickness of the XIS blocking filter is typically 10% (The *Suzaku* Technical Description[1]), and we evaluated its effect through spectral fits by adjusting the detector response which included the contamination thickness. As an example, the results of MS 1512.4+3647 are summarized in table 5.2. The temperature and abundances did not change significantly by these systematic uncertainties. We employed the systematic errors of NXB $\sigma_{\rm NXB}$, CXB $\sigma_{\rm CXB}$, and contamination $\sigma_{\rm CONTAMI}$, by examining the change of the fitted parameters in table 5.2. As a result, $\sigma_{\rm CXB}$ and $\sigma_{\rm NXB}$ are always less than 10% of the statistical errors, and $\sigma_{\rm CONTAMI}$ is comparable to the statistical error for the temperature and roughly 50% of that for the abundances of Ne, Mg, Si and S. In the following analysis we used the error defined by $\sigma_{\rm error} = (\sigma^2_{\rm STATISTICAL}+\sigma^2_{\rm NXB}+\sigma^2_{\rm CXB}+\sigma^2_{\rm CONTAMI})^{1/2}$.

5.2.2 Model dependence

In above spectral analysis, we utilized the *wabs* as the Galactic hydrogen absorption model. The *wabs* has been widely used for the X-ray analysis of clusters of galaxies. The solar abundance table employed in the *wabs* model was that derive by Anders & Ebihara (1982), while the table by Lodders (2003) is used as a solar abundance table for the *apec* model in our spectral analysis.

[1] http://www.astro.isas.ac.jp/suzaku/doc/suzaku_td/suzaku_td.html

Table 5.3: Results of model fittings with different abundance table in the case of ABELL 0262.

Model	kT (keV)	Ne (solar)	Mg (solar)	Si (solar)	S=Ar=Ca (solar)	Fe (solar)	Ni (solar)	χ^2/d.o.f.
case 1)	$2.12^{+0.02}_{-0.02}$	$1.60^{+0.23}_{-0.22}$	$0.47^{+0.08}_{-0.07}$	$0.46^{+0.04}_{-0.04}$	$0.46^{+0.05}_{-0.05}$	$0.51^{+0.02}_{-0.02}$	$0.34^{+0.17}_{-0.15}$	1150.9/939
case 2)	$2.23^{+0.04}_{-0.05}$	$2.07^{+0.23}_{-0.22}$	$0.60^{+0.09}_{-0.09}$	$0.54^{+0.04}_{-0.05}$	$0.49^{+0.06}_{-0.05}$	$0.55^{+0.02}_{-0.02}$	$0.52^{+0.19}_{-0.17}$	1192.0/939

We thus evaluated the possible discrepancy due to these two different solar abundance tables in the Galactic hydrogen absorption model: case 1), *wabs* model with Anders & Ebihara (1982), which is a nominal case of our analysis; case 2), *phabs* model with Lodders (2003), where *phabs* is one of the Galactic hydrogen absorption model and can change the solar abundance table. The result is shown in table 5.3 in the case of ABELL 0262. Case 2 shows higher value by 10–20% than those in case 1.

5.2.3 Radial dependence of metal abundances

Discussing the metal enrichment histories, we are interested in the average metal abundances in the ICM. In fact, radial gradient is observed for the metal abundances in number of clusters of galaxies (e.g. Leccardi & Molendi. 2008; Matsushita et al. 2012). We checked the systematic errors of the average metal abundances by comparing the result between spatially resolved analysis and our averaged analysis within 0.3 r_{200}.

As an example, here we select ABELL 0262. The integrated mass of the ICM in ABELL 0262 is estimated by 3-dimentional β-model,

$$\rho_{\rm gas}(r) = \rho_0 \left(1 + \frac{r}{r_{\rm core}}\right)^{-3\beta/2}, \tag{5.1}$$

with the parameters by Vikhlinin et al. (2006). Where ρ and r are gas density and radius from cluster center, respectively. The integrated mass of the ICM within 0.3 r_{200} is estimated as $M_{\rm gas} = 3.18 \times 10^{12}$ $\rm M_{solar}$ by integrating the 3-dimensional β-model. Based on the metal abundances and the estimated mass of the ICM, we calculate the mass of Fe as

$$\rho_{\rm Fe}(r) = Z_{\rm Fe}(r) \times \rho_{\rm gas}(r). \tag{5.2}$$

Adopting a β-model for the metal abundance profile, we calculate the integrated metal abundance within 0.3 r_{200} as,

$$Z_{\rm metal}(r) = Z_0 \left(1 + \frac{r}{r_{\rm core}}\right)^{-\alpha} \tag{5.3}$$

(De Grandi et al. 2004). The parameters are derived by fitting the above equation to the Fe profile in Sato et al. (2009b). Consequently, the integrated mass of Fe within 0.3 r_{200} is estimated as $M_{\rm Fe} = 1.35 \times 10^9$ $\rm M_{solar}$ by integrating $\rho_{\rm Fe}(r)$. The mass ratio is derived as $M_{\rm Fe}/M_{\rm gas} = 4.24 \times 10^{-4}$, which is corresponding to the metal abundance, $Z_{\rm Fe} = 0.26$ $Z_{\rm solar}$ referring the solar abundance table by Lodders (2003). On the other hand, our averaged analysis derived an Fe abundance, $Z_{\rm Fe} = 0.51$ $Z_{\rm solar}$. This is a large value of factor of 2 than one of the above estimation. The normalizations of the metal abundance evolutions are changed but the trend is not changed by this analysis method.

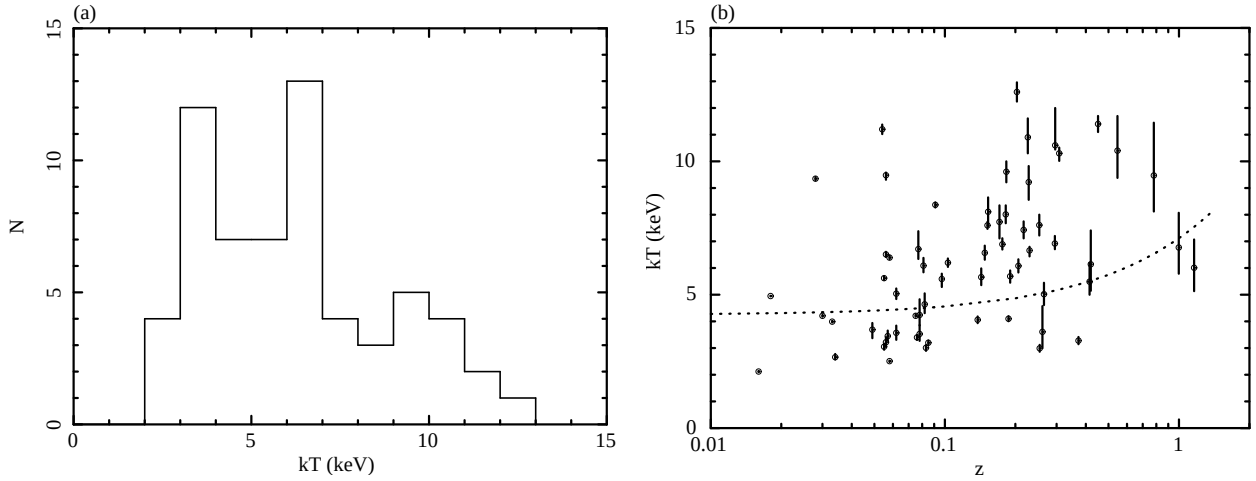

Figure 5.3: (a) Histogram of the temperature distribution of the sample. (b) Temperature plotted vs. redshift for the whole sample. Black dashed line indicates best-fit power-law model.

5.3 Temperature Evolution

From the spectral analysis of *Suzaku* data, we measured the average ICM temperature of 62 clusters of galaxies. Histograms of the temperature distribution of the sample is shown in panel (a) of figure 5.3. Most of our samples are hot clusters ($5 < kT$ keV), while 19 and 4 clusters are in the medium ($3 < kT < 5$ keV) and low ($kT < 3$ keV) temperature, respectively. Panel (b) of figure 5.3 shows the distribution of temperatures in our sample as a function of redshifts. According to the above plots, we used 1T fitting results as the temperature for the 2T clusters. The Spearman's test shows significant positive correlation between temperature and redshift with Spearman's rank coefficient of $r_{\rm s} = 0.42$ for 60 degrees of freedom and probability of null correlation $p = 1.71 \times 10^{-4}$ (table 5.4). Black dashed line in figure 5.3(b) indicates the results of simple power-law fitting, $T(z) = T_0(1+z)^{\alpha}$, with $\alpha = 0.74 \pm 0.04$. This correlation indicates that the data of higher temperature is increasing toward higher redshift.

5.4 Metal Abundance Evolutions

In order to discuss the metal evolution of each cluster of galaxies, we plot the metal abundances against several parameters (redshift, temperature, total mass, optical luminosity, Abell's richness classes, Bauts-Moragan type) which thought to trace the age of clusters. We also try Spearman's test to check the correlation with the parameters in the case of d.o.f.> 9, and the results are summarized in table 5.4. In case that null correlation probability is less than $p < 25\%$, we fit simple power-law model and summarized power index in table 5.4.

Redshift dependence Figure 5.4 shows the 3 σ detected metal abundance, and the upper limit of $Z_{\rm Fe}$ of SPT-CL J0546-5345 against their redshift. The iron abundance, $Z_{\rm Fe}$, in the ICM was determined $z \sim 1$, but the other abundances reach only medium distant ($z \sim 0.4$ for Si, S and Ni),

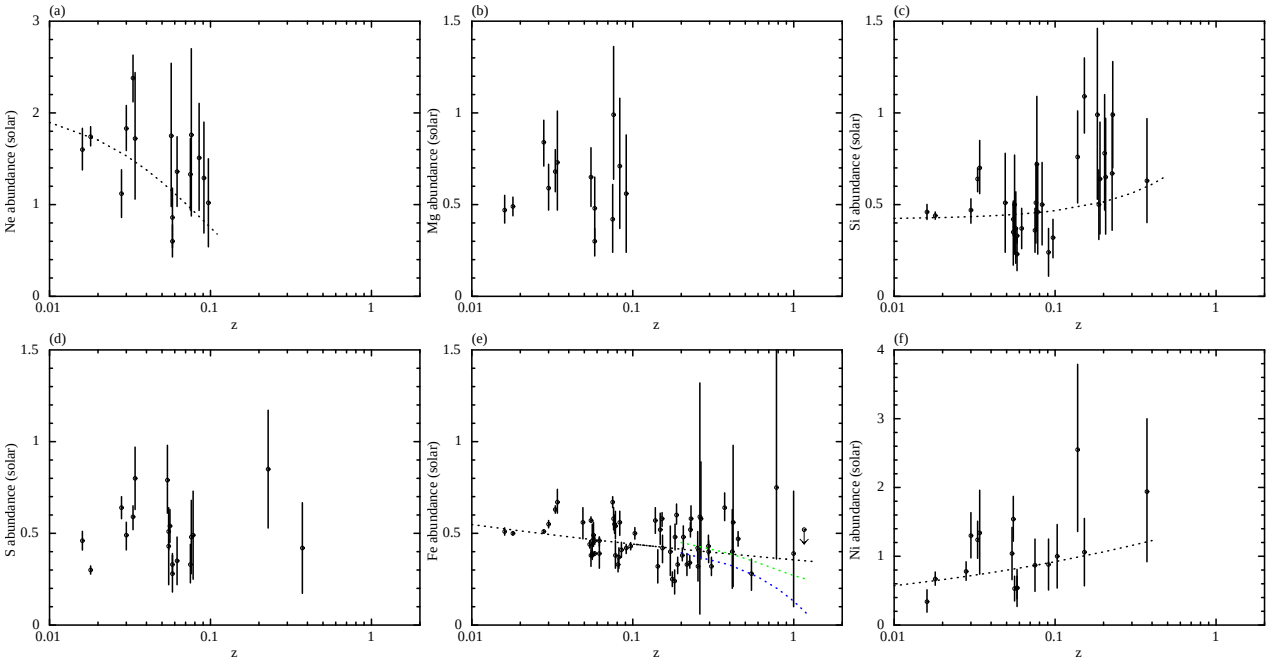

Figure 5.4: Metal abundances of Ne, Mg, Si, S, Fe and Ni plotted versus redshift. The black dashed line indicates best-fit value by simple power-law model. The green dashed line and blue dashed line denote the results of Balestra et al. (2007) and Anderson et al. (2009), respectively.

or nearby ($z \sim 0.1$ for Ne and Mg), respectively. The metal abundances of Ne, Mg, S and Ni show constant values of $Z_{\rm Ne} \sim 1.5$ solar, $Z_{\rm Mg} \sim 0.6$ solar, $Z_{\rm S} \sim 0.5$ solar, and $Z_{\rm Ni} \sim 1.0$ solar, respectively (panel (a), (b), (d) and (f) of figure 5.4), although these abundances are not measured from distant clusters. In contrast, as shown in figure 5.4(c), $Z_{\rm Si}$ exhibits a significant increase by a factor of 50% in the range of $z = 0$ to $z \sim 0.3$. On the other hand, $Z_{\rm Fe}$ are halved from $z = 0$ to $z \sim 0.5$. We conducted the Spearman's test to figure 5.4 and summarized the results in table 5.4. The result shows positive correlation for $Z_{\rm Si}$ and $Z_{\rm Ni}$, while $Z_{\rm Ne}$ and $Z_{\rm Fe}$ show weak negative correlation. We fit metal abundances versus redshift relation with simple power-law model, $Z_{\rm metal}(z) = Z_{\rm metal,0}(1+z)^{\alpha}$, (summarized in table 5.4) and plotted on figure 5.4 (black dashed line). The trend of $Z_{\rm Fe}$ shows a shallower slope than *Chandra* and *XMM-Newton* results (Balestra et al. 2007; Maughan et al. 2008; Anderson et al. 2009) with $\alpha \sim 1.25$ as shown in figure 5.4(e) (green dashed line: Balestra et al. 2007, blue dashed line: Anderson et al. 2009).

Temperature dependence Figure 5.5 shows best-fit metal abundances values against the temperature of the ICM for the whole sample. According to panel (b) and (f) of figure 5.5, $Z_{\rm Mg}$ and $Z_{\rm Ni}$ have no significant correlation with ICM temperature, where these metal abundances are largely scattered and number of samples are lower than the other abundances. On the other hand, $Z_{\rm Si}$ and $Z_{\rm S}$, mainly synthesized in SNe cc, show positive correlation with ICM temperature (panel (c) and (d) of figure 5.5). $Z_{\rm Si}$ and $Z_{\rm S}$ become two times larger above ~ 10 keV than that of ~ 3 keV. Alternatively, $Z_{\rm Fe}$, which is mainly synthesized with SNe I, shows negative correlation (panel (e) of

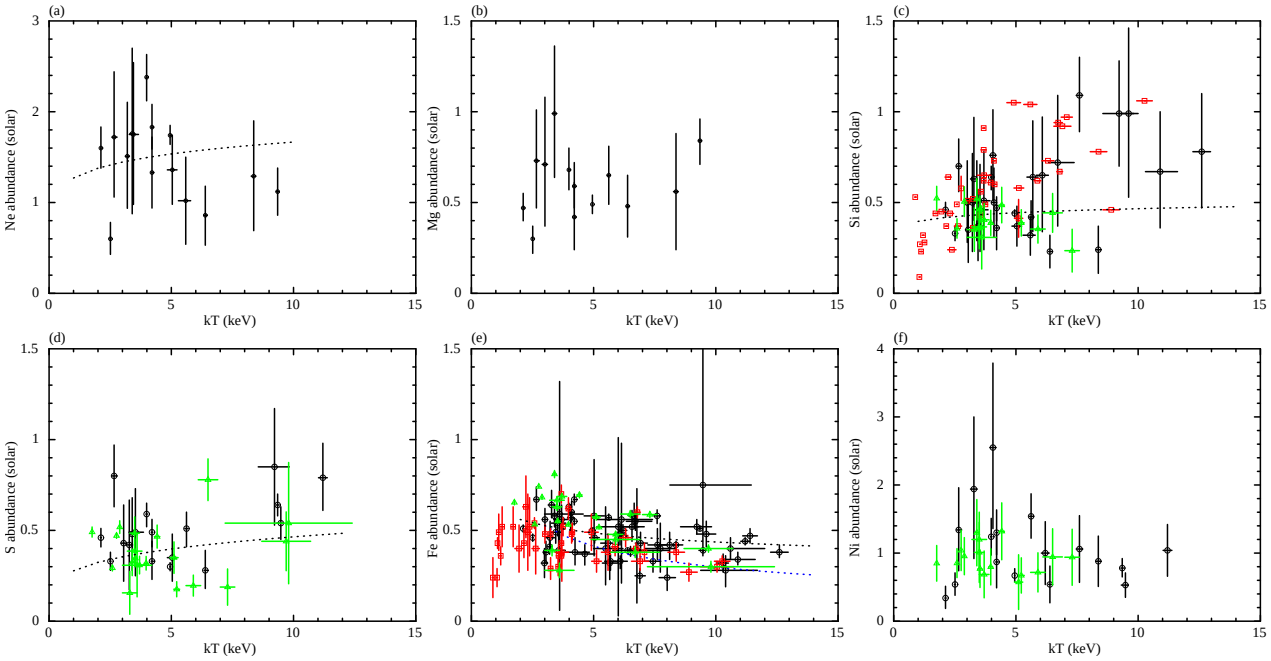

Figure 5.5: Metal abundances plotted as a function of the ICM temperature (black circle). Black dashed line indicates the best-fitted model assuming a simple power-law model. Red square, green triangle, and blue dashed line indicate the results of Fukazawa et al. (1998), de Plaa et al. (2007) and Balestra et al. (2007), respectively.

figure 5.5). This abundances drops 50% from ~ 3 keV to ~ 10 keV. We tried to Spearman's test for all metal abundances, $Z_{\rm Si}$ and $Z_{\rm S}$ show weak positive correlation with the temperature, while $Z_{\rm Ne}$ and $Z_{\rm Fe}$ show negative correlation (table 5.4). When We fit by simple power-law model, the parameters are summarized in table 5.4. The negative correlation of $Z_{\rm Fe}$ is seen in *Chandra* results reported by Balestra et al. (2007) with $Z_{\rm Fe}(0) = 0.88^{+0.5}_{-0.2}$ and $\alpha = -0.47^{+0.1}_{-0.2}$ (green dashed line in panel (e) of figure 5.5). Same trend of $Z_{\rm Si}$ and $Z_{\rm Fe}$ with ICM temperature were reported by Fukazawa et al. (1998) with *ASCA* measurements. The $Z_{\rm Si}$ and $Z_{\rm Fe}$ of Fukazawa et al. (1998) are converted to the value of Lodders (2003) and plotted on the panel (c) and (e) of figure 5.5 (red square), where the error bar of $Z_{\rm Si}$ is not plotted because of larger error bars than the range of y-axis. The resuls of de Plaa et al. (2007) with *XMM-Newton* are superposed in panel (c)–(f) of figure 5.5 (green triangle). This literature reports the metal abundances of nearby 22 clusters ($0.02 < z < 0.18$) in the central region ($< 0.2\ r_{500} \sim 0.1\ r_{200}$). The abundances of $Z_{\rm S}$, $Z_{\rm Fe}$, and $Z_{\rm Ni}$ show the same tendency as our results. The difference in trends of $Z_{\rm Si}$ between de Plaa et al. (2007) and our results indicates that $Z_{\rm Si}$ shows low value around the center ($< 0.1\ r_{200}$) of the ICM.

Total mass dependence Clusters of galaxies thought to evolve to larger systems by collision and merging of clusters. That naturally implies the systems which have larger total mass are older than smaller ones. Here we assumed that the total mass traces the age of the cluster, as shown in figure 5.6. The total mass information within r_{500} are retrieved from Planck Collaboration (2013)

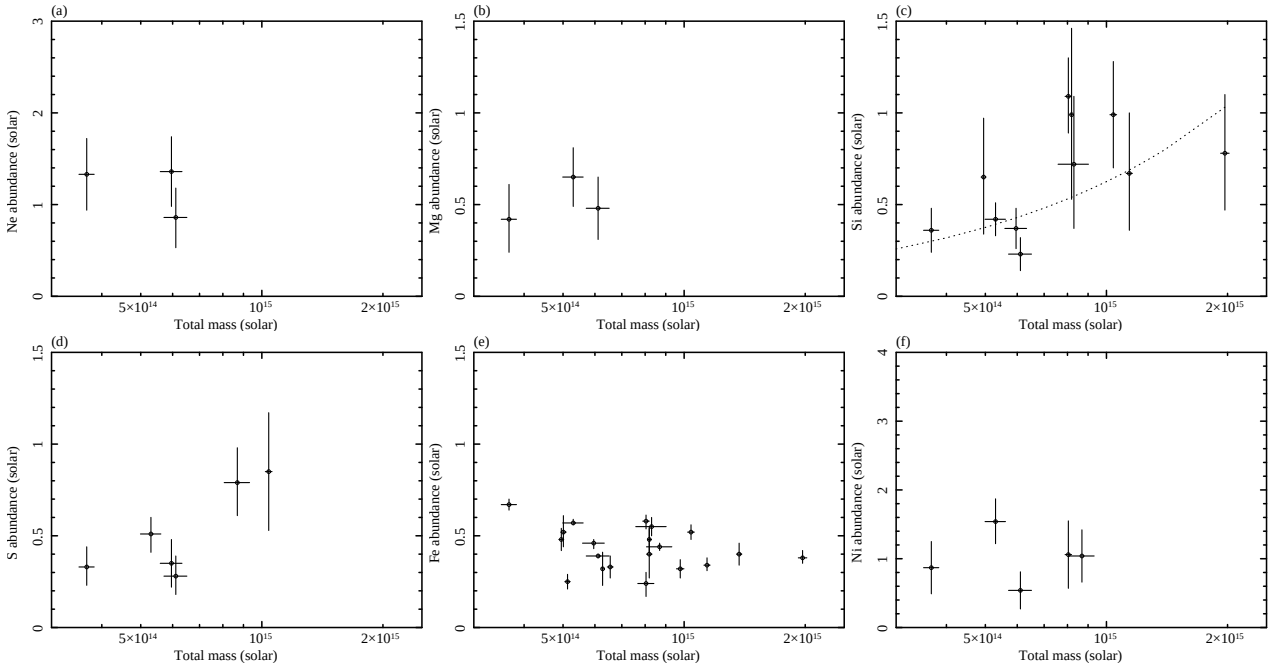

Figure 5.6: (a)–(f) Total mass versus the metal abundances. In panel (c) and (e), black dashed line indicate best-fit model.

(section 4.6). We see no significant trend in figure 5.6(a), (b), (d) nor (f), due to the limited statistics. In panel (c) of figure 5.6, $Z_{\rm Si}$ increases by a factor of two toward heavier systems. For the $Z_{\rm Si}$, Spearman's test shows significant positive correlation with $r_{\rm s} = 0.61$ and $p = 0.02$ (table 5.4). The best-fit value of simple power-law model is $\alpha = 0.74 \pm 0.05$. On the other hand, $Z_{\rm Fe}$ decreases by 40%. Spearman's test for the $Z_{\rm Fe}$ vs. total mass relation are tested and we see no significant correlation with $p = 0.51$.

Galaxy luminosity dependence The metal abundances have close ties to the optical luminosity, because the metals in the ICM have synthesized in the member galaxies. Here the metal abundances are plotted as a function of optical i band luminosity. The deviation of optical luminosity is detailed in section 4.7. In panel (a)–(f) of figure 5.7, the metal abundances are plotted as a function of the i band optical luminosity. The metal abundances show constant value about 0.5 $Z_{\rm solar}$ with luminosity, except for $Z_{\rm Fe}$. $Z_{\rm Fe}$ shows shallow slope toward large luminosity, but shows clear decline about 30%. Actually, We applied Spearman's test to figure 5.7. The results show significant negative correlation for only $Z_{\rm Fe}$ (table 5.4) with a power index of $\alpha = -0.18 \pm 0.01$.

Abell's richness classes dependence The Abell's richness classes (Abell 1958; Abell, Corwin. Jr & Olowin 1989) are used as reference of the age here. The definition of richness class is in subsection 2.2.3. The value of richness classes are obtained from NED and summarized in table B.1. It is notable a attention that the observatory is not same over the database and consequently each evaluated Abell's richness classes depend on the limiting magnitude of each observatory. Panel (a)

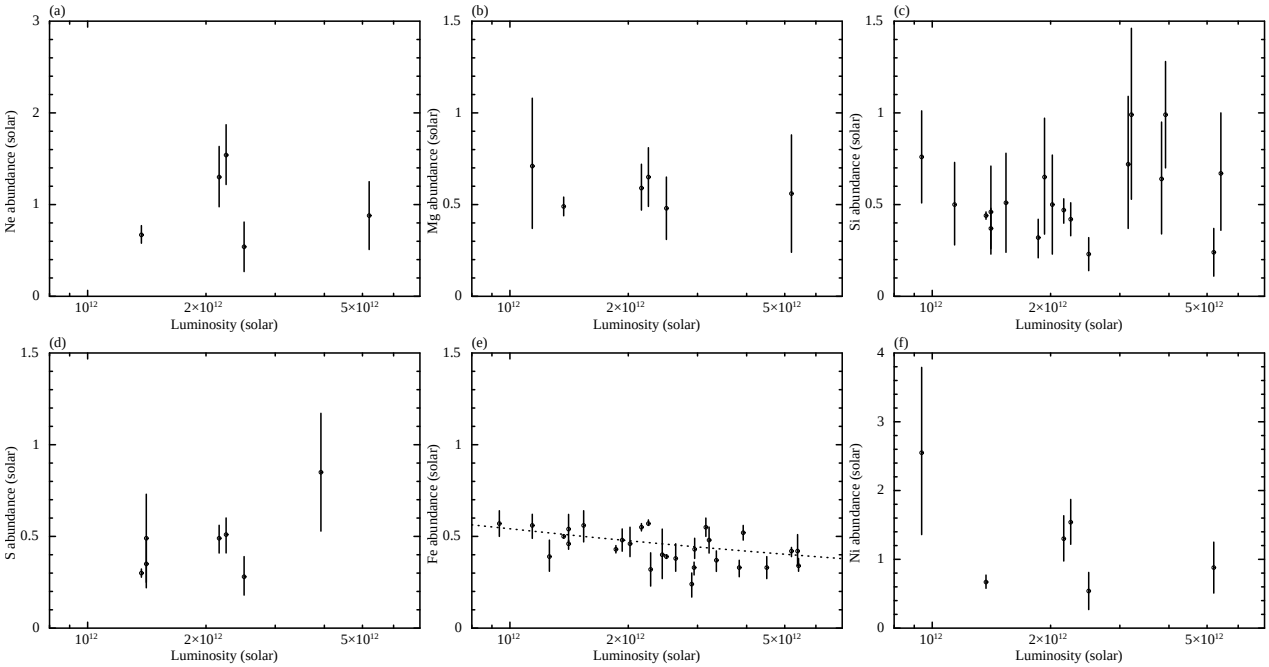

Figure 5.7: Metal abundances plotted as a function of the galaxy luminosity (black circle). The black dashed line show the best-fit power-law model.

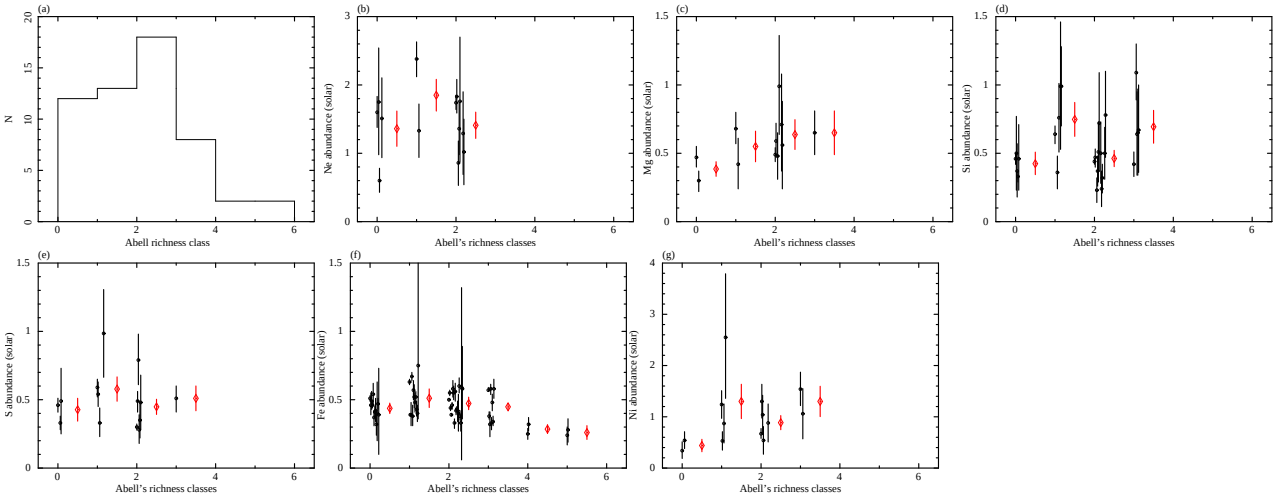

Figure 5.8: (a) Abell's richness classes histogram of the 55 clusters of galaxies in our sample. (b)–(g) Metal abundances versus Abell's richness classes. Red dia denote average metal abundances.

of figure 5.8 shows richness distribution of 55 clusters in our sample, indicating the numbers of rich clusters (richness = 4 and 5) are lower than those of poor clusters. The metal abundances versus Abell's richness classes are plotted in the panel (b)–(g) of figure 5.8, where red diamond denote average values per richness class. According to figure 5.8, panel (b)–(e) and (g) show mostly constant values against the richness class, where we note that the first bin shows lower value in the panel (c) and (g), whereas $Z_{\rm Fe}$ decrease about 50% from 0 to 5 (panel (f)).

B–M type dependence B–M type is also reasonable to trace the age of clusters (subsection 2.2.2). B–M type of clusters are summarized in table B.1. B–M type I is considered to be older than type III

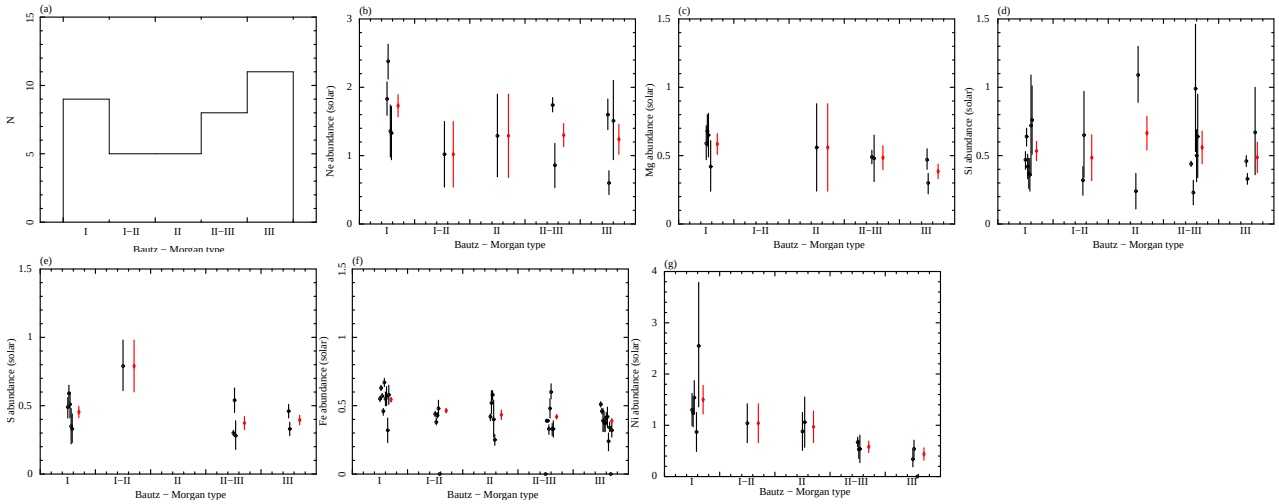

Figure 5.9: (a) B–M type histogram of the 38 clusters of galaxies in our sample. (b)–(g) B–M type versus metal abundances in the ICM. Red dia indicate the average value of the metal abundances.

because type I has cD galaxies in the central region. According to figure 5.9, the metal abundances of iron family elements tend to decrease from type I to type III about $\sim 30\%$ for $Z_{\rm Fe}$ and $\sim 70\%$ for $Z_{\rm Ni}$, while that of α elements show constant value around 0.5 $Z_{\rm solar}$ for $Z_{\rm Mg}$, $Z_{\rm Si}$ and $Z_{\rm S}$, 1.3 $Z_{\rm solar}$ for $Z_{\rm Ne}$. This trend indicates that the amount of iron family elements are sensitive to the central cD galaxy, where the amount of α elements shows no significant dependence on B–M type.

5.5 Status Resolved Metal Abundance

In this section we show the metal abundances against the status like a merging/relaxed, cool core/non-cool core, AGN/non-AGN.

Cool core dependence Generally, cool core clusters thought to have a cD galaxy in the central region, and the cD galaxy trigger the increase of $Z_{\rm Fe}$ in the central region (Matsushita et al. 2012; figure 2.5). Cool core status is thought to discuss the affection of central region of the cluster. In our sample, 15 clusters have a cool core and 4 clusters are classified non-cool core cluster (panel (a) of figure 5.10). The cool core status of individual clusters are referred by Hudson et al. (2010) and Frank et al. (2013), and summarized in table B.1. In panel (b) and (c), we show $Z_{\rm Si}$ and $Z_{\rm Fe}$ versus cool core status. We do not discuss about the other elements because of low statistics. Panel (b) of figure 5.10 shows the constant value of the $Z_{\rm Si}$ around 0.5 $Z_{\rm solar}$, where $Z_{\rm Fe}$ shows the percentage difference of 20%. These trend indicate that the central cD galaxy status perhaps affect only iron family elements.

Merging dependence Here we resolve the metal abundances with merging status, merging or non-merging. The merging status of individual clusters are referred by Frank et al. (2013) and summarized in table B.1. Panel (a) of figure 5.11 shows the merging phase distribution of my

Table 5.4: The results of Spearman's test and fitting.

	Metal	r_s^a	p^b	d.o.f.	α^c
Redshift	kT	0.42	1.80×10^{-4}	60	0.74 ± 0.04
	Ne	-0.38	0.14	13	-10.87 ± 2.85
	Mg	0.07	0.83	11	—
	Si	0.46	4.94×10^{-3}	28	1.11 ± 0.88
	S	-0.14	0.59	16	—
	Fe	-0.16	0.22	59	-0.09 ± 0.01
	Ni	0.36	0.13	15	0.21 ± 0.11
Temperature	Ne	-0.34	0.18	13	0.12 ± 0.10
	Mg	0.13	0.65	11	—
	Si	0.29	0.10	28	0.07 ± 0.09
	S	0.32	0.18	16	0.22 ± 0.12
	Fe	-0.29	0.02	59	-0.16 ± 0.02
	Ni	-0.17	0.52	15	—
Total mass	Ne	—	—	1	—
	Mg	—	—	1	—
	Si	0.61	0.02	9	0.74 ± 0.05
	S	—	—	4	—
	Fe	-0.15	0.51	18	—
	Ni	—	—	3	—
Luminosity	Ne	—	—	4	—
	Mg	—	—	4	—
	Si	0.18	0.46	16	—
	S	—	—	5	—
	Fe	-0.50	1.00×10^{-3}	26	-0.18 ± 0.01
	Ni	—	—	4	—

[a] Spearman's rank.
[b] Null correlation probability.
[c] Index of model fitting.

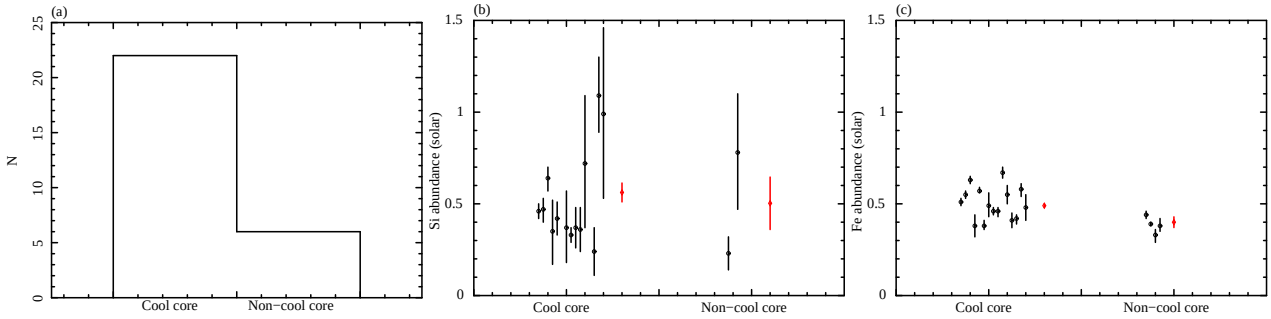

Figure 5.10: (a) Cool core histogram of the 19 clusters of galaxies in our sample. (b), (c) Cool core status varsus metal abundances. Red dia denote the average value.

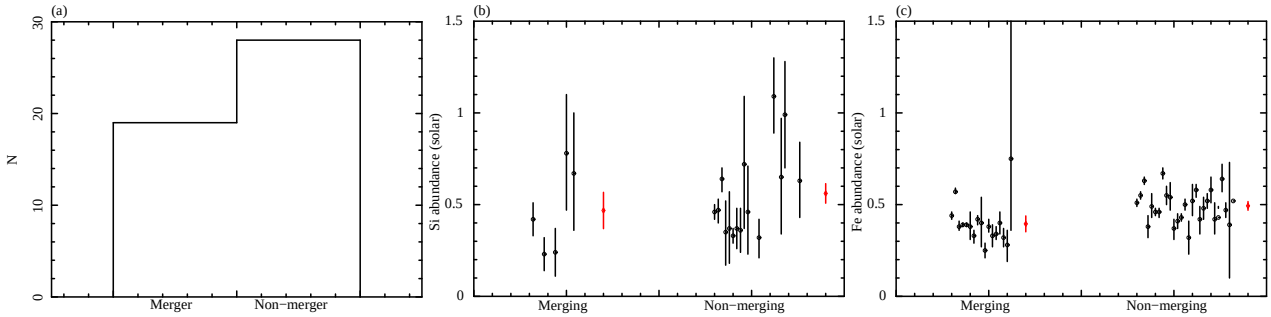

Figure 5.11: (a) Merging status histogram of the 44 clusters of galaxies in our sample. (b), (c) Merging status versus $Z_{\rm Si}$ and $Z_{\rm Fe}$. Red dia indicates average value.

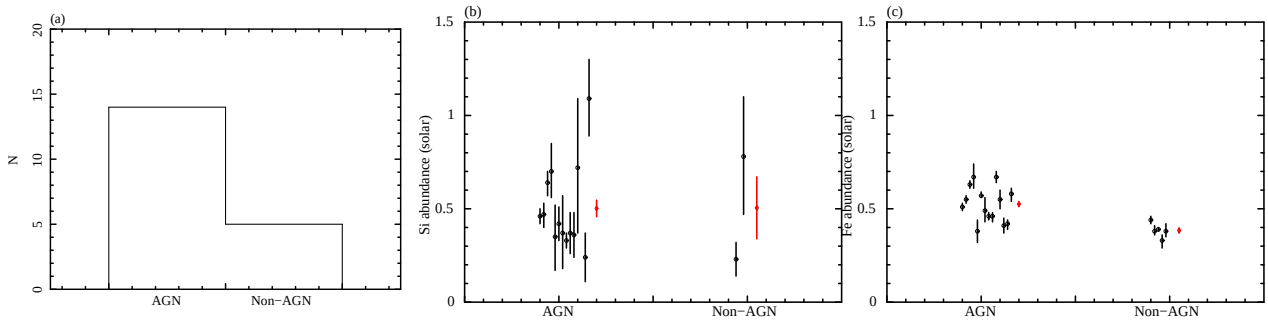

Figure 5.12: (a) AGN status histogram of the 19 clusters of galaxies in our sample. (b), (c) AGN status versus the metal abundances. Red dia indicates the average value.

samples. As shown in figure 5.11(b), $Z_{\rm Si}$ shows consistent value between merging and relaxed clusters within errors, while $Z_{\rm Fe}$ of relaxed clusters shows 20% higher value than that of merging clusters (panel (c)).

AGN dependence Some literature reported that the AGN will trigger the star burst (e.g. Esquej et al. 2012; Zubovas et al. 2013), and as a result the metal abundances are increase than that of non-AGN clusters. The AGN phase of individual clusters are referred by Frank et al. (2013) and summarized in table B.1. Panel (a) of figure 5.12 shows the AGN phase distributions of my samples. Figure 5.12 indicates that $Z_{\rm Si}$ shows no clear dependence on the AGN activity, and show constant value of 0.5 $Z_{\rm solar}$. On the other hand, $Z_{\rm Fe}$ is dropped about 25% at non-AGN clusters comparing with that of AGN clusters. These trend is same as cool core/non-cool core dependence, and indicates that the iron family elements are affected by central status of the clusters.

5.6 Status Resolved Metal Abundance Evolutions

In this section, we show the $Z_{\rm Si}$ and $Z_{\rm Fe}$ against redshift, temperature, total mass, Abell's richness classes with the status like a merging/relaxed, cool core/non-cool core, AGN/non-AGN.

Iron evolutions In figure 5.13, we plotted $Z_{\rm Fe}$ as a function of the several parameters, which thought to trace the age of clusters, with the information of cluster properties such as cool core

presence, dynamical state, and AGN activity. As shown in the distribution of red squares in figure 5.13(d)–(o), non-cool core, merging, non-AGN cluster exhibit rather constant $Z_{\rm Fe}$ around 0.4 $Z_{\rm solar}$ and show signs of older (higher temperature, heavier mass, brighter luminosity) clusters, while cool core, relaxed, and AGN clusters indicate higher abundance but with larger dispersion. The similar results are reported by Frank et al. (2013). They reported the correlation between the average ICM temperature distributions and the cluster properties including cool core presence, dynamical state, and AGN activity, and found that cool core, relaxed, and AGN clusters tend to exhibit lower temperatures. Similar results are reported by other works (e.g. Chen et al. 2007; Burns et al. 2008; Mittal et al. 2009).

We examined Spearman's test to figure 5.13, and the results are summarized in table 5.5. No significant correlation to the size of the clusters are seen in panel (d)–(o). In fact, Fukazawa et al. (1998) reported constant $Z_{\rm Fe}$ based on *ASCA* observation with morphological relaxed and core excluded ($\sim 0.1 h_{50}^{-1} <$ Mpc) analysis. Our results (black circle in figure 5.13(d), (e)) are consistent with their results. Although negative correlation between $Z_{\rm Fe}$ and temperature is reported by Balestra et al. (2007), they did not classify the clusters as argued above, nor exclude the central region. Thus we can conclude that $Z_{\rm Fe}$ exhibit no significant evolution with the age of clusters and is divided two groups with the status of the clusters.

In figure 5.13(a)–(c), all status exhibit rather constant with redshift, except for merging clusters in panel (b). The merging clusters show a moderate increase in time with $r_{\rm s} = -0.37$ and $p = 12\%$ (see table 5.5).

As we seen in the distribution of black or red points in figure 5.13(m)–(o), no clear dependence on the age of clusters are observed. However, since Abell's richness classes value retrieved from NED are not measured in homogeneous sampling with a single detector, we cannot conclude whether this apparent independence implies their less evolution effect or not.

Silicon evolutions In figure 5.14, along with $Z_{\rm Fe}$, we plotted $Z_{\rm Si}$ as a function of the several parameters, which thought to trace the age of clusters, with the information of cluster properties such as cool core presence, dynamical state, and AGN activity. Although, as shown in figure 5.14, status resolved $Z_{\rm Si}$ shows different trend between the two status as a function of temperature, total mass, optical luminosity, and Abell's richness classes, while non-cool core, merging, and non-AGN status show lower value than the other status, except for a function of redshift. The redshift dependence (panel (a)–(c)) show similar trend between two status. The reason what we can not seen the clear dependence to the cluster properties in figure 5.14(m)–(o) is same as described in iron evolutions.

According to the figure 5.14, because the slope of two status is similar, the average value between two status are considered to be consistent as shown in figure 5.10(b), 5.11(b), 5.12(b). The results of Spearman's test are summarized in table 5.5. A significant positive correlation are seen in panels

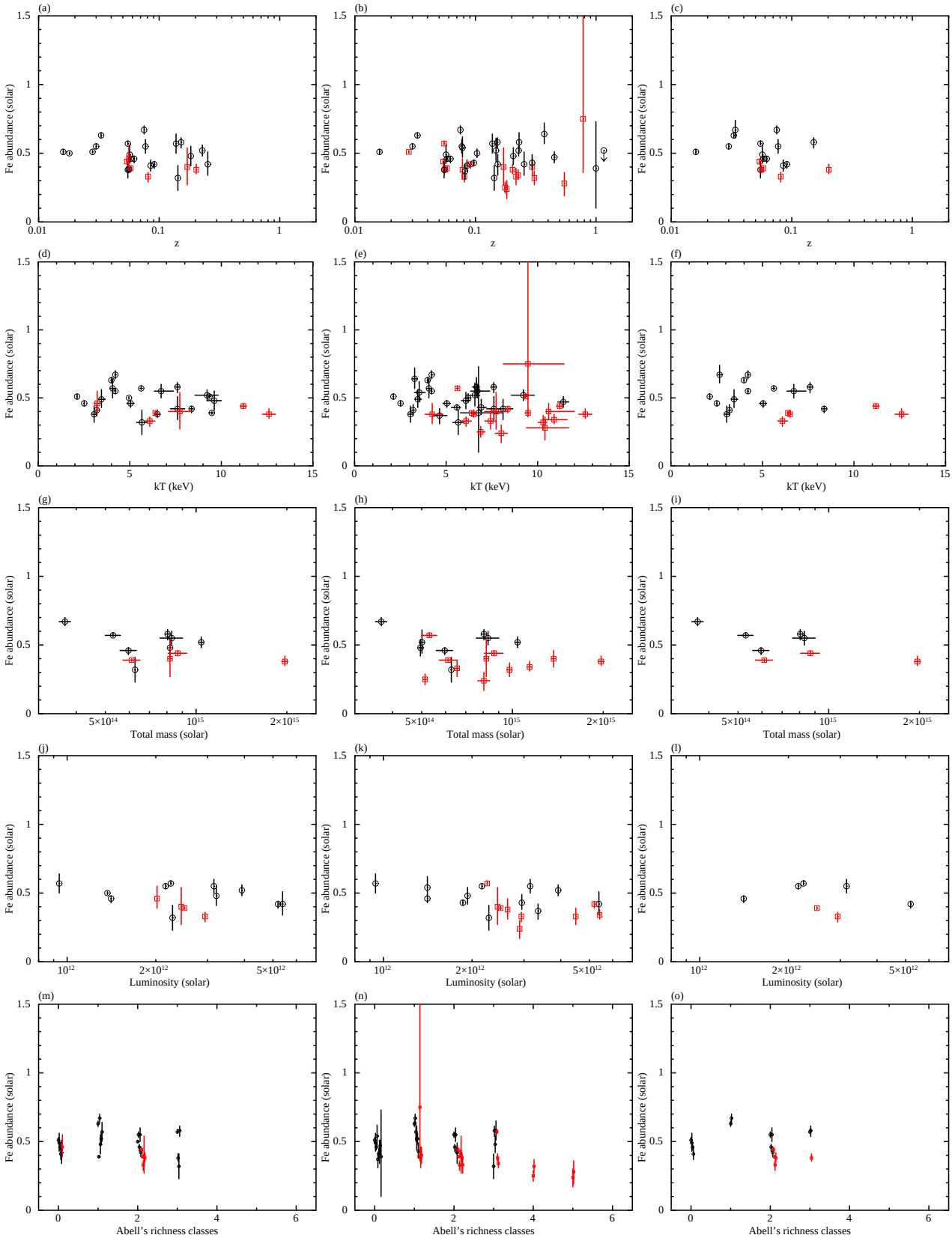

Figure 5.13: (a)–(c) $Z_{\rm Fe}$ versus redshift. (d)–(f) $Z_{\rm Fe}$ versus temperature. (g)–(i) $Z_{\rm Fe}$ versus total mass. (j)–(l) $Z_{\rm Fe}$ versus optical luminosity. (m)–(o) $Z_{\rm Fe}$ versus Abell's richness classes. (a), (d), (g), (j), (m) Black circle and red square denote cool core and non-cool core cluster, respectively. (b), (e), (h), (k), (n) Black circle and red square denote relaxed and merging cluster, respectively. (c), (f), (i), (l), (o) Black circle and red square denote AGN and non-AGN cluster, respectively.

(a), (b), (d), (e) of figure 5.14.

5.7 Number Ratio of Supernovae Ia and cc

5.7.1 Metal abundance ratios

To study the contributions of two types of supernovae (SNe Ia and SNe cc), we derived the relative abundance ratios to Fe by calculating confidence contours between the Fe abundance and another abundance. As an example, the results of MS 1512.4+3647 are shown in figure 5.15 and table 5.6. The relative abundance ratio (90% confidence interval of each) is estimated by the slopes of two lines from the origin (zero abundance point) inscribing the 90% confidence region for each abundance of element. The resultant abundance ratios are consistent with ~ 1 solar ratio within statistical errors (table 5.6). The abundance ratios for the other clusters are summarized in table B.4.

Figure 5.16(a) shows metal to Fe number ratios of obtained from the present *Suzaku* observation in sample. For comparison, the same ratios for nearby clusters observed with *Suzaku* are also plotted. The values are for the radius range of 0.05-0.1 r_{180}, and the clusters are AWM 7 ($z = 0.0172$; Sato et al. 2008), Centaurus cluster ($z = 0.0104$; Sakuma et al. 2011), NGC 5044 ($z = 0.0090$; Komiyama et al. 2009), NGC 1550 ($z = 0.0124$; Sato et al. 2010), HCG 62 ($z = 0.0145$; Tokoi et al. 2008), and NGC 507 ($z = 0.0165$; Sato et al. 2009a). The figure also shows the *XMM-Newton* result by de Plaa et al. (2007), indicating the average values for 22 clusters ($0.0214 \leq z \leq 0.1840$).

Figure 5.16(a) shows that our sample has the metal to Fe number ratios consistent with those of nearby clusters within the statistical and systematic errors. In the same figure, the expected abundance patterns of SNe Ia and cc yields, based on the calculation by Iwamoto et al. (1999) and Nomoto et al. (2006), are shown with the histogram. We assumed the W7 model for SNe Ia, along with the Salpeter initial mass function (IMF) for stellar masses from 10 to 50 $M_{\rm solar}$ with a progenitor metallicity of $Z = 0.02$ for SNe cc. The observed number ratios for Ne, Mg, Si, S, and Ni over Fe all fall between the SN Ia and SN cc . Therefore, both types of the supernova are considered to have enriched the ICM of the clusters shown in figure 5.16(a).

5.7.2 Number ratio of supernovae Ia and cc

If we assume the metals synthesized in clusters have been kept within the cluster system, the ratio of cumulative number of SN cc explosions to that of SN Ia explosions in each cluster can be estimated from the abundance pattern of metals contained in clusters, because the two types of supernova give significantly different metal yields. Most of Ne and Mg are synthesized by SN cc, while Fe and Ni are mostly produced by SN Ia. The abundance pattern was fitted by the sum of the expected abundance patterns of SN Ia and SN cc (figure A.4). We fit only if the abundance ratio of the two metals are derived at least. Free parameters in the fit are two normalizations of the abundance patterns of the SN Ia and SN cc metal yields. In the actual fit, however, free parameters were chosen to be the

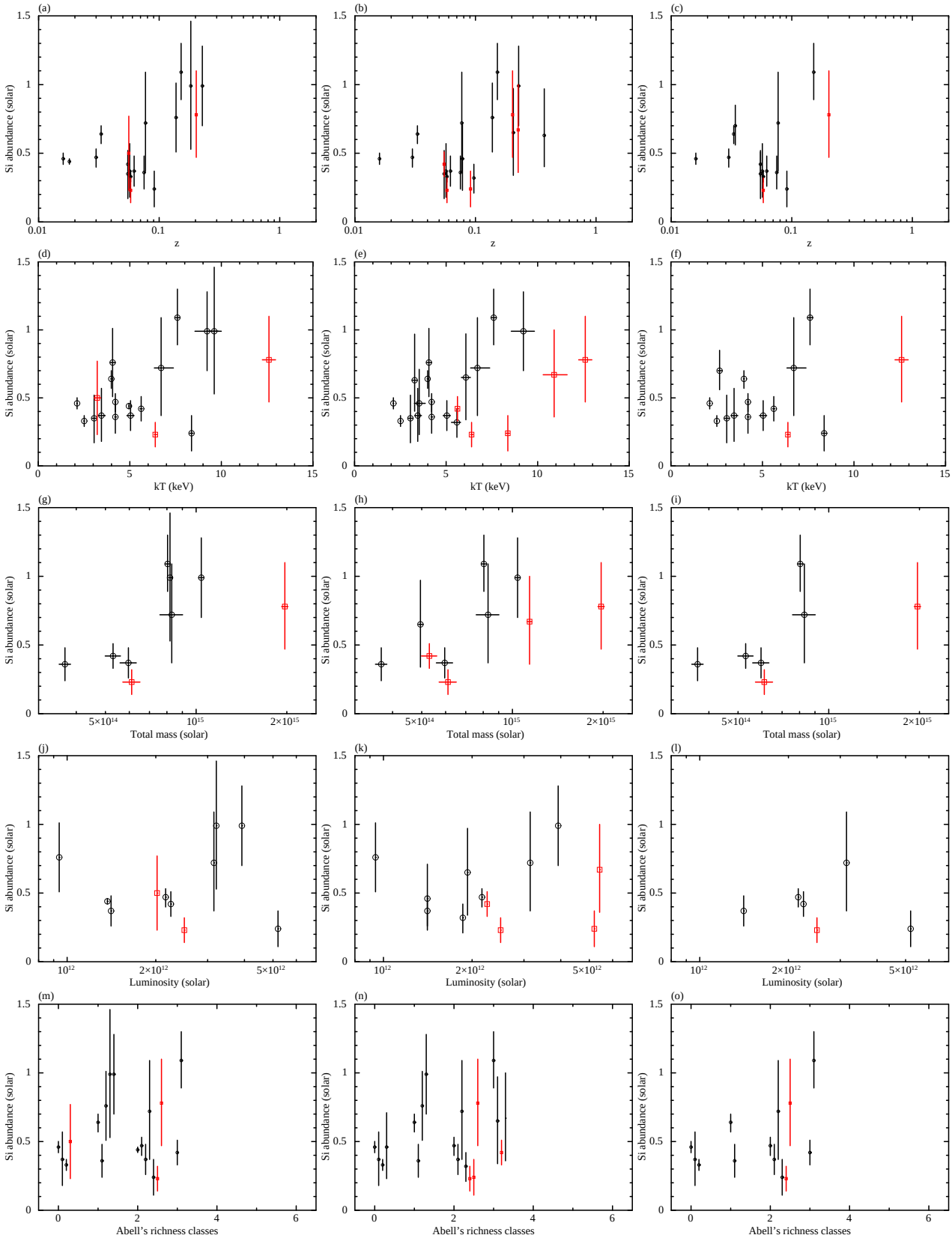

Figure 5.14: (a)–(c) $Z_{\rm Si}$ versus temperature. (d)–(f) $Z_{\rm Si}$ versus temperature. (g)–(i) $Z_{\rm Si}$ versus total mass. (j)–(l) $Z_{\rm Si}$ versus optical luminosity. (m)–(o) $Z_{\rm Si}$ versus Abell's richness classes. (a), (d), (g), (j), (m) Black circle and red square denote cool core and non-cool core cluster, respectively. (b), (e), (h), (k), (n) Black circle and red square denote relaxed and merging cluster, respectively. (c), (f), (i), (l), (o) Black circle and red square denote AGN and non-AGN cluster, respectively.

Table 5.5: The results of Spearman's test.

	Metal	Status	r_s^a	p^b	d.o.f.
Redshift	Si	cool core	0.39	0.14	14
	Si	non-cool core	—	—	1
	Si	relaxed	0.48	6.21×10^{-2}	14
	Si	merging	—	—	3
	Si	AGN	−0.12	0.69	11
	Si	non-AGN	—	—	0
	Fe	cool core	−0.08	0.72	20
	Fe	non-cool core	—	—	4
	Fe	relaxed	−0.11	0.60	25
	Fe	merging	−0.37	0.12	17
	Fe	AGN	−0.16	0.58	12
	Fe	non-AGN	—	—	3
Temperature	Si	cool core	0.43	0.10	14
	Si	non-cool core	—	—	1
	Si	relaxed	0.54	3.00×10^{-2}	14
	Si	merging	—	—	3
	Si	AGN	0.14	0.65	11
	Si	non-AGN	—	—	0
	Fe	cool core	0.05	0.81	20
	Fe	non-cool core	—	—	4
	Fe	relaxed	−0.06	0.75	25
	Fe	merging	0.10	0.68	17
	Fe	AGN	0.19	0.51	12
	Fe	non-AGN	—	—	3
Total mass	Si	cool core	—	—	5
	Si	non-cool core	—	—	0
	Si	relaxed	—	—	4
	Si	merging	—	—	2
	Si	AGN	—	—	3
	Si	non-AGN	—	—	0
	Fe	cool core	—	—	6
	Fe	non-cool core	—	—	2
	Fe	relaxed	—	—	6
	Fe	merging	0.12	0.73	9
	Fe	AGN	—	—	3
	Fe	non-AGN	—	—	1
Luminosity	Si	cool core	—	—	7
	Si	non-cool core	—	—	0
	Si	relaxed	—	—	6
	Si	merging	—	—	2
	Si	AGN	—	—	3
	Si	non-AGN	—	—	0
	Fe	cool core	−0.45	0.16	9
	Fe	non-cool core	—	—	2
	Fe	relaxed	−0.38	0.22	10
	Fe	merging	—	—	7
	Fe	AGN	—	—	3
	Fe	non-AGN	—	—	0

[a] Spearman's rank.
[b] Null correlation probability.
[c] Index of model fitting.

Table 5.6: The metal abundance ratio to Fe in the case of MS 1512.4+3647 (shimoda et al. 2013).

Model	Mg/Fe (solar)	Si/Fe (solar)	S/Fe (solar)	Ni/Fe (solar)
1T	< 2.09	$0.99^{+0.42}_{-0.38}$	$0.66^{+0.45}_{-0.45}$	$3.03^{+2.16}_{-2.06}$
CXB−6%	< 2.08	$0.98^{+0.42}_{-0.39}$	$0.65^{+0.46}_{-0.45}$	$3.11^{+2.23}_{-2.05}$
CXB+6%	< 2.11	$1.00^{+0.42}_{-0.39}$	$0.66^{+0.46}_{-0.45}$	$3.04^{+2.26}_{-2.05}$
NXB±3%	< 2.09	$0.99^{+0.42}_{-0.38}$	$0.66^{+0.45}_{-0.45}$	$3.03^{+2.24}_{-2.06}$
CONTAMI−10%	$1.27^{+1.21}_{-1.08}$	$1.16^{+0.39}_{-0.41}$	$0.80^{+0.49}_{-0.48}$	$3.11^{+2.29}_{-2.12}$
CONTAMI+10%	< 1.82	$0.85^{+0.39}_{-0.36}$	$0.54^{+0.42}_{-0.42}$	$2.99^{+2.15}_{-1.99}$

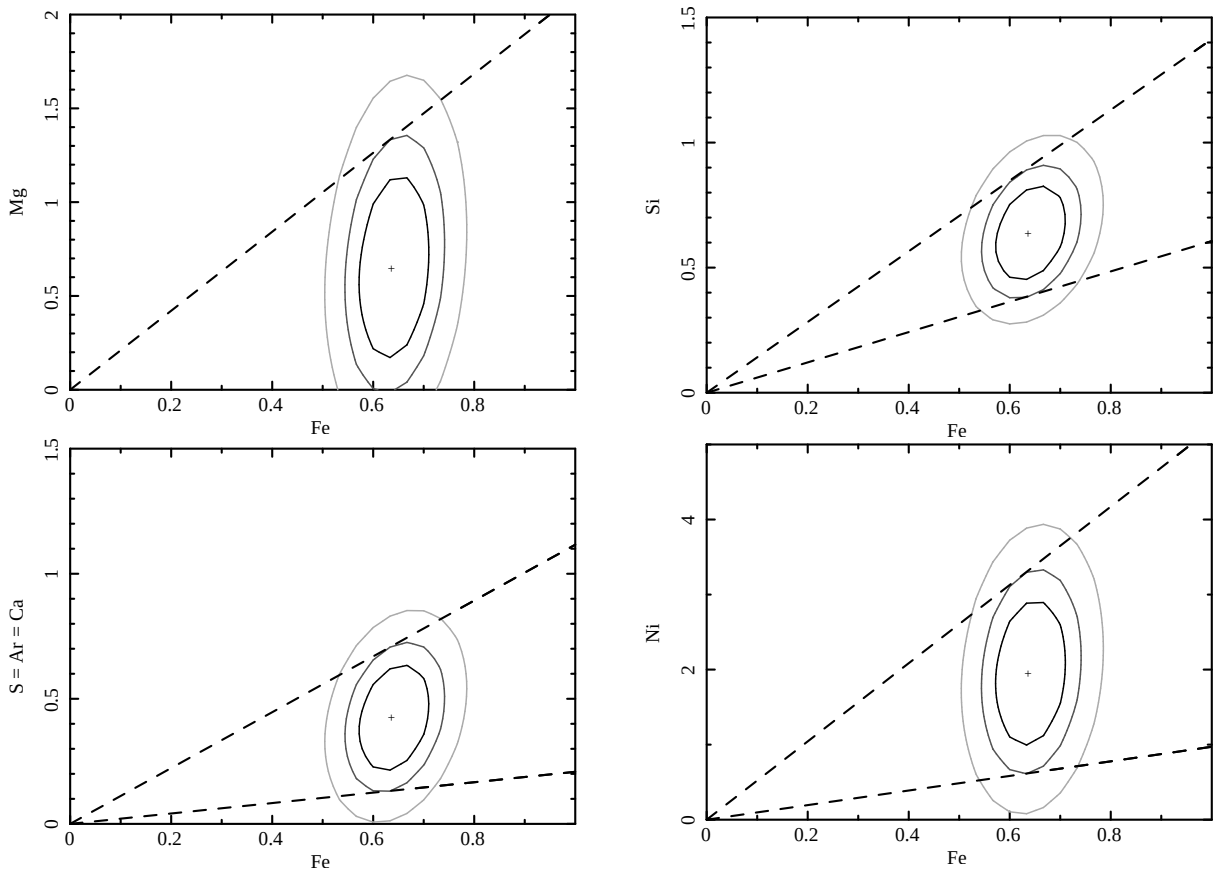

Figure 5.15: Confidence contours between a metal (Mg, Si, S, or Ni) and Fe abundances in the case of MS 1512.4+3647 (shimoda et al. 2013). The black, gray, and light gray contours represent 68%, 90%, and 99% confidence regions, respectively.

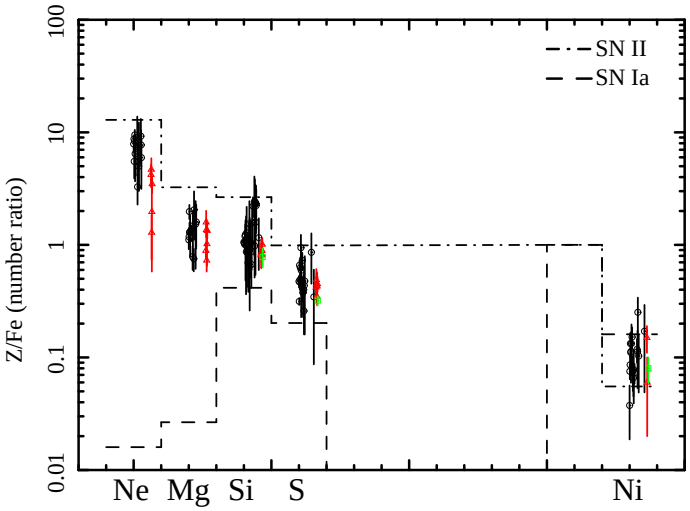

Figure 5.16: The abundance ratios of Ne, Mg, Si, S, and Ni to Fe within 0.3–0.6 r_{200}. The supernova yield models for SN Ia (W7: Iwamoto et al. 1999) and SN cc ($Z = 0.02$ and Salpeter IMF: Nomoto et al. 2006) are plotted in black dashed and dot-dashed lines, respectively.

normalizations of SNe Ia (N_1) and the number ratio of SNe cc to SNe Ia (N_2/N_1), because N_1 could be constrained well with the relatively small error in the Fe abundance. The derived parameters are summarized in table B.4 only if the the value is significant than 1 σ level. Our results range from 3 to 30 with large errorbar. Sato et al. (2007b) reported the supernova ratio, N_2/N_1, for nearby four clusters to be $\sim$ 3.5. de Plaa et al. (2007) also showed that the number ratio of SNe cc to SNe Ia is $\sim$ 3.5, based on *XMM-Newton* observations. The N_2/N_1 ratio of our sample is compared with those of nearby clusters and groups, which are NGC 5044 ($z = 0.009280$, $kT = 1.0$; Komiyama et al. 2009), Hydra Cluster ($z = 0.012600$, $kT = 3.0$ keV; Sato et al. 2007a), NGC 4759 GROUP ($z = 0.014720$, $kT = 1.5$ keV; Tokoi et al. 2008), NGC 0507 ($z = 0.016458$, $kT = 1.5$ keV; Sato et al. 2009a), and WBL 088 ($z = 0.017239$, $kT = 3.5$ keV; Sato et al. 2008) , as a function of redshift (figure 5.17(a)) or temperature (figure 5.17(b)). Spearman's test shows no correlation with $r_s = -0.16$ and null correlation probability of $p = 0.42$ for panel (a), and positive correlation with $r_s = 0.36$ and $p = 0.08$ for panel (b) with 22 d.o.f. We fit simple powerlaw model to figure 5.17(b). The result gives power index of $\alpha = 0.35$ (black dashed line of figure 5.17(b)).

Figure 5.17(a) also shows a curve based on a simple model (dashed green line). For the model, we adopted the star formation history in equation (5) of Strolger et al. (2004), which is based on field galaxy data, as the time evolution of the SN cc frequency, and the gaussian model for the SN Ia time evolution (see figure 14 of Strolger et al. 2004). The present result gives little constraint to the model of the supernova history with large errorbars, but half of our sample shows larger value than the expected value.

According to the bottom panel of figure A.4, most of Ne and Mg and $\sim$ 70% of Si and S are provided by SN cc, while $\sim$ 70% of Fe and most of Ni are provided by SN Ia. The contribution of

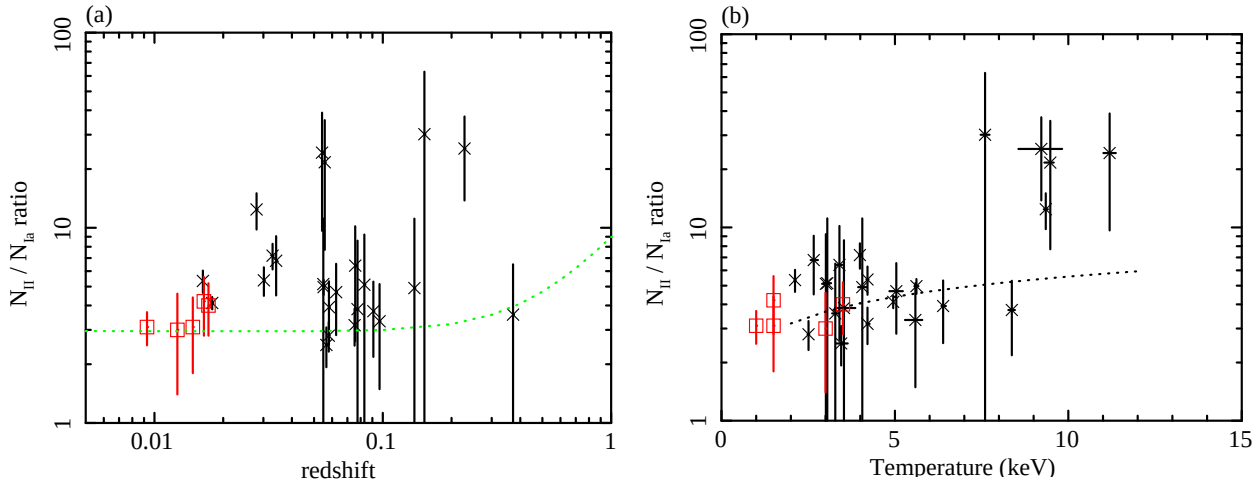

Figure 5.17: (a) Number ratios of SNe cc to SNe Ia plotted against redshift. The dashed green line indicates the expected model, where SNe cc and Ia model are taken from equation (5) and figure 14 of Strolger et al. (2004), respectively. (b) Same as (a) but plotted against temperature. Black dashed line denotes best-fit simple powerlaw model.

SN cc to the Si and S production is slightly larger than the results of de Plaa et al. (2007), while the other elements show consistent values with de Plaa et al. (2007) within errors.

Chapter 6

DISCUSSION

6.1 Summary of the Results

In order to study the metal enrichment histories, we have analyzed the *Suzaku* data of 62 clusters of galaxies to measure average temperature and the metal abundances of Ni, Mg, Si, S, Fe, and Ni of each ICM through X-ray spectral analysis. Together with the total mass and the optical luminosity of the clusters measured by the radio and optical observations, we derived following characteristics of the clusters distributing in the redshift $0.02 < z < 1.16$.

1. $Z_{\rm Fe}$ increases toward lower redshift (in older universe) with a power index of $\alpha = -0.09 \pm 0.01$ (figure 5.4(e)).

2. $Z_{\rm Fe}$ decreases toward larger systems ($\sim$older system) by 30% (figure 5.5(e), figure 5.6(e), figure 5.7(e) and figure 5.8(f)).

3. $Z_{\rm Fe}$ is affected by the central statuses of the cluster and the difference between two status is about factor of 1.3 (figure 5.9(c), figure 5.10(c), figure 5.11(c), and figure 5.12(c)).

4. $Z_{\rm Si}$ decreases toward lower redshift (in older universe) with a power index of $\alpha = 1.11 \pm 0.88$ (figure 5.4(c)).

5. $Z_{\rm Si}$ (in some cases also including $Z_{\rm S}$) increases toward larger ($\sim$older) systems by 50% (figure 5.5(c), figure 5.6(c), figure 5.7(c), and figure 5.8(d)).

6. $Z_{\rm Si}$ shows constant value around $\sim$ 0.5 $Z_{\rm solar}$ with the central statuses (figure 5.9(b), figure 5.10(b), figure 5.11(b), and figure 5.12(b)).

7. Both status resolved $Z_{\rm Si}$ and $Z_{\rm Fe}$ versus age show different trend between relaxed (cool core/AGN) and merging (non-cool core/non-AGN) statuses (figure 5.13 and figure 5.14).

8. The metal abundance number ratios to Fe show consistent values in all samples within errors (figure 5.16(a)).

Table 6.1: Summary of our results.

	Redshift dependence	Size dependence	Status dependence
Fe	increase in time (result 1)	decrease in time (result 2)	Yes (result 3, 7)
Si	decrease in time (result 4)	increase in time (result 5)	Yes (result 6, 7)
$N_{\rm SN\ cc}/N_{\rm SN\ Ia}$	no (result 9)	increase in time (result 9)	—

9. The number ratio of two types of supernovae, $N_{\rm SN\ cc}/N_{\rm SN\ Ia}$, increases from ~ 4 to ~ 20 toward larger systems, while the number ratio shows no correlation with redshift (figure 5.17).

10. Most of Ne and Mg and $\sim 70\%$ of Si and S are provided by SN cc, while most of Fe and Ni are provided by SN Ia (figure A.4).

Above results are interacting with each other. We summarized above results in table 6.1. We will derive consistent explanation of the metal enrichment histories in following sections.

6.2 Iron Evolutions

6.2.1 Redshift evolutions

According to result 1, $Z_{\rm Fe}$ exhibits apparent shallow increase toward lower redshift (older) with power index of $\alpha = -0.09 \pm 0.01$, but we have to note that our sample have a selection bias as we saw in figure 5.3(b). That is, the rate of high temperature samples are increasing toward higher redshift, in other words, the rate of lower $Z_{\rm Fe}$ samples consequently shows apparent increase as shown in figure 5.5(e). To look at the effect of the selection bias on the redshift evolution, we divide our sample to three temperature groups: $kT < 5$ keV (23 clusters), $5 \leq kT < 7$ keV (20 clusters), $7 \leq kT$ keV (19 clusters), and plot in figure 6.1. The Spearman's test to each groups shows no correlation with Spearman's rank of $r_{\rm s} = 0.03$ and null correlation probability of $p = 0.89$ for $kT < 5$ keV, $r_{\rm s} = 0.19$ and $p = 0.43$, $r_{\rm s} = -0.12$ and $p = 0.61$, respectively. Thus we safely reject the redshift evolution of $Z_{\rm Fe}$ and attribute the apparent the redshift evolution of $Z_{\rm Fe}$ to the selection bias of our sample. In Baldi et al. (2011), spatially resolved analysis of 39 clusters of galaxies with *XMM-Newton* reported no significant $Z_{\rm Fe}$ evolution with redshift. Our results support their report, but are inconsistent with Balestra et al. (2007), Maughan et al. (2008), and Anderson et al. (2009) which $Z_{\rm Fe}$ increase toward lower redshift.

As shown in figure 5.13(b), merging status divided $Z_{\rm Fe}$ shows constant value for relaxed clusters, and decrease with redshift for merging clusters. This results suggest that relaxed clusters have already experienced merging and have richer $Z_{\rm Fe}$ than that of merging clusters, while merging clusters have enhanced the starburst and $Z_{\rm Fe}$ decreases with redshift (increase in time). We conclude that the status information (e.g. merging/relaxed) are important to discuss the metal enrichment in the ICM.

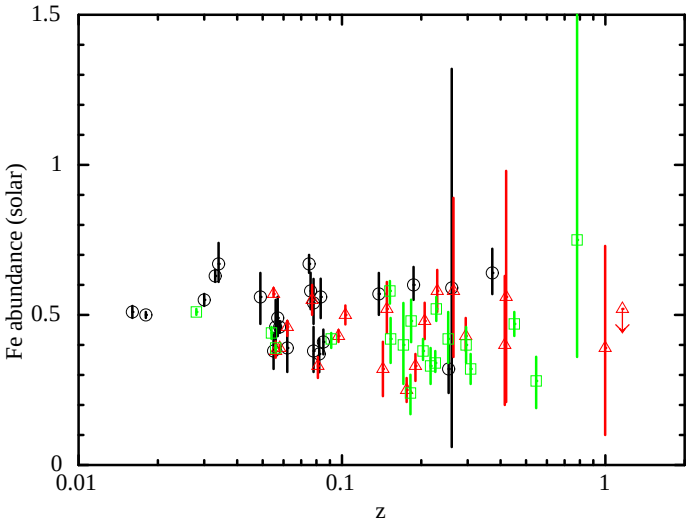

Figure 6.1: Fe abundance plotted versus redshift with three temperature groups. Black circle, red triangle, and green square denote $kT < 5$ keV, $5 \leq kT < 7$ keV, $7 \leq kT$ keV groups, respectively.

The history of the SN Ia rate is more complicated than that of SN cc, because it is a convolution of the lifetime of binary systems and the star formation rate (e.g. Borgani et al. 2008). In general, the SN Ia rate is peaked later in time (at smaller z) and prolonged longer than the SN cc rate history. In fact, a mild decrease of the SN Ia rate in the cluster environment is found from $z \sim 1$ to $z \sim 0$ by a factor of $2 \sim 10$ (Gal-Yam et al. 2002). Our result suggests a low SN Ia rate in $0.02 < z < 1.16$, since the $Z_{\rm Fe}$ is consistent through the our entire sample (figure 5.4(e)) as far as we take in account of selection bias discussed above paragraph. If one assumes the evolution of the SN Ia rate implied from the field galaxy data (for example, model 1N2.3 in solid line in figure 10b of Loewenstein 2006), the number of SN Ia would increase by $\sim 40\%$ from $z = 0.4$ to $z = 0$, namely in about 4 Gy. In this case, the redshift dependence of $Z_{\rm Fe}$ (figure 5.4(e)) requires significantly steep slope than our results. Since *recent* increase of SN Ia rate does not explain our result, we conclude that our result favors models of the SN Ia evolution with steeper gradient and/or more contribution at larger redshifts (for example, model 2H1.05WxSt1 in solid line in figure 11b of Loewenstein 2006). Similar conclusion are addressed in the reported observations of SNe Ia (Mannucci, Della Valle & Panagia 2006; Maoz, Mannucci & Brandt 2012).

6.2.2 Age evolutions

Result 3 indicates that $Z_{\rm Fe}$ concentrates in the central region of the cluster. A number of literatures have reported the central peaked $Z_{\rm Fe}$ profile by spatially resolved spectral analysis so far (e.g. Kawaharada 2006; Sato 2007; Matsushita et al. 2012). They report that $Z_{\rm Fe}$ exhibits significant excess by a factor of 2 at the central region than those in the radius of $\sim 0.4\ r_{200}$. This Fe concentration is explained by member galaxy falling to the center of gravity of each cluster (Gu et al. 2013). They discovered that the member galaxies of clusters are interacting with the ICM

and falling to the central region by ram-pressure with the time scale of ~ 6 Gyr. Then the SN Ia explosion will cause the Fe concentration at the central region (Kawaharada 2006).

The reason of higher $Z_{\rm Fe}$ in the cool core, relaxed, and AGN clusters has been argued as: the starburst activity triggered by cluster merging caused the central cD galaxy for the cool core clusters (e.g. Matsushita et al. 2012), the metal enrichment in ICM through AGN outflow (e.g. Fields et al. 2007), and thus resulted in the relaxed clusters having larger $Z_{\rm Fe}$ (e.g. Elbaz & Cesarsky 2003).

From result 3, we concluded that the trend of decreasing $Z_{\rm Fe}$ with age (result 2) should be attributed to the status of the cluster central region and that there is no significant Fe increase or decrease with the size of systems ($\sim$ age) of the clusters of galaxies.

6.3 Silicon Evolutions

6.3.1 Redshift evolutions

Result 4 indicates that $Z_{\rm Si}$ decrease from distant (in younger universe) to nearby (in older universe) clusters. Considering the selection bias of the sample (section 5.3), we here discuss the redshift evolution. As shown in the diagram of temperature versus redshift relation (figure 5.3(b)), high temperature clusters increase toward higher redshift (in younger universe) with the slope of $\alpha = 0.74 \pm 0.04$, while $Z_{\rm Si}$ versus redshift relation shows the positive slope of $\alpha = 1.11 \pm 0.88$. Since the slopes are consistent within their statistical errors, we conclude that the redshift evolution of $Z_{\rm Si}$ is explained by the selection bias of our sample solely.

The SN cc explosion rates is correlated with the star formation history (SFH), IMF, and the lifetime function of stars (e.g. Borgani et al. 2008). Since massive stars above ~ 8 $M_{\rm solar}$ cause a core collapse with a short lifetime, the history of SN cc should follow the curve of SFH, which is relatively flat at $z > 2$, peaked at $1 < z < 2$, and then decreases by about one order of magnitude toward $z \sim 0$ (e.g. Strolger et al. 2004). For example, in the SFH models (M1 and M2) in Strolger et al. (2004), the number of star formation per unit volume at $0 < z < 0.4$ is only $\sim 10\%$ of the integrated value in $0 < z < 6$. This suggests that the number of SN cc would be lower than the nearby cluster values by about $\sim 10\%$ at $z = 0.4$. Considering the selection bias with power index of $\alpha = 0.74$, the expected decrease of $Z_{\rm Si}$ by about 10% is within the error (figure 5.4(c)). Then we conclude that our results support Strolger et al. (2004).

6.3.2 Age evolutions

Result 6 indicates that $Z_{\rm Si}$ is not affected by the status of core region (< 100 kpc) of the clusters nor extent to the ICM. Some literatures report the central concentration of $Z_{\rm Si}$ by spatially resolved analysis of nearby clusters of galaxies (e.g. Kawaharada 2006; Komiyama et al. 2009; Sato et al. 2009b). Considering result 7, $Z_{\rm Si}$ is divided two groups by the central status of the clusters. Therefore, it is natural to assume that Si is also considered to be affected by the status of core

region.

Result 5 shows that $Z_{\rm Si}$ is proportional to the age of the cluster. Similar results are reported by the *ASCA* observations (Fukazawa et al. 1998; Baumgartner et al. 2005). Fukazawa et al. (1998) explained this trend assuming higher specific energies of SNe cc products. A larger fraction of SNe cc products escapes from the relative shallower gravitational potential of poorer systems. Additionally, the increase of SN cc rate in larger systems also supports the explanation above.

6.4 Contributions from SNe Ia and SNe cc

Result 8 indicates that the metal abundance ratios to Fe are consistent through the our sample, while the scatter is fairly large, and the ratios requires mixed contributions of two types of supernovae in the ICM where Ne/Fe and Mg/Fe show large contributions from SNe cc. This results means that the metal abundance ratio does not depend on age nor size of clusters.

Result 9 implies two possibilities: one is that the cumulative number of SN cc explosion is proportional to the size of the systems because the number of elliptical galaxies in richer clusters are larger than that of poorer clusters (Dressler 1980) and ellipticals have higher frequencies of SN cc explosion than spirals (e.g. Arimoto & Yoshii 1987); and the other is that or the SN cc products are escape from the shallower gravitational potentials of the poorer systems (Fukazawa et al. 1998). The former is possible to introduce the idea of inverse wind (e.g. Matteucci 1994; Pipino & Matteucci 2004). The inverse wind is explained as follows: in the first stage of starburst in the member galaxies, SN cc is dominant because of their shorter lifetime; the large number of SN cc explosions creates galactic wind to evolve the gas material of the starburst; as a result, starburst is stopped, while SN Ia rarely occurred because of their longer lifetime.

The latter is possible because the recent *Suzaku* observations of clusters of galaxies to the virial radius show non-equilibrium state of the outer region of the ICM (Hoshino et al. 2010; Kawaharada et al. 2010; Akamatsu et al. 2011). In the outer region of the ICM, the metals perhaps escape from the gravitational potentials of the clusters suggesting by Fukazawa et al. (1998), and this effect maybe be prominent in poorer clusters. This explanation is well much with our results 9.

Result 10 shows that the contributions to the each metal production of two types of supernovae are common through the our sample, and does not depend on the size of the clusters.

6.5 Implications for Metal Enrichment History

From the above discussion, we summarize the general pictures of the metal enrichment history of the ICM, in phase 1 to 5. The suggested evolutions of $Z_{\rm Fe}$ and $Z_{\rm Si}$ are illustrated in figure 6.2.

1. In the early epoch of cluster formation ($z \sim 2$), the ICM was enriched by the supernovae explosions. SNe cc was dominant than SNe Ia with the ratio of $N_{\rm cc}/N_{\rm Ia} \sim 3.5$ during the era.

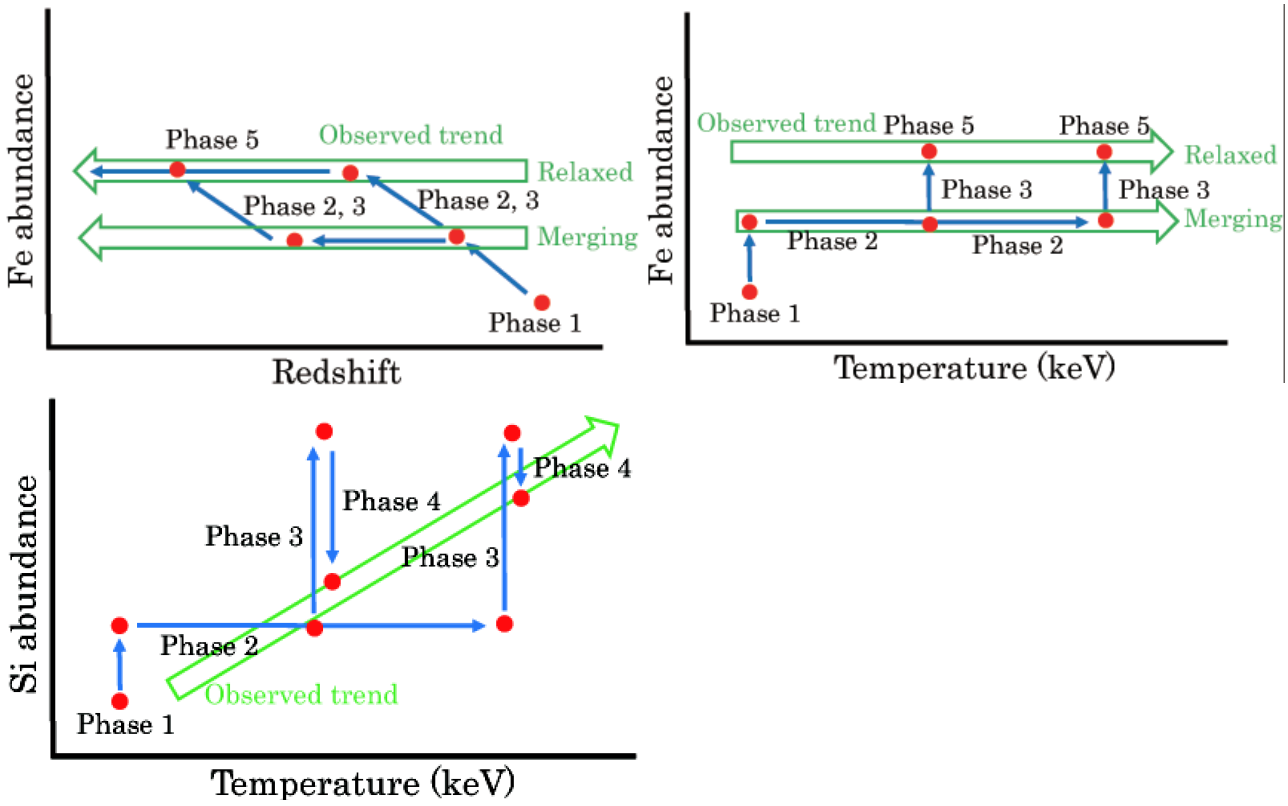

Figure 6.2: Schematic view of metal enrichment history. Redshift distribution is common in Fe and Si. In the pictures, we drew two clusters for the example. For the temperature dependence of $Z_{\rm Si}$, we adopted the Si escape model in phase 4.

2. In the following cluster merging era, the ICM temperature, total mass, and optical luminosity increased.

3. Starburst activity was triggered by the merging in the member galaxies. SN cc is dominant because of short lifetime and then starburst activity ceased shortly by the inverse wind before SN Ia explosion occurred.

4. During the merging, the deviation from equilibrium state of the ICM became prominent, and the metals in the ICM escaped from the gravitational potentials of the cluster, or starburst activity became larger with growth of the cluster, and the portion of SN cc products increased than that of SN Ia products.

5. After the starburst activity, clusters were relaxed, but the average temperature became higher than those before merging because of the larger gravitational potential.

Chapter 7

CONCLUSION

In order to investigate the metal enrichment histories of the ICM, we analyze *Suzaku* data of the 62 clusters of galaxies with *Chandra* and SDSS data.

The metal abundance ratio to Fe exhibit a common shape and contributions of two types supernovae to the metal synthesize are consistent in the range of our sample, while the number ratio of SN cc to SN Ia increases with the age of clusters.

The metal abundance does not show significant evolutions with redshift. On the other hand, the metal abundances plotted with another tracers of age (such as temperature, total mass, and optical luminosities) show different trends between different statuses of clusters such as cool core/non-cool core, merging/relaxed, and AGN/non-AGN. Along the cluster growth, the merging event enhance the starburst activity and the metal abundance of α elements increase, while Fe abundance is almost constant with age. The different trend between Fe and Si supports the escape of SNe cc products from ICM and inverse wind. Thus the difference of the evolution between Fe and Si to $z \sim 1$ based on the X-ray observations shows the different evolution of SNe Ia and SNe cc.

Appendix A

Individual Clusters

A.1 X-Ray Images

The X-ray images of *Suzaku* XIS and *Chandra* ACIS in the 0.5–7.0 keV energy range are shown in figure A.1. For the XIS images, the observed XIS 0, 1, 3 images were added on the sky coordinates after removing calibration-source regions and exposure was corrected, though the NXB and vignetting were not subtracted. The images are smoothed with a Gaussian kernel of $\sigma = 16$ pixel $\simeq 17''$. In the figure A.1, the removed regions of point sources from spectral analysis are indicated by dashed circles. The SRC and the BGD regions are within the solid circle and outside of the dashed circle, respectively.

ACIS image in 0.5—7.0 keV energy range were smoothed with a Gaussian kernel of $\sigma = 4$ pixel $\simeq 2''$. The Suzaku FOV are shown as the square on the image. The point sources detected with `wavdetect` are indicated by black crosses.

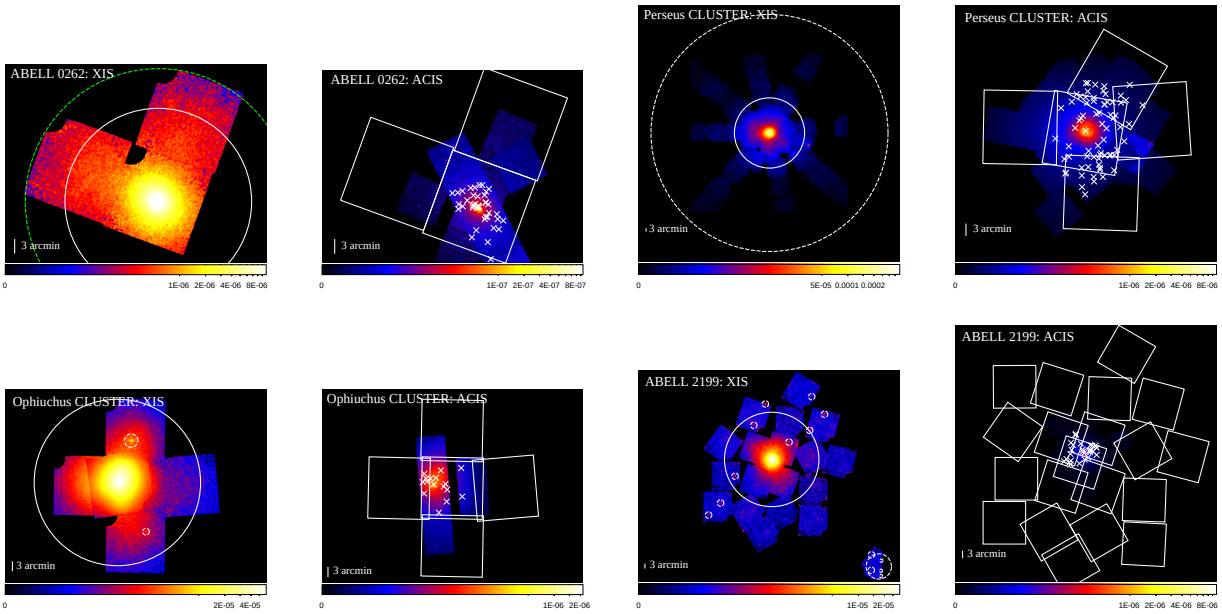

Figure A.1: X-ray images.

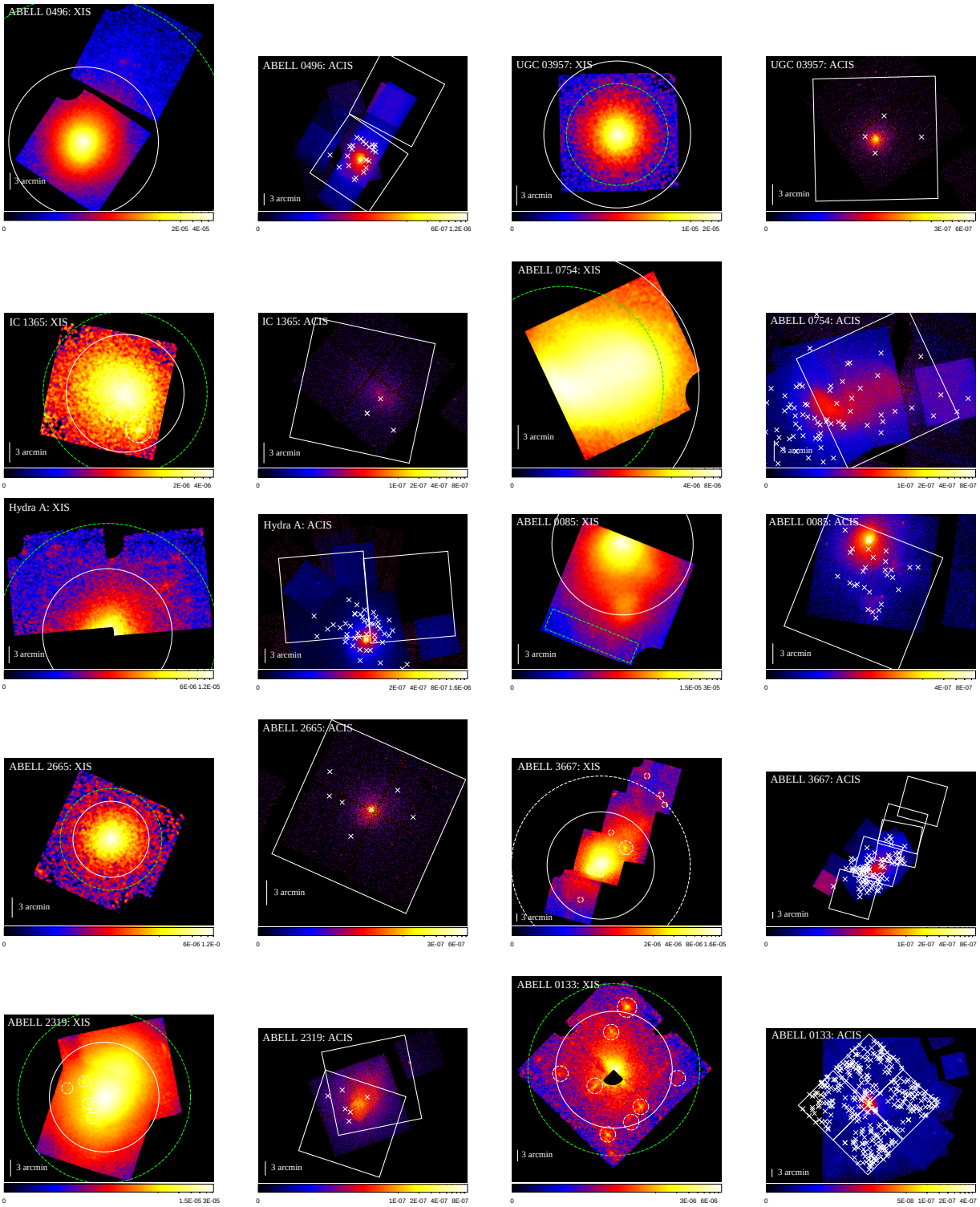

Figure A.1: *Continued.*

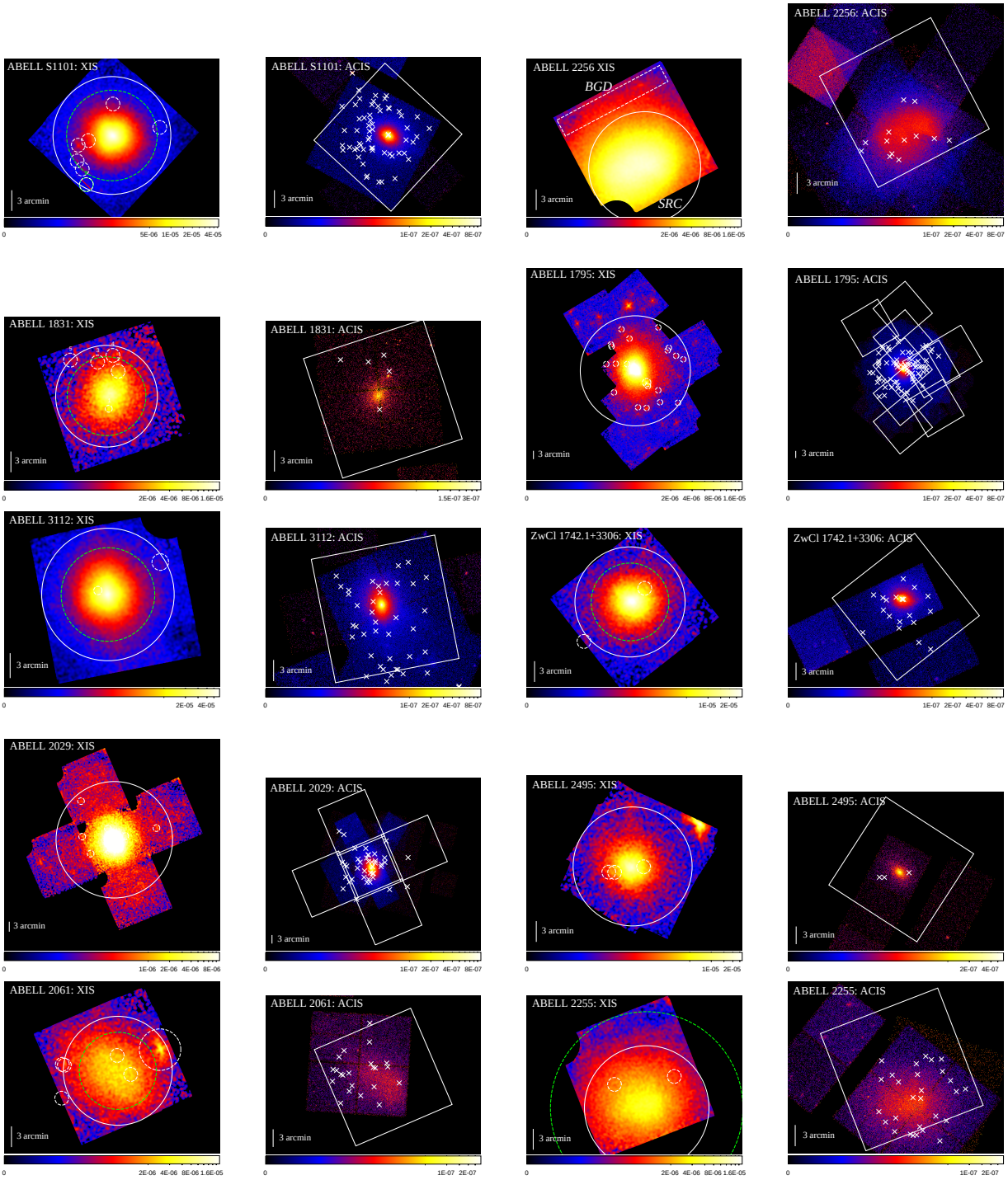

Figure A.1: *Continued.*

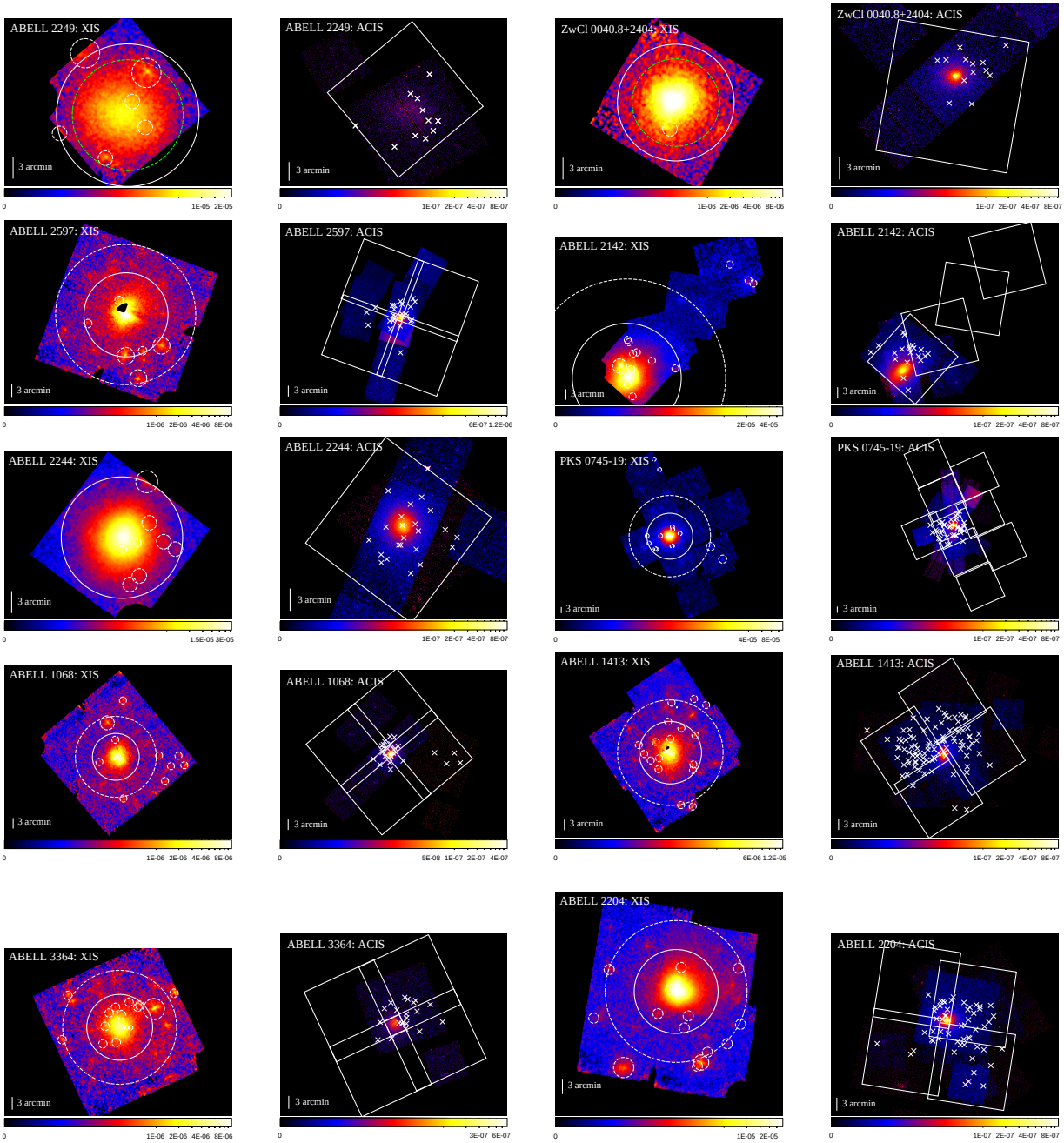

Figure A.1: *Continued.*

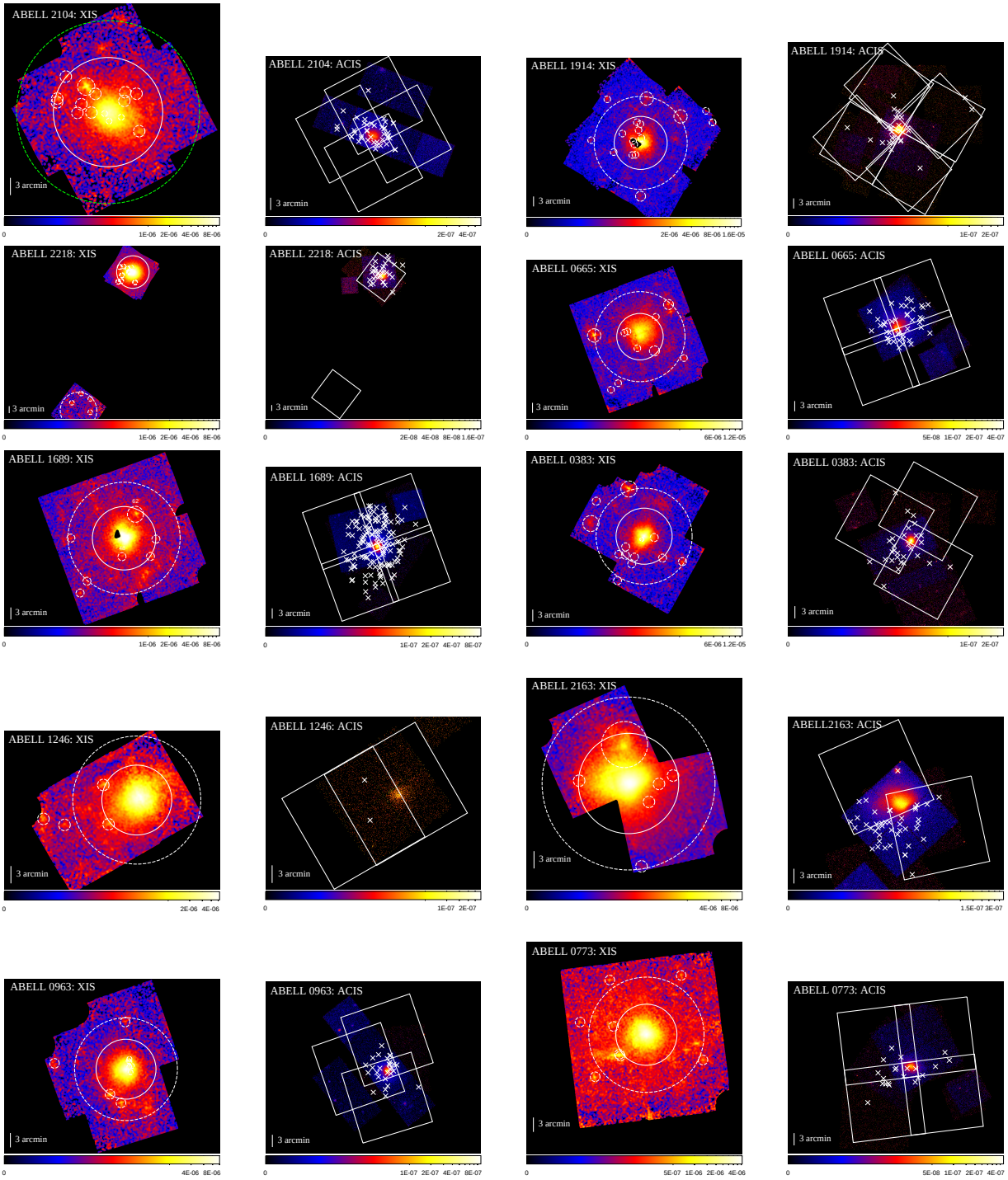

Figure A.1: *Continued.*

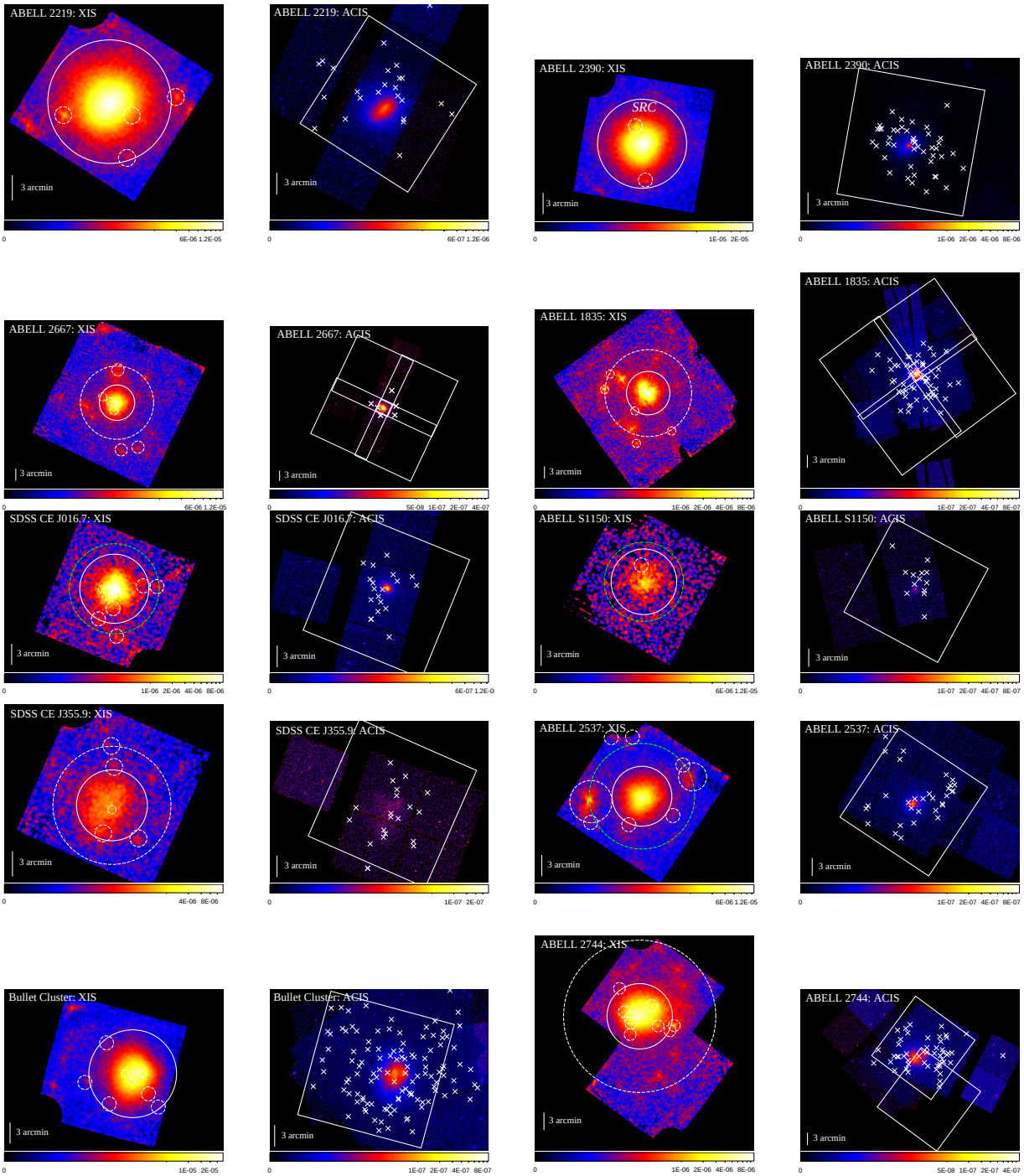

Figure A.1: *Continued.*

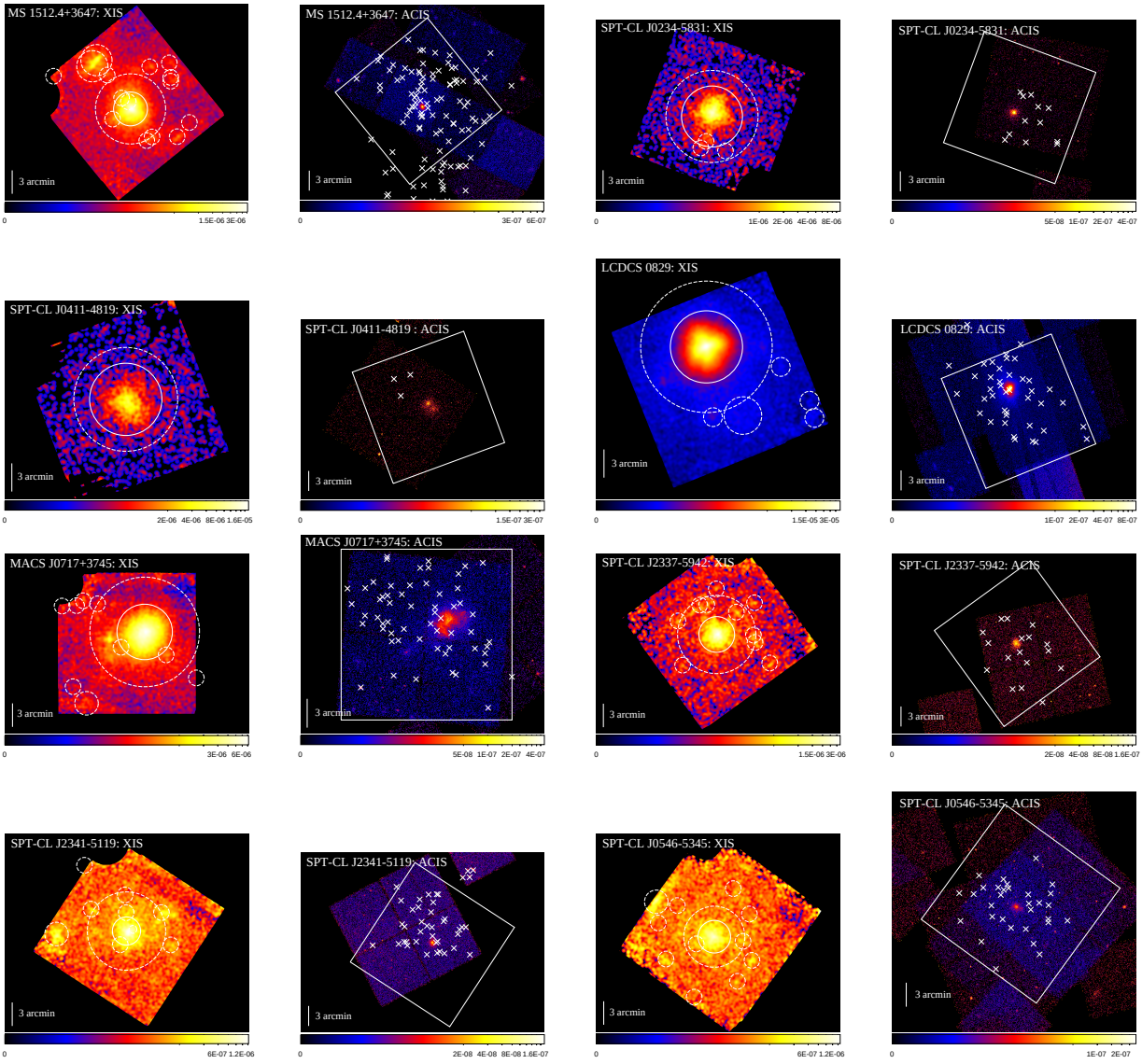

Figure A.1: *Continued.*

A.2 X-Ray Spectra

NXB-subtracted spectra of the SRC region are show in this section. Black and red are XIS-FI (averaged over XIS 0 and XIS 3) and XIS-BI spectra, respectively. Black and red lines are the best-fit model of the XIS-FI and XIS-BI, respectively. For the XIS-FI, model components of the ICM, LHB, MWH, and CXB are shown in blue, magenta, green, and orange, respectively. The lower panel shows the fit residuals in units of σ. XRB spectra are not plotted here for clarity.

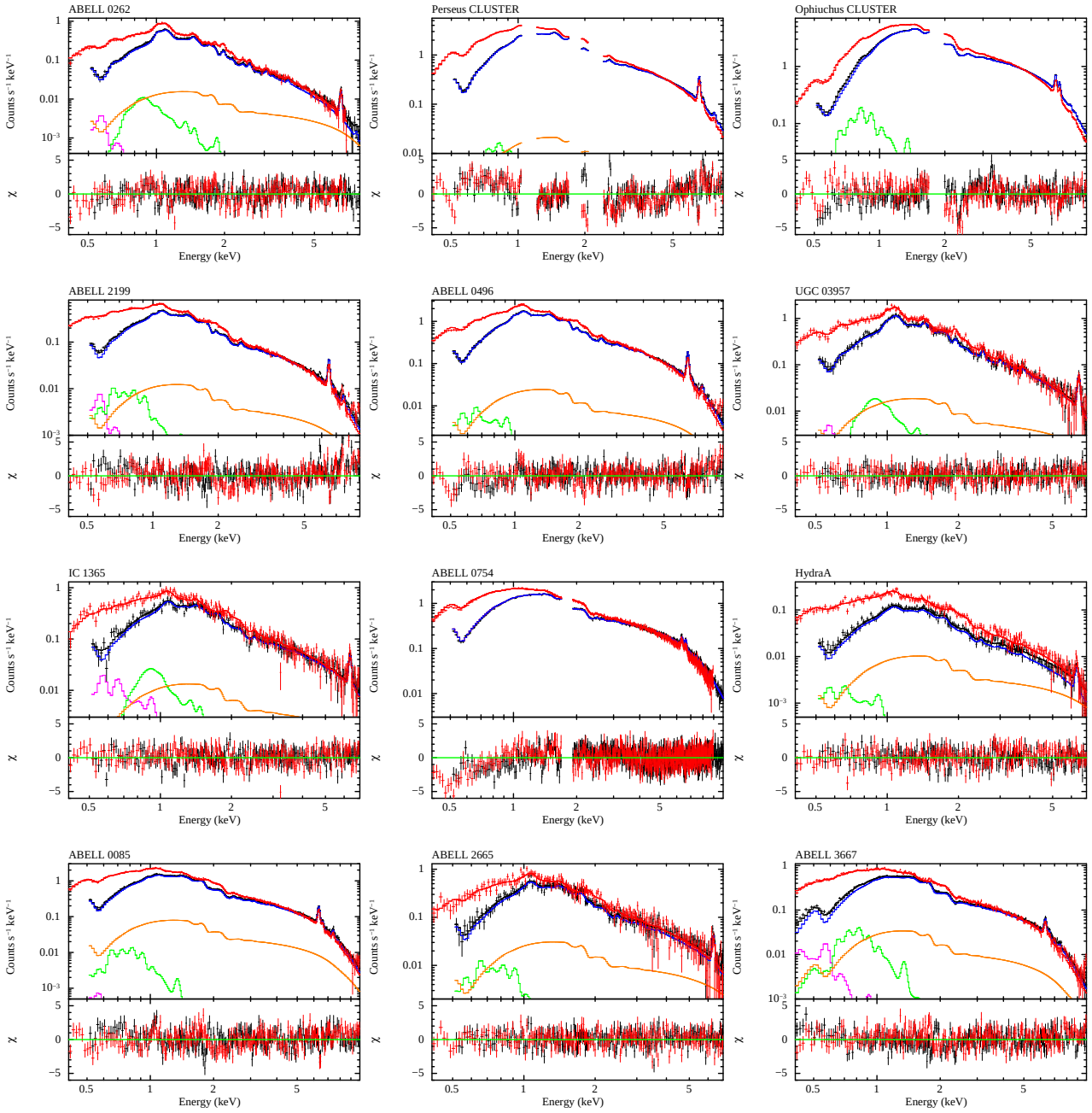

Figure A.2: X-ray spectra.

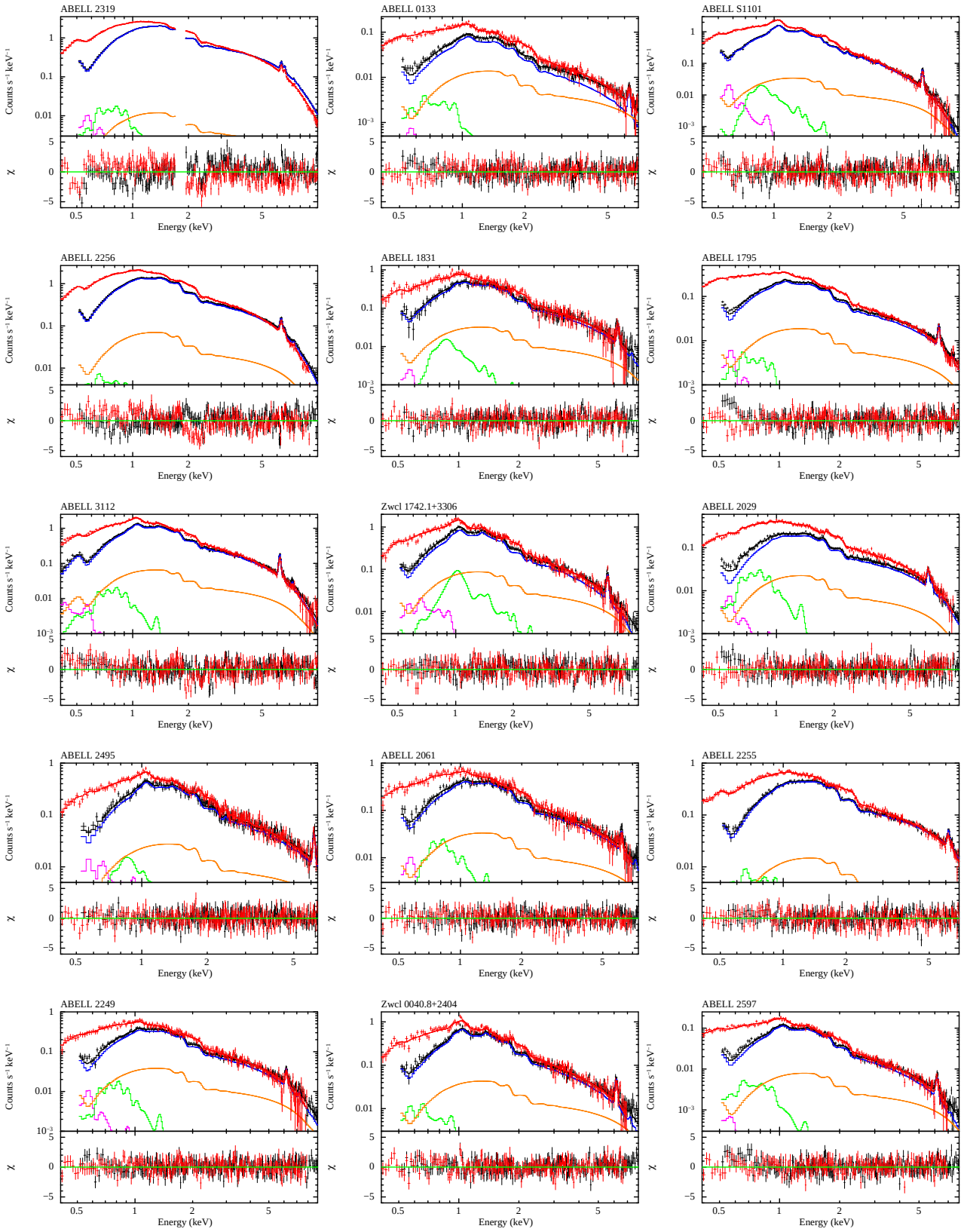

Figure A.2: *Continued.*

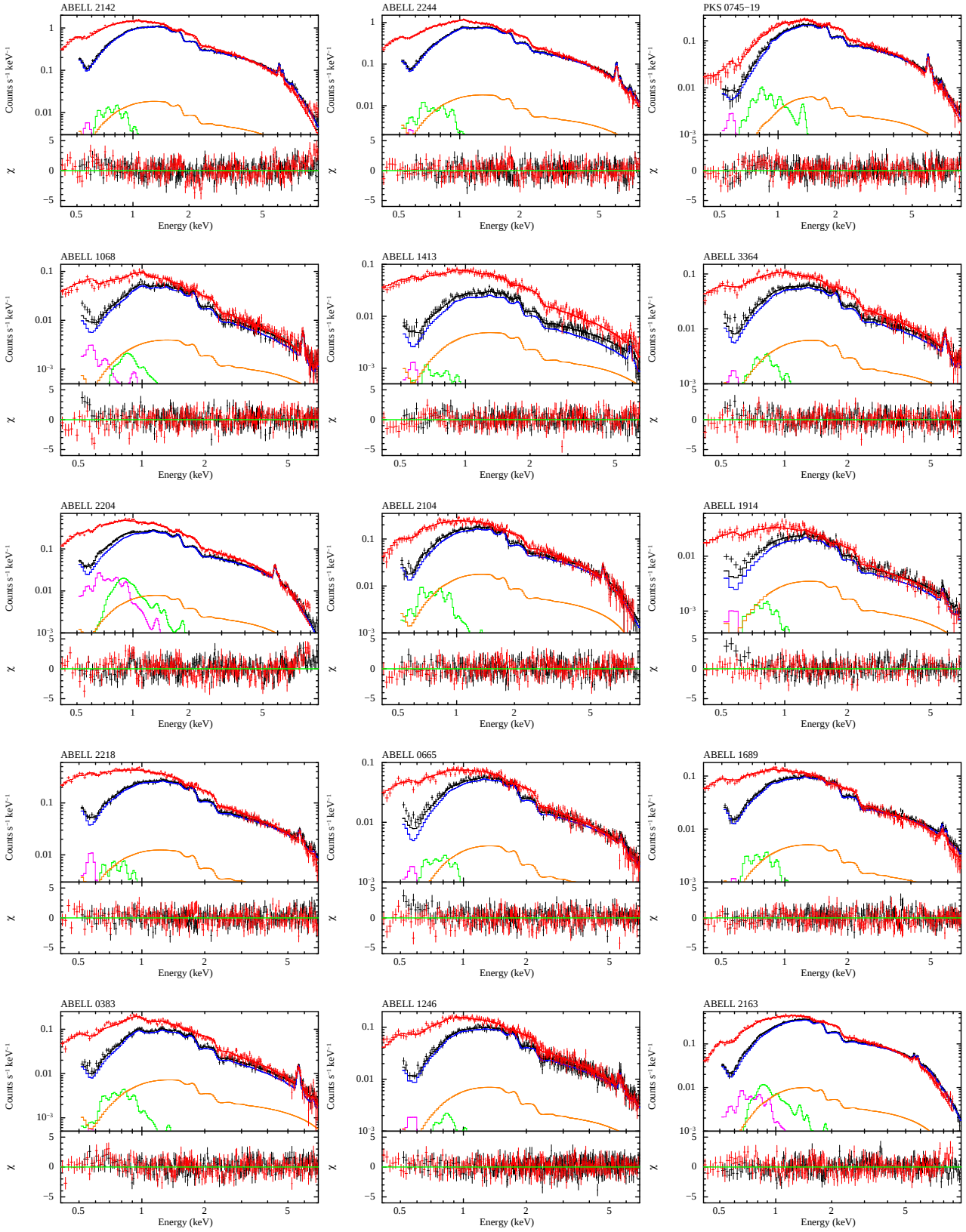

Figure A.2: *Continued.*

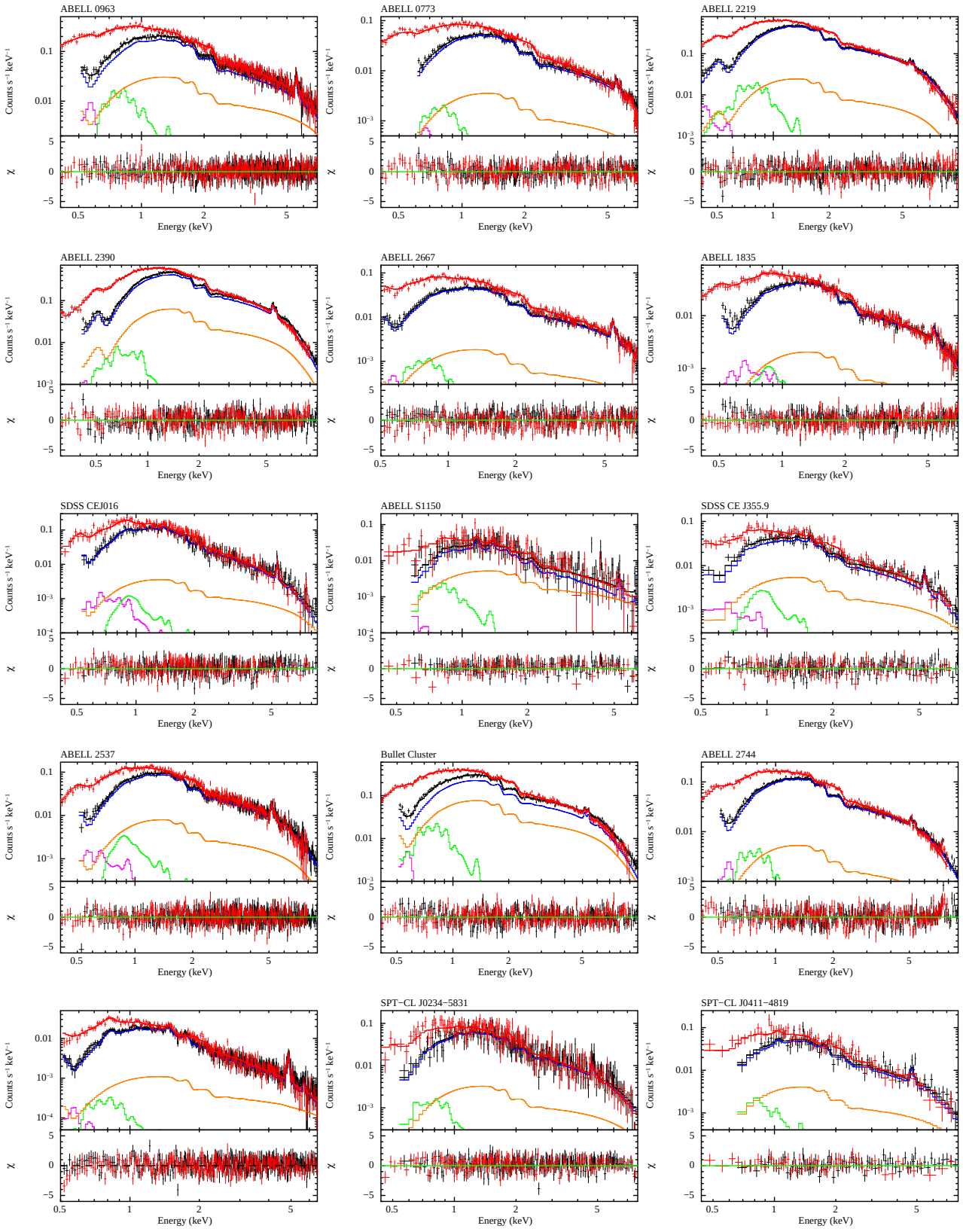

Figure A.2: *Continued.*

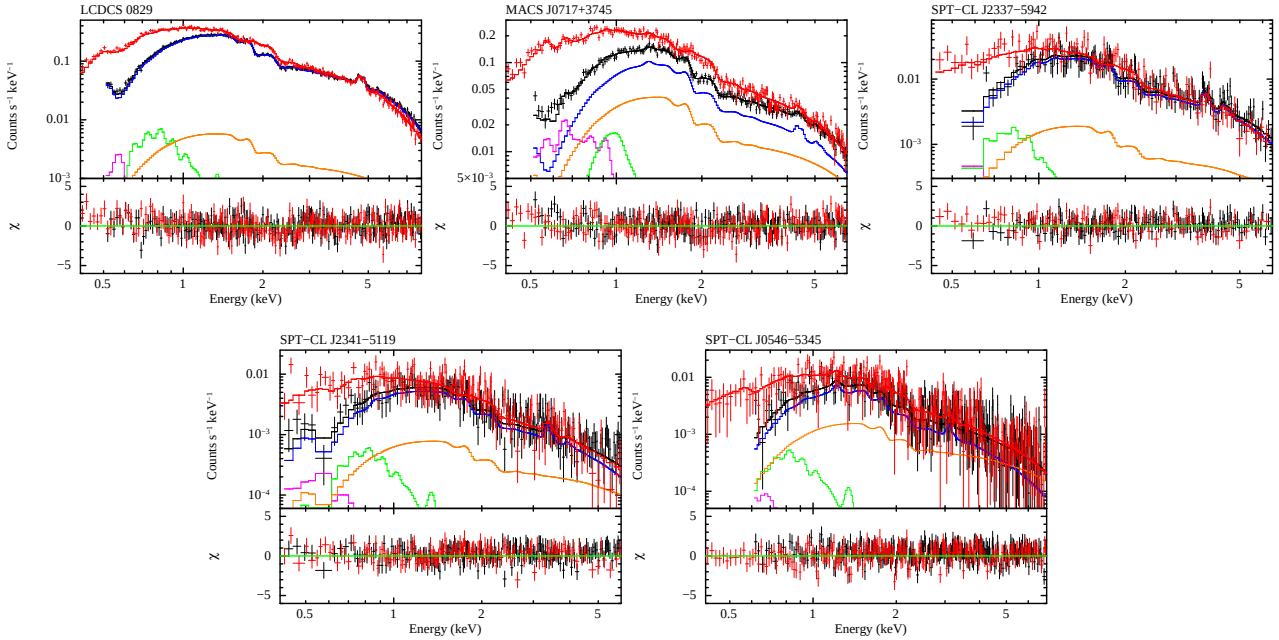

Figure A.2: *Continued.*

A.3 Color-Magnitude Diagram

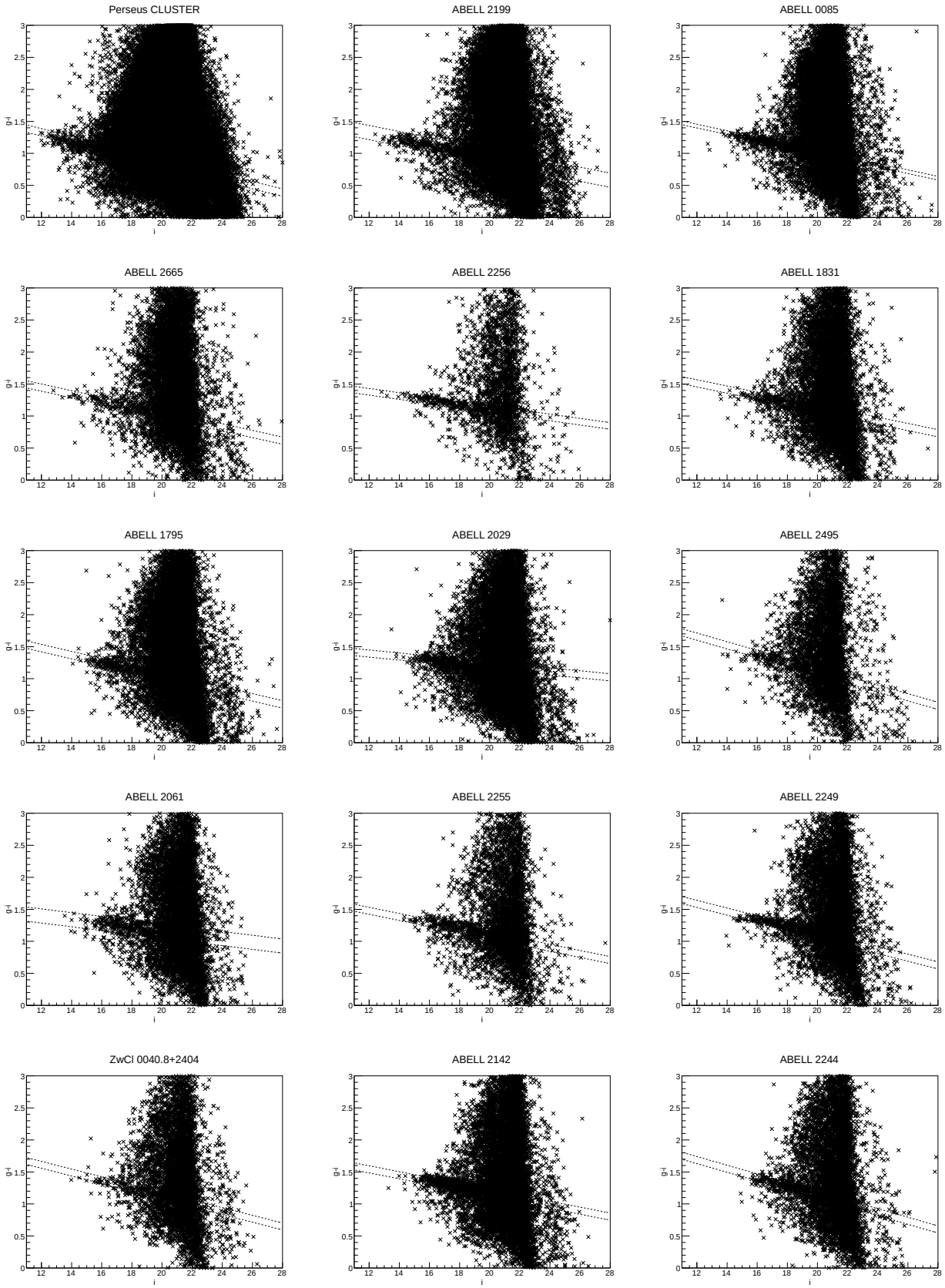

Figure A.3: Color-magnitude diagram.

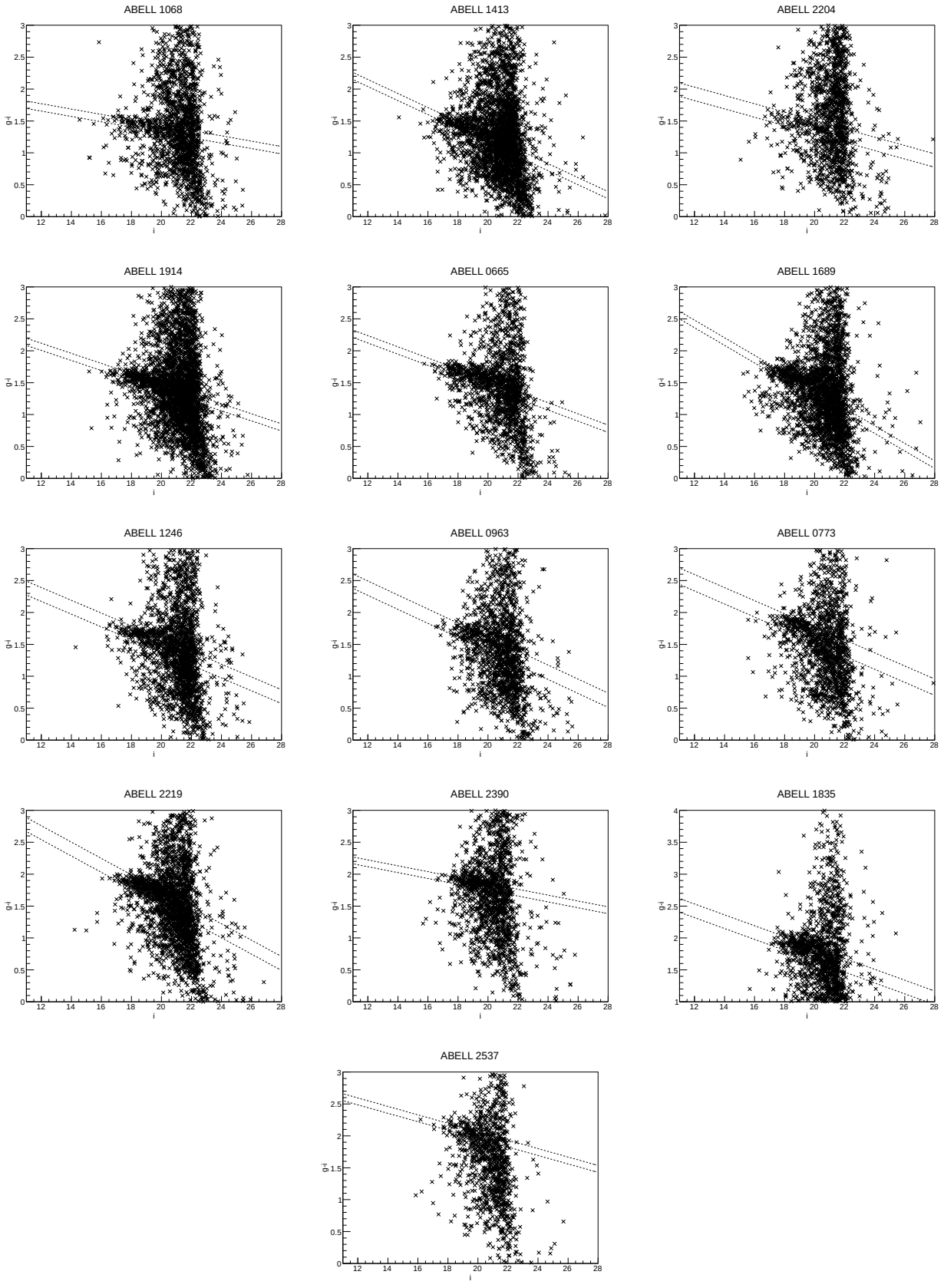

Figure A.3: *Continued.*

A.4 Number Ratio of Supernovae

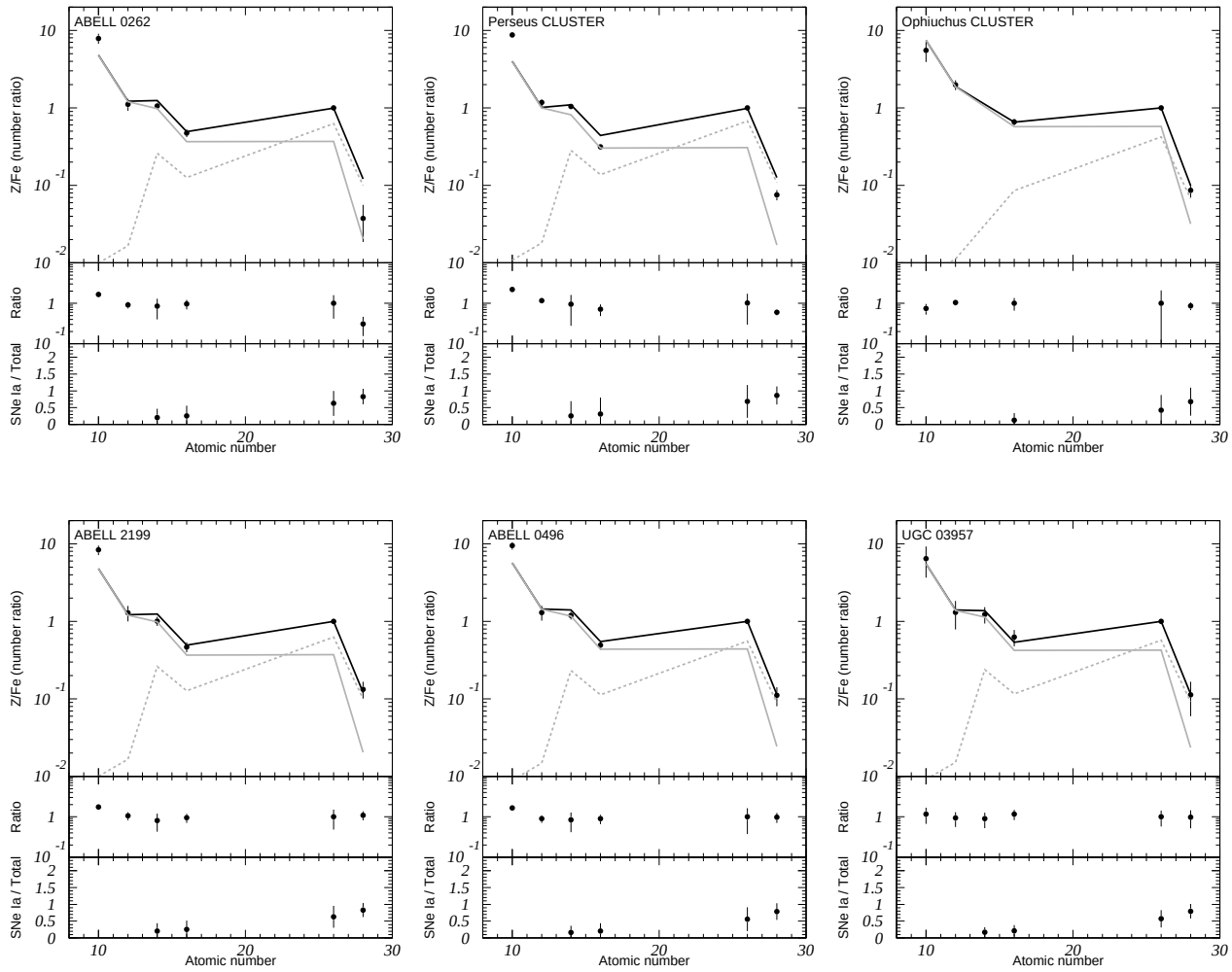

Figure A.4: Top panel shows the abundance ratios within 0.3–0.6r_{200} (black points) fitted by $N_1 + (N_2/N_1)$ (black line). Gray dashed and solid lines correspond to the contributions of SNe Ia and SNe II, respectively. Middle and bottom panels indicate ratios of data to the best fit model, and fractions of the SNe Ia contribution to total metal numbers of individual elements, respectively.

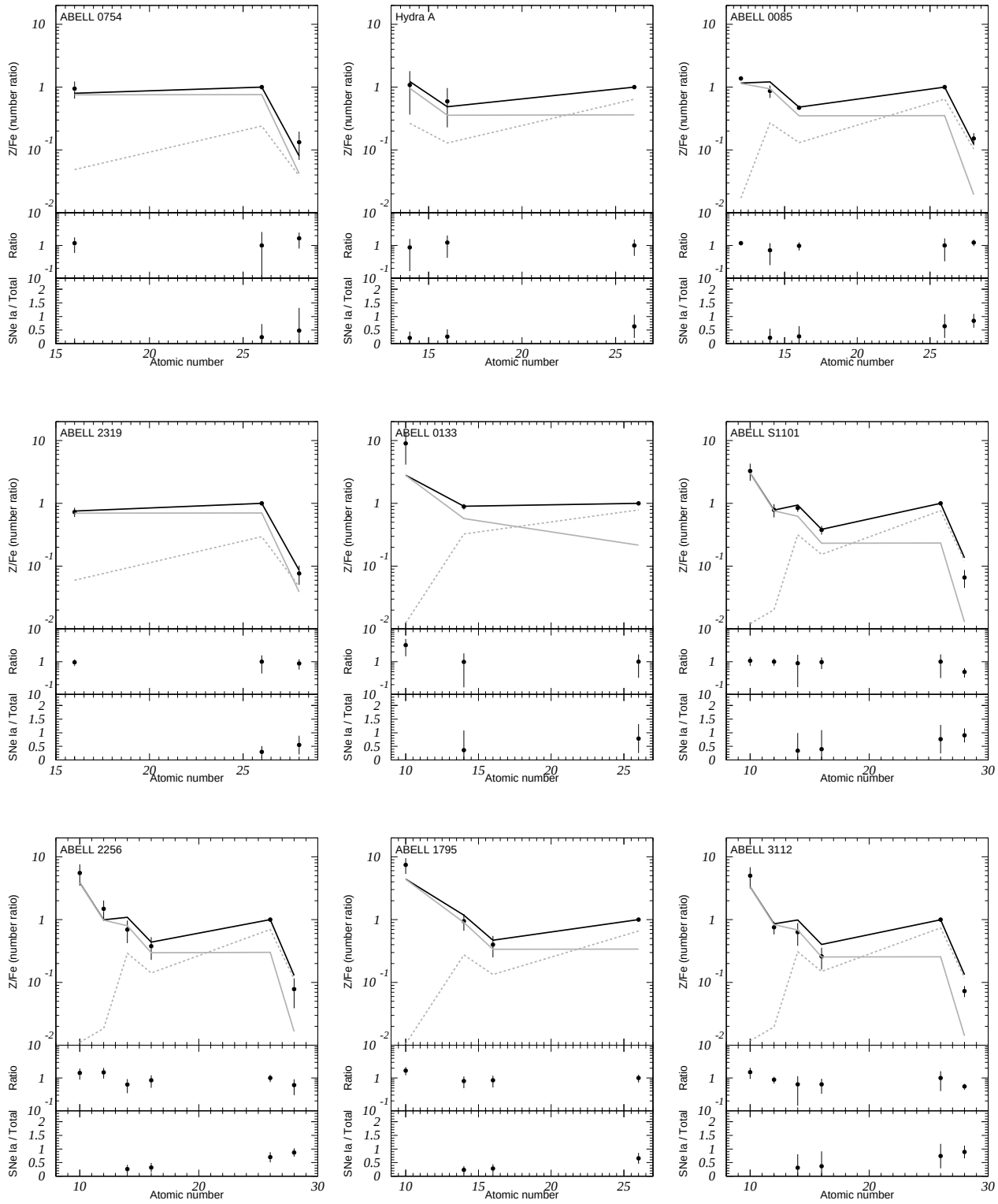

Figure A.4: *Continued.*

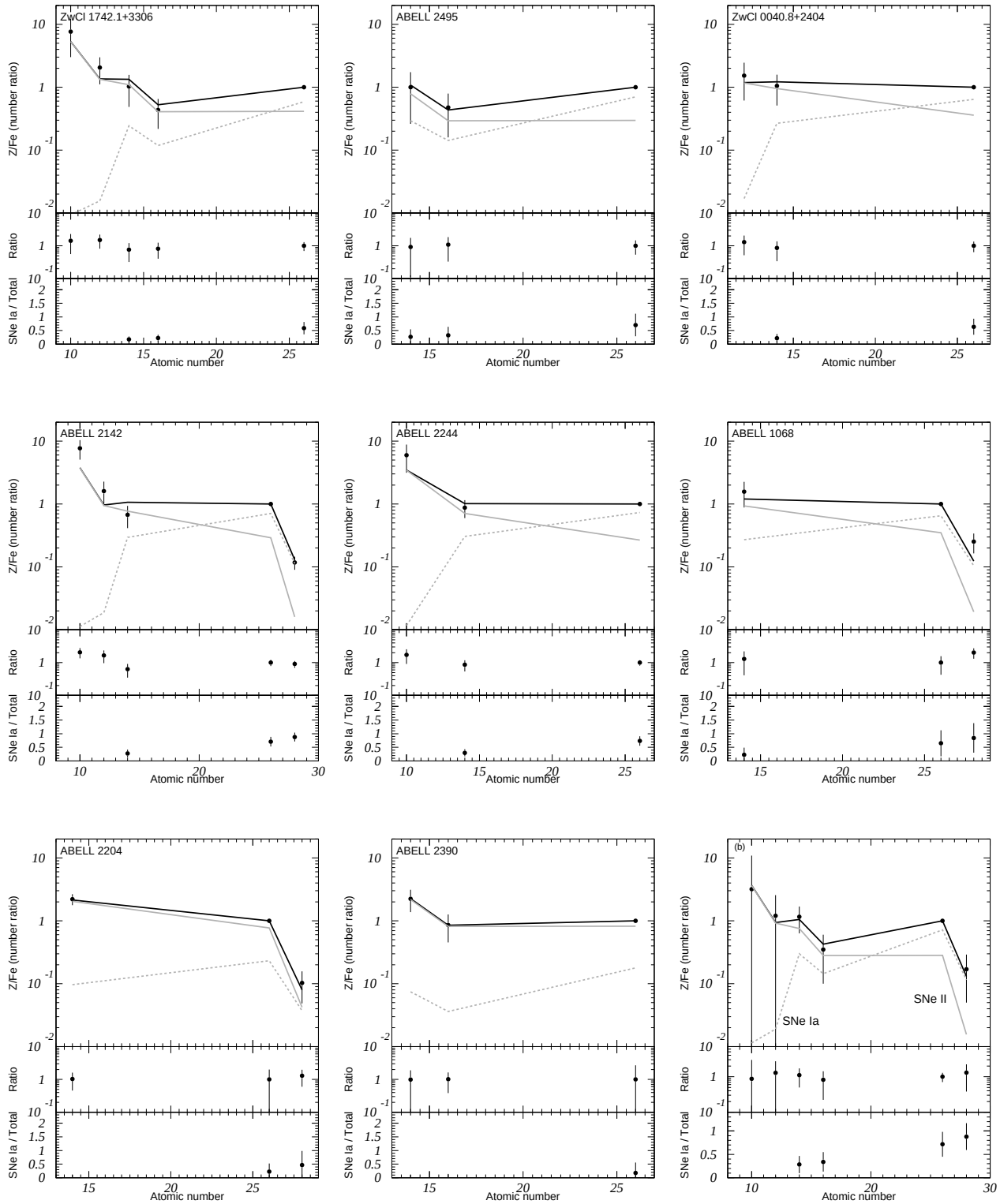

Figure A.4: *Continued.*

Appendix B

Lists of Cluster Parameters

Table B.1: Information of target clusters.

ID	Cluster[a]	z[b]	D_A^c [Mpc]	N_H^d [10^{20} cm^{-2}]	$k\langle T\rangle^e$ [keV]	r_{200}^f [arcmin]	[Mpc]	Richness[g]	B–M type[h]	Merger[i]	CCC[j]	AGN[k]
1	ABELL 0262	0.016	68.5	5.67	2.2	64.1	1.26	0	III	Relaxed	CC	Yes
2	Perseus CLUSTER	0.018	74.0	13.2	6.8	103.7	2.23	2	II—III	—	CC	—
3	Ophiuchus CLUSTER	0.028	114.4	19.30	10.3	82.3	2.73	—	—	Merger	CC	—
4	ABELL 2199	0.030	122.8	0.89	4.1	48.4	1.73	2	I	Relaxed	CC	Yes
5	ABELL 0496	0.033	133.6	3.76	4.1	44.5	1.73	1	I	Relaxed	CC	Yes
6	UGC 03957	0.034	138.3	4.27	3.0	36.4	1.47	—	—	—	—	Yes
7	IC 1365	0.049	191.5	5.75	3.9	29.2	1.67	—	—	—	—	—
8	ABELL 0754	0.054	202.8	4.82	9.5	41.7	2.60	2	I—II	Merger	NCC	No
9	Hydra A	0.055	214.7	4.68	3.0	23.1	1.46	—	—	Relaxed	CC	Yes
10	ABELL 0085	0.055	217.2	2.78	6.9	35.0	2.22	3	I	Merger	CC	Yes
11	ABELL 2665	0.056	217.9	5.82	4.2	27.0	1.73	0	—	—	NCC	—
12	ABELL 3667	0.056	219.9	4.46	6.3	33.1	2.12	3	I—II	Merger	CC	No
13	ABELL 2319	0.056	219.9	8.00	8.8	39.1	2.50	1	II—III	Merger	CC	—
14	ABELL 0133	0.057	221.7	1.59	3.7	25.0	1.63	0	—	Relaxed	CC	Yes
15	ABELL S1101	0.058	223.6	1.14	1.8	17.1	1.14	0	III	Relaxed	CC	Yes
16	ABELL 2256	0.058	228.7	4.24	6.6	32.5	2.17	2	II—III	Merger	NCC	No
17	ABELL 1831	0.062	229.1	1.34	4.2	24.5	1.72	1	III	—	—	—
18	ABELL 1795	0.062	241.5	1.19	7.8	33.0	2.35	2	I	Relaxed	CC	Yes
19	ABELL 3112	0.075	290.9	1.33	5.3	22.8	1.93	1	I	Relaxed	CC	Yes
20	ZwCl 1742.1+3306	0.076	292.5	3.83	4.1	19.9	1.69	2	—	—	—	
21	ABELL 2029	0.077	298.1	3.26	9.1	29.1	2.52	2	I	Relaxed	CC	Yes
22	ABELL 2495	0.078	298.8	4.73	5.0	21.5	1.87	0	—	Relaxed	—	—
23	ABELL 2061	0.078	302.0	1.69	5.6	22.5	1.98	1	III	Merger	—	—
24	ABELL 2255	0.081	309.7	2.49	5.9	22.5	2.03	2	II—III	Merger	NCC	No
25	ABELL 2249	0.082	313.2	2.20	5.6	21.7	1.97	0	III	Relaxed	—	—
26	ZwCl 0040.8+2404	0.083	318.1	3.71	4.3	18.7	1.73	2	—	—	—	—
27	ABELL 2597	0.085	325.7	2.48	3.6	16.6	1.58	0	III	Relaxed	CC	Yes
28	ABELL 2142	0.091	345.2	3.78	9.7	25.8	2.59	2	II	Merger	CC	Yes
29	ABELL 2244	0.097	365.2	1.89	7.1	20.8	2.21	2	I—II	Relaxed	—	—
30	PKS 0745-19	0.103	385.2	41.80	6.5	18.8	2.11	—	—	Relaxed	—	—
31	ABELL 1068	0.138	495.7	1.69	3.9	11.1	1.60	1	I	Relaxed	CC	—
32	ABELL 1413	0.143	511.6	1.83	7.3	14.8	2.20	3	I	Relaxed	CC	—
33	ABELL 3364	0.148	528.4	2.07	6.1	13.0	2.00	1	II	Relaxed	—	—
34	ABELL 2204	0.152	539.9	5.67	7.2	13.8	2.17	3	II	Relaxed	CC	Yes
35	ABELL 2104	0.153	543.4	8.37	9.6	15.8	2.50	2	III	Relaxed	—	—
36	ABELL 1914	0.171	595.0	1.06	8.3	13.3	2.30	2	II	Merger	NCC	—
37	ABELL 2218	0.176	607.4	2.60	6.7	11.7	2.07	4	II	Merger	—	—

Table B.1: *continued.*

ID	Cluster[a]	z^b	D_A^c [Mpc]	N_H^d [10^{20} cm^{-2}]	$k\langle T\rangle^e$ [keV]	r_{200}^f [arcmin]	r_{200}^f [Mpc]	Richness[g]	Morphology[h]	Merger[i]	CCC[j]	AGN[k]
38	ABELL 0665	0.182	625.0	4.31	7.0	11.6	2.10	5	III	Merger	—	—
39	ABELL 1689	0.183	628.5	1.82	9.2	13.2	2.42	1	II—III	—	CC	—
40	ABELL 0383	0.187	639.3	3.48	7.5	11.7	2.18	2	II—III	—	—	—
41	ABELL 1246	0.190	647.7	1.57	5.7	10.1	1.90	3	II—III	—	—	—
42	ABELL 2163	0.203	681.9	10.80	13.3	14.5	2.87	2	—	Merger	NCC	No
43	ABELL 0963	0.206	689.8	1.26	6.8	10.4	2.08	3	I—II	Relaxed	—	—
44	ABELL 0773	0.217	718.3	1.28	8.1	10.6	2.22	2	II—III	Merger	—	—
45	ABELL 2219	0.226	740.1	1.75	11.4	12.2	2.63	3	III	Merger	—	—
46	ABELL 2390	0.228	746.1	6.21	8.8	10.6	2.31	1	—	Relaxed	CC	—
47	ABELL 2667	0.230	751.0	1.73	5.9	8.7	1.90	3	I	Relaxed	—	—
48	ABELL 1835	0.253	807.1	2.04	7.4	8.9	2.09	0	—	Relaxed	CC	—
49	SDSS CE J016.7	0.254	808.3	3.15	2.9	5.5	1.30	0	—	—	—	—
50	ABELL S1150	0.261	825.4	1.13	4.0	6.4	1.53	2	I—II	—	—	—
51	SDSS CE J355.9	0.265	835.4	3.35	5.0	7.0	1.71	2	—	—	—	—
52	ABELL 2537	0.295	901.1	4.63	6.1	7.1	1.86	1	III	Relaxed	—	—
53	Bullet Cluster	0.296	903.3	4.90	13.2	10.4	2.73	1	—	Merger	—	—
54	ABELL 2744	0.308	928.6	1.40	11.2	9.3	2.50	4	III	Merger	—	—
55	MS 1512.4+3647	0.372	1053.0	1.45	2.9	4.0	1.22	—	—	Relaxed	—	—
56	SPT-CL J0234-5831	0.415	1127.2	3.47	5.4	5.0	1.65	0	—	—	—	—
57	SPT-CL J0411-4819	0.420	1135.3	2.53	6.0	5.2	1.73	—	—	—	—	—
58	LCDCS 0829	0.451	1184.0	4.60	10.0	6.4	2.19	0	—	Relaxed	—	—
59	MACS J0717+3745	0.546	1313.7	6.63	11.6	5.9	2.24	5	—	Merger	—	—
60	SPT-CL J2337-5942	0.781	1537.8	1.45	8.9	3.8	1.72	1	—	Merger	—	—
61	SPT-CL J2341-5119	0.998	1657.9	1.21	8.0	3.0	1.44	0	—	Relaxed	—	—
62	SPT-CL J0546-5345	1.160	1711.7	6.79	7.5	2.6	1.27	1	—	Relaxed	—	—

[a] The name of cluster provided by NED.
[b] The cluster redshift provided by NED.
[c] The angular size distance by NED.
[d] Hydrogen column density of galactic absorption by Dickey & Lockman (1990).
[e] Average temperature.
[f] Virial radius.
[g] Abell richness class.
[h] Classification by morphology.
[i] Merging classification.
[j] Cool-core classification by Hudson et al. 2010 and Frank et al. 2013: CC = cool core and NCC = non-cool core.
[k] AGN classification.

Table B.2: Surface brightness profile.

ID	Cluster	$\beta^a_{\rm in}$	$r^b_{\rm core,in}$ [arcmin]	$\beta^a_{\rm out}$	$r^b_{\rm core,out}$ [arcmin]	M^e_{500} [$10^{14} M_{\rm solar}$]
1	ABELL 0262	0.37 ± 0.01	0.127 ± 0.004	—	—	—
2	Perseus CLUSTER	0.58 ± 0.01	1.421 ± 0.004	—	—	—
3	Ophiuchus CLUSTER	0.30 ± 0.01	0.301 ± 0.008	—	—	—
4	ABELL 2199	0.48 ± 0.01	0.09 ± 0.001	—	—	—
5	ABELL 0496	0.49 ± 0.07	0.139 ± 0.016	0.43 ± 0.01	0.454 ± 0.022	—
6	UGC 03957	0.49 ± 0.01	0.325 ± 0.016	—	—	—
7	IC 1365	0.56 ± 0.02	1.983 ± 0.149	—	—	—
8	ABELL 0754	0.43 ± 0.01	1.638 ± 0.033	—	—	8.69 ± 0.63
9	Hydra A	0.48 ± 0.01	0.257 ± 0.004	—	—	—
10	ABELL 0085	0.42 ± 0.01	0.280 ± 0.005	—	—	5.30 ± 0.31
11	ABELL 2665	0.59 ± 0.01	1.147 ± 0.068	—	—	—
12	ABELL 3667	0.66 ± 0.01	3.639 ± 0.084	—	—	—
13	ABELL 2319	0.53 ± 0.01	2.394 ± 0.040	—	—	—
14	ABELL 0133	0.48 ± 0.01	0.251 ± 0.001	—	—	—
15	ABELL S1101	0.64 ± 0.01	0.524 ± 0.004	—	—	—
16	ABELL 2256	0.68 ± 0.05	4.345 ± 0.284	—	—	6.11 ± 0.40
17	ABELL 1831	0.56 ± 0.01	0.989 ± 0.051	—	—	—
18	ABELL 1795	0.53 ± 0.01	0.511 ± 0.007	—	—	5.96 ± 0.37
19	ABELL 3112	0.54 ± 0.01	0.280 ± 0.004	—	—	3.67 ± 0.16
20	ZwCl 1742.1+3306	0.51 ± 0.01	0.347 ± 0.006	—	—	—
21	ABELL 2029	0.59 ± 0.07	0.158 ± 0.026	0.58 ± 0.01	0.713 ± 0.023	8.3 ± 0.72
22	ABELL 2495	0.51 ± 0.01	0.321 ± 0.016	—	—	—
23	ABELL 2061	0.48 ± 0.12	2.801 ± 0.743	—	—	—
24	ABELL 2255	0.82 ± 0.03	4.831 ± 0.169	—	—	—
25	ABELL 2249	0.60 ± 0.06	2.757 ± 0.367	—	—	—
26	ZwCl 0040.8+2404	0.50 ± 0.01	0.185 ± 0.004	—	—	—
27	ABELL 2597	0.59 ± 0.01	0.308 ± 0.001	—	—	—
28	ABELL 2142	0.53 ± 0.01	0.824 ± 0.009	—	—	—
29	ABELL 2244	0.56 ± 0.00	0.694 ± 0.009	—	—	—
30	PKS 0745-19	0.59 ± 0.01	0.353 ± 0.001	—	—	—
31	ABELL 1068	0.98 ± 0.20	0.098 ± 0.018	0.62 ± 0.01	0.354 ± 0.017	—
32	ABELL 1413	0.59 ± 0.01	0.569 ± 0.018	—	—	6.27 ± 0.04
33	ABELL 3364	0.84 ± 0.02	1.447 ± 0.046	—	—	5.01 ± 0.08
34	ABELL 2204	0.52 ± 0.01	0.114 ± 0.003	—	—	8.04 ± 0.15
35	ABELL 2104	0.63 ± 0.02	1.091 ± 0.040	—	—	—
36	ABELL 1914	0.82 ± 0.01	1.061 ± 0.026	—	—	8.19 ± 0.13
37	ABELL 2218	0.72 ± 0.01	1.138 ± 0.039	—	—	5.13 ± 0.08
38	ABELL 0665	0.48 ± 0.01	0.472 ± 0.011	—	—	8.04 ± 0.37
39	ABELL 1689	0.60 ± 0.01	0.405 ± 0.001	—	—	8.19 ± 0.08
40	ABELL 0383	0.84 ± 0.06	0.140 ± 0.014	0.71 ± 0.02	0.535 ± 0.024	—
41	ABELL 1246	0.77 ± 0.05	1.168 ± 0.110	—	—	—
42	ABELL 2163	0.60 ± 0.00	1.090 ± 0.010	—	—	19.68 ± 0.48
43	ABELL 0963	0.63 ± 0.01	0.484 ± 0.030	—	—	4.95 ± 0.07
44	ABELL 0773	0.64 ± 0.01	0.786 ± 0.023	—	—	6.55 ± 0.11
45	ABELL 2219	0.73 ± 0.01	1.209 ± 0.020	—	—	11.44 ± 0.20

Table B.2: *Continued.*

ID	Cluster	$\beta^a_{\rm in}$	$r^b_{\rm core,in}$ [arcmin]	$\beta^a_{\rm out}$	$r^b_{\rm core,out}$ [arcmin]	M^e_{500} [$10^{14} M_{\rm solar}$]
46	ABELL 2390	0.48 ± 0.01	0.193 ± 0.003	—	—	10.35 ± 0.20
47	ABELL 2667	1.35 ± 0.05	0.165 ± 0.008	0.62 ± 0.01	0.390 ± 0.017	—
48	ABELL 1835	0.57 ± 0.01	0.164 ± 0.002	—	—	—
49	SDSS CE J016.7	0.61 ± 0.01	0.125 ± 0.003	—	—	—
50	ABELL S1150	0.70 ± 0.10	0.416 ± 0.089	—	—	—
51	SDSS CE J355.9	1.26 ± 0.93	2.524 ± 1.380	—	—	—
52	ABELL 2537	0.60 ± 0.01	0.384 ± 0.013	—	—	—
53	Bullet Cluster	1.21 ± 0.02	2.124 ± 0.031	—	—	13.73 ± 0.21
54	ABELL 2744	0.89 ± 0.03	1.722 ± 0.066	—	—	9.78 ± 0.21
55	MS 1512.4+3647	0.53 ± 0.01	0.072 ± 0.003	—	—	—
56	SPT-CL J0234-5831	0.59 ± 0.01	0.135 ± 0.011	—	—	—
57	SPT-CL J0411-4819	0.39 ± 0.01	0.074 ± 0.022	—	—	—
58	LCDCS 0829	0.58 ± 0.01	0.102 ± 0.003	—	—	—
59	MACS J0717+3745	0.98 ± 0.06	1.293 ± 0.089	—	—	—
60	SPT-CL J2337-5942	3.10 ± 1.69	1.383 ± 0.467	—	—	—
61	SPT-CL J2341-5119	0.70 ± 0.04	0.228 ± 0.025	—	—	—
62	SPT-CL J0546-5345	0.70 ± 0.06	0.254 ± 0.041	—	—	—

[a] The slope of the surface brightness profile.
[b] The core radius of the surface brightness profile.
[c] The central number density of the ICM.
[d] The ICM mass within 0.3 r_{200}.
[e] The total mass within r_{500} measured with *Plank*.

Table B.3: Fitting results.

ID	Cluster	kT [keV]	Ne [solar]	Mg [solar]	Si [solar]	S=Ar=Ca [solar]	Fe [solar]	Ni [solar]	χ^2/d.o.f
1	ABELL 0262	$2.12^{+0.02}_{-0.02}$	$1.60^{+0.23}_{-0.22}$	$0.47^{+0.08}_{-0.07}$	$0.46^{+0.04}_{-0.04}$	$0.46^{+0.05}_{-0.05}$	$0.51^{+0.02}_{-0.02}$	$0.34^{+0.17}_{-0.15}$	1150.9/939
2	Perseus CLUSTER	$4.95^{+0.01}_{-0.01}$	$1.74^{+0.11}_{-0.10}$	$0.49^{+0.05}_{-0.05}$	$0.44^{+0.02}_{-0.02}$	$0.30^{+0.02}_{-0.02}$	$0.50^{+0.01}_{-0.01}$	$0.67^{+0.10}_{-0.09}$	2160.6/1109
3	Ophiuchus CLUSTER	$9.35^{+0.06}_{-0.06}$	$1.12^{+0.26}_{-0.26}$	$0.84^{+0.12}_{-0.13}$	—	$0.64^{+0.06}_{-0.06}$	$0.51^{+0.01}_{-0.01}$	$0.78^{+0.14}_{-0.13}$	1089.9/600
4	ABELL 2199	$4.21^{+0.03}_{-0.03}$	$1.83^{+0.25}_{-0.24}$	$0.59^{+0.13}_{-0.12}$	$0.47^{+0.06}_{-0.07}$	$0.49^{+0.07}_{-0.08}$	$0.55^{+0.02}_{-0.02}$	$1.30^{+0.32}_{-0.31}$	1271.6/682
5	ABELL 0496	$3.99^{+0.03}_{-0.03}$	$2.38^{+0.25}_{-0.26}$	$0.68^{+0.12}_{-0.11}$	$0.64^{+0.06}_{-0.07}$	$0.59^{+0.06}_{-0.07}$	$0.63^{+0.02}_{-0.02}$	$1.24^{+0.27}_{-0.27}$	967.4/815
6	UGC 03957	$2.66^{+0.12}_{-0.09}$	$1.72^{+0.72}_{-0.66}$	$0.73^{+0.28}_{-0.26}$	$0.70^{+0.15}_{-0.14}$	$0.80^{+0.17}_{-0.17}$	$0.67^{+0.07}_{-0.06}$	$1.34^{+0.62}_{-0.60}$	588.2/588
7	IC 1365	$3.69^{+0.25}_{-0.32}$	—	—	$0.51^{+0.27}_{-0.27}$	—	$0.56^{+0.08}_{-0.09}$	—	583.2/548
8	ABELL 0754	$11.19^{+0.18}_{-0.18}$	—	—	—	$0.79^{+0.19}_{-0.18}$	$0.44^{+0.02}_{-0.02}$	$1.04^{+0.38}_{-0.38}$	1615.7/1130
9	Hydra A	$3.05^{+0.11}_{-0.11}$	—	—	$0.35^{+0.17}_{-0.18}$	$0.43^{+0.21}_{-0.21}$	$0.38^{+0.06}_{-0.06}$	—	784.3/718
10	ABELL 0085	$5.62^{+0.06}_{-0.06}$	—	$0.65^{+0.16}_{-0.16}$	$0.42^{+0.09}_{-0.09}$	$0.51^{+0.09}_{-0.10}$	$0.57^{+0.02}_{-0.01}$	$1.54^{+0.33}_{-0.32}$	1152.4/793
11	ABELL 2665	$3.22^{+0.19}_{-0.17}$	—	—	$0.50^{+0.27}_{-0.27}$	—	$0.46^{+0.09}_{-0.07}$	—	643.4/640
12	ABELL 3667	$6.51^{+0.09}_{-0.09}$	—	—	—	—	$0.38^{+0.03}_{-0.02}$	—	1723.2/885
13	ABELL 2319	$9.48^{+0.10}_{-0.17}$	—	—	—	$0.54^{+0.09}_{-0.09}$	$0.39^{+0.01}_{-0.01}$	$0.53^{+0.18}_{-0.18}$	2079.2/1351
14	ABELL 0133	$3.45^{+0.19}_{-0.15}$	$1.75^{+0.78}_{-0.76}$	—	$0.37^{+0.20}_{-0.19}$	—	$0.49^{+0.07}_{-0.06}$	—	762.1/741
15	ABELL S1101	$2.51^{+0.02}_{-0.03}$	$0.60^{+0.18}_{-0.17}$	$0.30^{+0.07}_{-0.08}$	$0.33^{+0.04}_{-0.04}$	$0.33^{+0.05}_{-0.05}$	$0.46^{+0.02}_{-0.02}$	$0.54^{+0.17}_{-0.16}$	1090.5/809
16	ABELL 2256	$6.39^{+0.08}_{-0.05}$	$0.86^{+0.32}_{-0.33}$	$0.48^{+0.17}_{-0.17}$	$0.23^{+0.09}_{-0.09}$	$0.28^{+0.11}_{-0.10}$	$0.39^{+0.01}_{-0.01}$	$0.54^{+0.27}_{-0.27}$	1102.8/767
17	ABELL 1831	$3.57^{+0.27}_{-0.26}$	—	—	—	—	$0.39^{+0.09}_{-0.08}$	—	590.5/553
18	ABELL 1795	$5.04^{+0.19}_{-0.20}$	$1.36^{+0.38}_{-0.38}$	—	$0.37^{+0.11}_{-0.11}$	$0.35^{+0.13}_{-0.13}$	$0.46^{+0.02}_{-0.03}$	—	542.8/442
19	ABELL 3112	$4.21^{+0.06}_{-0.03}$	$1.33^{+0.39}_{-0.39}$	$0.42^{+0.19}_{-0.18}$	$0.36^{+0.12}_{-0.12}$	$0.33^{+0.11}_{-0.10}$	$0.67^{+0.03}_{-0.03}$	$0.87^{+0.38}_{-0.38}$	1183.5/935
20	ZwCl 1742.1+3306	$3.40^{+0.08}_{-0.08}$	$1.76^{+0.88}_{-0.82}$	$0.99^{+0.37}_{-0.35}$	$0.51^{+0.22}_{-0.22}$	$0.48^{+0.20}_{-0.20}$	$0.58^{+0.06}_{-0.06}$	—	775.1/622
21	ABELL 2029	$6.71^{+0.67}_{-0.37}$	—	—	$0.72^{+0.37}_{-0.35}$	—	$0.55^{+0.05}_{-0.05}$	—	502.3/455
22	ABELL 2495	$3.53^{+0.33}_{-0.26}$	—	—	$0.46^{+0.25}_{-0.23}$	$0.49^{+0.24}_{-0.24}$	$0.54^{+0.08}_{-0.07}$	—	493.3/486
23	ABELL 2061	$4.24^{+0.59}_{-0.39}$	—	—	—	—	$0.38^{+0.08}_{-0.07}$	—	610.7/635
24	ABELL 2255	$6.09^{+0.29}_{-0.25}$	—	—	—	—	$0.33^{+0.03}_{-0.04}$	—	744.6/718
25	ABELL 2249	$4.64^{+0.41}_{-0.33}$	—	—	—	—	$0.37^{+0.05}_{-0.06}$	—	576.3/620
26	ZwCl 0040.8+2404	$3.01^{+0.10}_{-0.11}$	—	$0.71^{+0.37}_{-0.34}$	$0.50^{+0.23}_{-0.22}$	—	$0.56^{+0.06}_{-0.07}$	—	535.8/528
27	ABELL 2597	$3.20^{+0.08}_{-0.08}$	$1.51^{+0.59}_{-0.57}$	—	—	—	$0.41^{+0.04}_{-0.04}$	—	777.0/666
28	ABELL 2142	$8.37^{+0.09}_{-0.10}$	$1.29^{+0.61}_{-0.60}$	$0.56^{+0.32}_{-0.32}$	$0.24^{+0.13}_{-0.13}$	—	$0.42^{+0.02}_{-0.03}$	$0.88^{+0.37}_{-0.37}$	1011.2/737
29	ABELL 2244	$5.59^{+0.20}_{-0.30}$	$1.02^{+0.48}_{-0.48}$	—	$0.32^{+0.10}_{-0.11}$	—	$0.43^{+0.02}_{-0.02}$	—	478.1/442
30	PKS 0745-19	$6.20^{+0.10}_{-0.10}$	—	—	—	—	$0.50^{+0.03}_{-0.03}$	$1.00^{+0.46}_{-0.46}$	941.2/712
31	ABELL 1068	$4.06^{+0.12}_{-0.12}$	—	—	$0.76^{+0.25}_{-0.25}$	—	$0.57^{+0.07}_{-0.07}$	$2.55^{+1.24}_{-1.19}$	1232.9/840
32	ABELL 1413	$5.66^{+0.30}_{-0.27}$	—	—	—	—	$0.32^{+0.09}_{-0.09}$	—	838.1/727
33	ABELL 3364	$6.57^{+0.26}_{-0.25}$	—	—	—	—	$0.52^{+0.09}_{-0.08}$	—	711.0/641
34	ABELL 2204	$7.60^{+0.13}_{-0.13}$	—	—	$1.09^{+0.21}_{-0.20}$	—	$0.58^{+0.03}_{-0.04}$	$1.06^{+0.49}_{-0.49}$	1232.4/850
35	ABELL 2104	$8.11^{+0.32}_{-0.33}$	—	—	—	—	$0.42^{+0.07}_{-0.08}$	—	853.0/704

Table B.3: *continued.*

ID	Cluster	kT [keV]	Ne [solar]	Mg [solar]	Si [solar]	S=Ar=Ca [solar]	Fe [solar]	Ni [solar]	χ^2/d.o.f
36	ABELL 1914	$7.73^{+0.58}_{-0.58}$	—	—	—	—	$0.40^{+0.14}_{-0.13}$	—	731.7/579
37	ABELL 2218	$6.89^{+0.22}_{-0.19}$	—	—	—	—	$0.25^{+0.04}_{-0.04}$	—	627.2/593
38	ABELL 0665	$8.01^{+0.33}_{-0.32}$	—	—	—	—	$0.24^{+0.06}_{-0.07}$	—	1266.0/806
39	ABELL 1689	$9.61^{+0.38}_{-0.39}$	—	—	$0.99^{+0.47}_{-0.46}$	—	$0.48^{+0.07}_{-0.07}$	—	974.1/847
40	ABELL 0383	$4.10^{+0.09}_{-0.09}$	—	—	$0.50^{+0.19}_{-0.19}$	—	$0.60^{+0.06}_{-0.05}$	—	769.9/631
41	ABELL 1246	$5.69^{+0.22}_{-0.24}$	—	—	$0.64^{+0.31}_{-0.30}$	—	$0.33^{+0.04}_{-0.05}$	—	796.0/780
42	ABELL 2163	$12.61^{+0.36}_{-0.36}$	—	—	$0.78^{+0.32}_{-0.31}$	—	$0.38^{+0.04}_{-0.03}$	—	867.0/747
43	ABELL 0963	$6.08^{+0.23}_{-0.23}$	—	—	$0.65^{+0.32}_{-0.31}$	—	$0.48^{+0.06}_{-0.06}$	—	926.2/876
44	ABELL 0773	$7.43^{+0.31}_{-0.31}$	—	—	—	—	$0.33^{+0.06}_{-0.06}$	—	1067.5/707
45	ABELL 2219	$10.92^{+0.71}_{-0.60}$	—	—	$0.67^{+0.33}_{-0.31}$	—	$0.34^{+0.04}_{-0.03}$	—	609.1/483
46	ABELL 2390	$9.22^{+0.60}_{-0.66}$	—	—	$0.99^{+0.29}_{-0.29}$	$0.85^{+0.32}_{-0.32}$	$0.52^{+0.04}_{-0.04}$	—	601.6/482
47	ABELL 2667	$6.66^{+0.13}_{-0.22}$	—	—	—	—	$0.58^{+0.07}_{-0.07}$	—	1287.7/833
48	ABELL 1835	$7.61^{+0.38}_{-0.38}$	—	—	—	—	$0.42^{+0.09}_{-0.08}$	—	1100.2/833
49	SDSS CE J016.7	$2.99^{+0.13}_{-0.13}$	—	—	—	—	$0.32^{+0.08}_{-0.08}$	—	473.2/512
50	ABELL S1150	$3.61^{+0.96}_{-0.61}$	—	—	—	—	$0.59^{+0.73}_{-0.53}$	—	289.8/301
51	SDSS CE J355.9	$5.02^{+0.42}_{-0.40}$	—	—	—	—	$0.58^{+0.31}_{-0.22}$	—	369.7/372
52	ABELL 2537	$6.92^{+0.27}_{-0.20}$	—	—	—	—	$0.43^{+0.06}_{-0.05}$	—	1017.2/1000
53	Bullet Cluster	$10.57^{+1.39}_{-0.90}$	—	—	—	—	$0.40^{+0.06}_{-0.06}$	—	532.8/468
54	ABELL 2744	$10.32^{+0.21}_{-0.28}$	—	—	—	—	$0.32^{+0.05}_{-0.05}$	—	945.3/706
55	MS 1512.4+3647	$3.28^{+0.09}_{-0.09}$	—	—	$0.63^{+0.21}_{-0.20}$	$0.42^{+0.23}_{-0.23}$	$0.64^{+0.08}_{-0.07}$	$1.94^{+1.06}_{-1.02}$	1087.8/1014
56	SPT-CL J0234-5831	$5.49^{+0.71}_{-0.49}$	—	—	—	—	$0.40^{+0.23}_{-0.20}$	—	459.4/497
57	SPT-CL J0411-4819	$6.14^{+1.27}_{-0.99}$	—	—	—	—	$0.56^{+0.42}_{-0.35}$	—	184.4/226
58	LCDCS 0829	$11.37^{+0.30}_{-0.30}$	—	—	—	—	$0.47^{+0.04}_{-0.04}$	—	1004.1/823
59	MACS J0717+3745	$10.44^{+1.05}_{-0.67}$	—	—	—	—	$0.28^{+0.08}_{-0.09}$	—	829.5/691
60	SPT-CL J2337-5942	$9.47^{+1.98}_{-1.35}$	—	—	—	—	$0.75^{+0.79}_{-0.39}$	—	416.9/386
61	SPT-CL J2341-5119	$6.77^{+1.30}_{-0.98}$	—	—	—	—	$0.39^{+0.34}_{-0.29}$	—	629.8/643
62	SPT-CL J0546-5345	$6.01^{+1.04}_{-0.85}$	—	—	—	—	< 0.52	—	931.2/786

Table B.4: The metal abundance ratio to Fe.

ID	Cluster	Ne/Fe [solar]	Mg/Fe [solar]	Si/Fe [solar]	S/Fe [solar]	Ni/Fe [solar]	$N_{\rm SN\ II}/N_{\rm SN\ Ia}$
1	ABELL 0262	$3.14^{+0.47}_{-0.45}$	$0.92^{+0.16}_{-0.14}$	$0.90^{+0.09}_{-0.09}$	$0.90^{+0.10}_{-0.10}$	$0.67^{+0.33}_{-0.30}$	5.34 ± 0.70
2	Perseus CLUSTER	$3.48^{+0.23}_{-0.21}$	$0.98^{+0.10}_{-0.10}$	$0.88^{+0.04}_{-0.04}$	$0.60^{+0.04}_{-0.04}$	$1.34^{+0.20}_{-0.18}$	4.12 ± 0.30
3	Ophiuchus CLUSTER	$2.20^{+0.64}_{-0.62}$	$1.65^{+0.24}_{-0.26}$	—	$1.25^{+0.12}_{-0.12}$	$1.53^{+0.30}_{-0.30}$	12.42 ± 2.62
4	ABELL 2199	$3.33^{+0.47}_{-0.45}$	$1.07^{+0.24}_{-0.22}$	$0.86^{+0.11}_{-0.13}$	$0.89^{+0.13}_{-0.15}$	$2.36^{+0.59}_{-0.57}$	5.38 ± 0.90
5	ABELL 0496	$3.78^{+0.42}_{-0.43}$	$1.08^{+0.23}_{-0.21}$	$1.02^{+0.11}_{-0.13}$	$0.94^{+0.11}_{-0.14}$	$1.97^{+0.54}_{-0.51}$	7.20 ± 1.08
6	UGC 03957	$2.57^{+1.11}_{-1.01}$	$1.09^{+0.43}_{-0.40}$	$1.04^{+0.25}_{-0.23}$	$1.19^{+0.28}_{-0.28}$	$2.00^{+0.95}_{-0.91}$	6.78 ± 2.28
7	IC 1365	—	—	$0.91^{+0.50}_{-0.50}$	—	—	—
8	ABELL 0754	—	—	—	$1.80^{+0.55}_{-0.52}$	$2.36^{+1.13}_{-1.08}$	24.27 ± 14.62
9	Hydra A	—	—	$0.92^{+0.61}_{-0.58}$	$1.13^{+0.70}_{-0.67}$	—	5.15 ± 6.00
10	ABELL 0085	—	$1.14^{+0.10}_{-0.09}$	$0.74^{+0.74}_{-0.15}$	$0.90^{+0.04}_{-0.08}$	$2.70^{+0.59}_{-0.56}$	4.97 ± 0.44
11	ABELL 2665	—	—	$1.09^{+0.76}_{-0.70}$	—	—	—
12	ABELL 3667	—	—	—	—	—	—
13	ABELL 2319	—	—	—	$1.38^{+0.23}_{-0.23}$	$1.36^{+0.46}_{-0.46}$	21.67 ± 13.96
14	ABELL 0133	$3.57^{+1.93}_{-1.92}$	—	$0.76^{+0.07}_{-0.58}$	—	—	2.51 ± 0.58
15	ABELL S1101	$1.30^{+0.40}_{-0.37}$	$0.65^{+0.16}_{-0.18}$	$0.72^{+0.09}_{-0.09}$	$0.72^{+0.11}_{-0.11}$	$1.17^{+0.37}_{-0.35}$	2.80 ± 0.48
16	ABELL 2256	$2.21^{+0.82}_{-0.85}$	$1.23^{+0.44}_{-0.44}$	$0.59^{+0.23}_{-0.23}$	$0.72^{+0.28}_{-0.26}$	$1.38^{+0.69}_{-0.69}$	3.92 ± 1.40
17	ABELL 1831	—	—	—	—	—	—
18	ABELL 1795	$2.96^{+0.84}_{-0.85}$	—	$0.80^{+0.24}_{-0.25}$	$0.76^{+1.47}_{-1.76}$	—	4.68 ± 1.86
19	ABELL 3112	$1.99^{+0.74}_{-0.70}$	$0.63^{+0.14}_{-0.14}$	$0.54^{+0.21}_{-0.21}$	$0.49^{+0.19}_{-0.18}$	$1.30^{+0.26}_{-0.30}$	3.17 ± 0.68
20	ZwCl 1742.1+3306	$3.03^{+1.84}_{-1.83}$	$1.71^{+0.78}_{-0.77}$	$0.88^{+0.46}_{-0.47}$	$0.83^{+0.41}_{-0.43}$	—	6.40 ± 3.78
21	ABELL 2029	—	—	$1.31^{+0.77}_{-0.74}$	—	—	—
22	ABELL 2495	—	—	$0.85^{+0.63}_{-0.46}$	$0.91^{+0.60}_{-0.47}$	—	3.83 ± 4.76
23	ABELL 2061	—	—	—	—	—	—
24	ABELL 2255	—	—	—	—	—	—
25	ABELL 2249	—	—	—	—	—	—
26	ZwCl 0040.8+2404	—	$1.27^{+0.76}_{-0.62}$	$0.89^{+0.46}_{-0.35}$	—	—	5.11 ± 4.13
27	ABELL 2597	$3.68^{+1.56}_{-1.54}$	—	—	—	—	—
28	ABELL 2142	$3.07^{+1.06}_{-0.98}$	$1.33^{+0.56}_{-0.53}$	$0.57^{+0.22}_{-0.23}$	—	$2.10^{+0.50}_{-0.76}$	3.74 ± 1.56
29	ABELL 2244	$2.37^{+1.12}_{-1.12}$	—	$0.74^{+0.24}_{-0.26}$	—	—	3.32 ± 1.83
30	PKS 0745-19	—	—	—	—	$2.00^{+1.04}_{-1.13}$	—
31	ABELL 1068	—	—	$1.33^{+0.59}_{-0.52}$	—	$4.47^{+1.57}_{-1.46}$	4.91 ± 6.23
32	ABELL 1413	—	—	—	—	—	—
33	ABELL 3364	—	—	—	—	—	—
34	ABELL 2204	—	—	$1.88^{+0.38}_{-0.37}$	—	$1.83^{+0.96}_{-1.03}$	30.18 ± 32.93
35	ABELL 2104	—	—	—	—	—	—
36	ABELL 1914	—	—	—	—	—	—
37	ABELL 2218	—	—	—	—	—	—
38	ABELL 0665	—	—	—	—	—	—
39	ABELL 1689	—	—	$2.06^{+1.38}_{-1.18}$	—	—	—
40	ABELL 0383	—	—	$0.83^{+0.40}_{-0.38}$	—	—	—
41	ABELL 1246	—	—	$1.94^{+1.31}_{-1.06}$	—	—	—
42	ABELL 2163	—	—	$2.05^{+0.87}_{-0.83}$	—	—	—
43	ABELL 0963	—	—	$1.35^{+0.90}_{-0.75}$	—	—	—
44	ABELL 0773	—	—	—	—	—	—
45	ABELL 2219	—	—	$1.97^{+0.89}_{-0.95}$	—	—	—

Table B.4: *Continued.*

ID	Cluster	Ne/Fe [solar]	Mg/Fe [solar]	Si/Fe [solar]	S/Fe [solar]	Ni/Fe [solar]	$N_{\mathrm{SN\ II}}/N_{\mathrm{SN\ Ia}}$
46	ABELL 2390	—	—	$1.90^{+0.74}_{-0.68}$	$1.63^{+0.78}_{-0.77}$	—	25.49 ± 11.69
47	ABELL 2667	—	—	—	—	—	—
48	ABELL 1835	—	—	—	—	—	—
49	SDSS CE J016.7	—	—	—	—	—	—
50	ABELL S1150	—	—	—	—	—	—
51	SDSS CE J355.9	—	—	—	—	—	—
52	ABELL 2537	—	—	—	—	—	
53	Bullet Cluster	—	—	—	—	—	—
54	ABELL 2744	—	—	—	—	—	—
55	MS 1512.4+3647	—	—	$0.99^{+0.42}_{-0.38}$	$0.66^{+0.45}_{-0.45}$	$3.03^{+2.16}_{-2.06}$	3.59 ± 2.91
56	SPT-CL J0234-5831	—	—	—	—	—	—
57	SPT-CL J0411-4819	—	—	—	—	—	—
58	LCDCS 0829	—	—	—	—	—	—
59	MACS J0717+3745	—	—	—	—	—	—
60	SPT-CL J2337-5942	—	—	—	—	—	—
61	SPT-CL J2341-5119	—	—	—	—	—	—
62	SPT-CL J0546-5345	—	—	—	—	—	—

Table B.5: Color-Magnitude relation.

ID	Cluster	a[a]	b[a]	c[a]	$L^b_{\mathrm{limit},i}$	$L^b_{\mathrm{limit},g}$	$L_{\mathrm{total}}/L_{\mathrm{obs}}$		L^d_i	L^d_g
					$10^9 L_{\mathrm{solar}}$	$10^9 L_{\mathrm{solar}}$	i	g	$10^{12} L_{\mathrm{solar}}$	$10^{12} L_{\mathrm{solar}}$
2	PerseusCluster	-0.05882	2.03511	0.06	0.01	0.02	1.00001	1.00025	1.37	1.32
4	ABELL 2199	-0.04644	1.88202	0.11	0.02	0.04	1.00003	1.00046	2.16	1.73
7	IC 1365	-0.04919	2.00509	0.06	0.06	0.15	1.00011	1.00154	1.54	1.32
10	ABELL 0085	-0.05083	2.03648	0.03	0.07	0.17	1.00013	1.00177	2.25	1.85
11	ABELL 2665	-0.05181	2.06635	0.06	0.07	0.20	1.00015	1.00206	2.02	1.71
16	ABELL 2256	-0.03333	1.77848	0.05	0.08	0.20	1.00016	1.00210	2.50	2.02
17	ABELL 1831	-0.04867	2.09460	0.06	0.08	0.21	1.00018	1.00215	1.26	1.00
18	ABELL 1795	-0.05489	2.13629	0.06	0.08	0.21	1.00018	1.00215	1.41	1.21
21	ABELL 2029	-0.02319	1.67101	0.06	0.14	0.37	1.00035	1.00387	3.15	2.83
22	ABELL 2495	-0.06757	2.46749	0.06	0.15	0.40	1.00037	1.00419	1.41	1.21
23	ABELL 2061	-0.02937	1.74866	0.11	0.14	0.36	1.00035	1.00373	2.64	2.27
24	ABELL 2255	-0.04815	2.05473	0.05	0.15	0.38	1.00037	1.00391	2.94	2.41
25	ABELL 2249	-0.05999	2.30426	0.06	0.15	0.39	1.00038	1.00400	3.35	2.68
26	ZwCl 0040.8+2404	-0.06014	2.33271	0.05	0.16	0.42	1.00041	1.00436	1.14	0.94
28	ABELL 2142	-0.04612	2.09398	0.06	0.20	0.53	1.00054	1.00550	5.20	4.53
29	ABELL 2244	-0.06768	2.49747	0.06	0.21	0.56	1.00060	1.00579	1.86	1.61
31	ABELL 1068	-0.04191	2.21546	0.06	0.47	1.37	1.00167	1.01427	0.94	0.80
32	ABELL 1413	-0.10984	3.41217	0.06	0.47	1.29	1.00166	1.01345	2.28	1.99
36	ABELL 1914	-0.07892	3.00833	0.06	0.74	2.27	1.00301	1.02381	2.44	2.19
38	ABELL 0665	-0.08752	3.22925	0.06	0.88	2.86	1.00377	1.03014	2.90	2.55
39	ABELL 1689	-0.13789	4.07464	0.06	0.79	2.31	1.00330	1.02422	3.21	2.76
41	ABELL 1246	-0.10008	3.48276	0.11	0.93	2.92	1.00403	1.03078	3.83	3.36
43	ABELL 0963	-0.10975	3.69709	0.11	1.08	3.44	1.00493	1.03634	1.93	2.21
44	ABELL 0773	-0.10230	3.69330	0.13	1.28	4.42	1.00612	1.04696	4.50	3.83
45	ABELL 2219	-0.12808	4.18645	0.11	1.38	4.72	1.00673	1.05015	5.42	4.02
46	ABELL 2390	-0.04597	2.72130	0.05	1.80	8.27	1.00954	1.08964	3.92	4.80
48	ABELL 1835	-0.08530	3.44933	0.11	1.92	7.61	1.01035	1.08214	5.39	5.45
52	ABELL 2537	-0.06612	3.33322	0.05	3.31	17.92	1.02094	1.20430	2.95	3.60

[a] Color-magnitude relation parameters of the form: $|color - (a \times m_{\mathrm{band}} + b)| < c$.

[b] Luminosity cutoff value.

[c] correction factor of galaxy luminosities due to the luminosity cutoff.

[d] Background subtracted and corrected total luminosity.

Appendix C

Observation Logs

Table C.1: *Suzaku* observation logs.

ID	Cluster		ObsID[a]	R.A.[b] [J2000.0]	Decl.[b] [J2000.0]	Date[c]	Exposure[d] [ksec]	Exposure[e] [ksec]
1	ABELL 0262	1	802001010	28.1922	36.1591	2007 Aug 17	26.3	18.8
		2	802079010	28.5344	36.2686	2007 Aug 06	43.6	37.2
		3	802080010	28.0598	36.4356	2007 Aug 08	40.2	30.7
2	Perseus CLUSTER	1	800010010	49.9554	41.5039	2006 Feb 01	32.5	20.6
		2	804056010	50.3027	41.5257	2009 Jul 29	9.7	6.1
		3	804057010	50.6767	41.5228	2009 Jul 29	11.0	8.4
		4	804058010	51.0503	41.5202	2009 Jul 29	4.1	4.1
		5	804059010	51.4246	41.5162	2009 Jul 30	21.9	16.7
		6	804060010	51.7975	41.5108	2009 Jul 30	12.6	11.4
		7	804061010	52.1705	41.5044	2009 Jul 31	26.8	20.2
		8	804062010	52.5439	41.4965	2009 Jul 31	23.6	18.4
		9	804063010	49.7797	41.7196	2009 Aug 18	14.7	11.2
		10	804064010	49.5875	41.9633	2009 Aug 19	13.2	7.4
		11	804066010	49.2103	42.4455	2009 Aug 19	23.6	16.8
		12	804067010	49.0181	42.6863	2009 Aug 20	10.6	8.0
		13	804068010	48.8242	42.9264	2009 Aug 20	26.9	26.9
		14	804069010	48.6285	43.1676	2009 Aug 21	33.0	22.7
		15	805096010	49.8666	41.2611	2010 Aug 16	1.6	1.1
		16	805097010	49.8015	40.9830	2010 Aug 17	10.9	9.3
		17	805098010	49.7347	40.7118	2010 Aug 17	11.1	5.2
		18	805099010	49.6689	40.4337	2010 Aug 17	11.2	6.2
		19	805100010	49.6049	40.1572	2010 Aug 18	10.6	7.6
		20	805101010	49.5399	39.8840	2010 Aug 18	9.8	6.7
		21	805102010	49.4762	39.6090	2010 Aug 19	16.1	9.4
		22	805103010	49.5928	41.5523	2010 Aug 20	10.1	4.9
		23	805104010	49.2188	41.5721	2010 Aug 20	10.0	5.1
		24	805105010	48.8462	41.5856	2010 Aug 20	1.7	1.3
		25	805106010	48.4696	41.6016	2010 Aug 21	10.4	8.9
		26	805107010	48.1001	41.6131	2010 Aug 21	7.9	4.7
		27	805108010	47.7251	41.6255	2010 Aug 22	15.4	10.3
		28	805109010	47.3511	41.6379	2010 Aug 23	15.4	14.8
		29	805110010	49.6359	40.2959	2010 Aug 18	3.6	3.6
		30	805111010	49.5719	40.0219	2010 Aug 18	11.2	5.1
		31	805112010	49.5080	39.7472	2010 Aug 19	15.7	10.4
		32	805113010	49.4444	39.4701	2010 Aug 20	9.4	8.5
		33	805114010	48.2846	41.6054	2010 Aug 21	10.9	5.4
		34	805115010	47.9127	41.6204	2010 Aug 21	3.4	3.4
		35	805116010	47.5391	41.6300	2010 Aug 22	16.0	10.3
		36	805117010	47.1647	41.6449	2010 Aug 23	15.1	7.3
		37	806099010	49.6666	41.3604	2011 Aug 30	6.5	6.0
		38	806100010	49.3858	41.1787	2011 Aug 27	3.8	3.8
		39	806101010	49.2375	41.0889	2011 Aug 27	10.7	8.0
		40	806102010	49.1020	40.9982	2011 Aug 28	12.0	6.1
		41	806103010	48.9544	40.9043	2011 Aug 28	10.3	9.3
		42	806104010	48.8197	40.8139	2011 Aug 28	13.2	12.7
		43	806105010	48.6726	40.7228	2011 Aug 28	10.8	7.4
		44	806106010	48.5394	40.6338	2011 Aug 29	15.5	9.6
		45	806107010	48.3936	40.5388	2011 Aug 29	5.6	5.3
		46	806108010	48.2625	40.4485	2011 Aug 29	11.6	8.6
		47	806109010	48.1163	40.3561	2011 Aug 30	11.6	5.2

Table C.1: *continued.*

ID	Cluster		ObsID[a]	R.A.[b] [J2000.0]	Decl.[b] [J2000.0]	Date[c]	Exposure[d] [ksec]	Exposure[e] [ksec]
2	Perseus CLUSTER	48	806110010	47.9840	40.2680	2011 Aug 30	4.5	3.9
		49	806112010	50.4145	41.1258	2011 Aug 24	7.9	7.6
		50	806113010	50.5437	41.0145	2011 Aug 24	11.1	8.1
		51	806114010	50.6611	40.9157	2011 Aug 25	11.8	7.2
		52	806115010	50.7904	40.8069	2011 Aug 25	1.1	0.7
		53	806116010	50.9063	40.7039	2011 Aug 25	7.8	7.5
		54	806117010	51.0328	40.5957	2011 Aug 25	12.0	8.3
		55	806118010	51.1493	40.4958	2011 Aug 26	10.9	6.2
		56	806119010	51.2770	40.3868	2011 Aug 26	7.9	7.2
		57	806120010	51.3915	40.2857	2011 Aug 26	10.1	6.9
		58	806121010	51.5164	40.1750	2011 Aug 27	10.2	5.4
		59	806122010	51.6308	40.0717	2011 Aug 27	2.3	2.0
		60	806123010	50.2177	41.6975	2011 Sep 05	10.9	7.5
		61	806124010	50.5182	41.8628	2011 Sep 04	10.2	7.0
		62	806125010	50.6676	41.9537	2011 Sep 04	9.8	4.5
		63	806126010	50.8162	42.0347	2011 Sep 05	6.1	2.4
		64	806127010	50.9699	42.1175	2011 Sep 05	4.8	4.8
		65	806128010	51.1184	42.2072	2011 Sep 04	10.3	10.3
		66	806129010	51.2710	42.2915	2011 Sep 05	10.4	5.4
		67	806130010	51.4212	42.3710	2011 Sep 06	7.5	3.1
		68	806131010	51.5754	42.4541	2011 Sep 06	14.9	11.5
		69	806132010	51.7255	42.5390	2011 Sep 06	11.4	5.5
		70	806133010	51.8822	42.6245	2011 Sep 07	6.0	2.1
		71	806134010	52.0330	42.7019	2011 Sep 07	5.8	5.1
		72	806135010	50.0010	41.7793	2011 Aug 30	11.4	7.3
		73	806136010	50.0870	42.0498	2011 Aug 31	10.7	4.9
		74	806137010	50.1251	42.1872	2011 Aug 31	4.5	4.2
		75	806138010	50.1707	42.3226	2011 Aug 31	5.0	4.3
		76	806139010	50.2092	42.4612	2011 Aug 31	10.0	7.1
		77	806140010	50.2584	42.5938	2011 Sep 01	11.8	5.6
		78	806141010	50.2947	42.7325	2011 Sep 02	1.4	0.8
		79	806142010	50.3399	42.8692	2011 Sep 02	14.3	11.8
		80	806143010	50.3796	43.0058	2011 Sep 02	16.5	7.6
		81	806144010	50.4234	43.1429	2011 Sep 03	2.0	2.0
		82	806145010	50.4676	43.2769	2011 Sep 03	12.0	9.2
		83	806146010	50.5088	43.4191	2011 Sep 03	11.1	6.2
		84	801049010	49.6445	42.0680	2006 Sep 02	15.7	9.5
		85	801049020	49.2788	41.3719	2006 Sep 02	32.5	23.5
		86	801049030	50.2242	41.1004	2006 Sep 03	32.9	27.9
		87	801049040	50.5735	41.8053	2006 Sep 04	9.8	5.3
		88	805045010	49.9430	41.2145	2011 Feb 23	14.0	12.5
		89	805046010	49.9431	41.7900	2011 Feb 17	20.7	16.6
		90	805047010	50.3247	41.3807	2011 Feb 04	11.7	6.5
		91	805048010	50.3251	41.6598	2011 Feb 03	18.2	12.2
3	Ophiuchus CLUSTER	1	801021010	258.0174	-23.3865	2007 Mar 24	9.8	4.3
		2	801022010	258.2981	-23.3868	2007 Mar 21	23.3	16.7
		3	801023010	257.7375	-23.3864	2007 Mar 22	17.5	11.2
		4	801026010	258.0184	-23.1077	2007 Mar 22	22.4	12.2
		5	801029010	258.0175	-23.6665	2007 Mar 23	18.3	12.3
		6	802046010	258.1093	-23.3790	2007 Sep 24	86.5	51.4

Table C.1: *continued.*

ID	Cluster		ObsID[a]	R.A.[b] [J2000.0]	Decl.[b] [J2000.0]	Date[c]	Exposure[d] [ksec]	Exposure[e] [ksec]
3	Ophiuchus CLUSTER	7	801030010	257.0147	-25.0612	2007 Mar 24	14.9	11.6
4	ABELL 2199	1	801056010	247.1922	39.4840	2006 Oct 01	23.5	13.0
		2	801057010	247.0269	39.6504	2006 Oct 01	15.4	12.2
		3	801058010	247.3619	39.6495	2006 Oct 03	15.7	10.3
		4	801059010	247.3596	39.3165	2006 Oct 04	25.2	14.7
		5	801060010	247.0296	39.3161	2006 Oct 04	20.7	17.0
		6	805042010	246.7666	40.2374	2010 Sep 19	49.8	39.6
		7	806147010	247.4695	38.9998	2011 Aug 16	13.9	12.4
		8	806148010	247.0222	38.9947	2011 Aug 17	20.3	9.9
		9	806149010	246.6242	39.5648	2011 Aug 17	14.9	12.8
		10	806150010	247.7662	39.3698	2011 Aug 18	18.7	9.9
		11	806151010	248.9722	38.6569	2011 Aug 18	14.5	12.4
		12	806152010	247.2752	38.7861	2011 Aug 19	20.6	11.4
		13	806153010	247.8714	39.0623	2011 Aug 19	29.0	18.7
		14	806155010	246.6190	38.9138	2011 Sep 12	17.6	13.2
		15	806156010	245.7785	38.4489	2011 Dec 27	31.3	25.1
		16	806157010	246.6136	39.2216	2011 Sep 11	8.2	5.7
		17	806158010	246.9232	39.9293	2011 Sep 16	12.2	6.9
		18	806159010	247.4008	39.9951	2011 Sep 11	27.9	24.0
		19	806160010	246.2604	39.5212	2011 Sep 21	15.3	10.0
		20	806161010	246.4820	39.8890	2011 Sep 19	26.0	22.0
		21	806162010	247.7994	39.6960	2011 Oct 06	28.3	17.4
5	ABELL 0496	1	803048010	68.2513	-13.0087	2008 Jul 27	31.9	21.1
		2	803073010	68.4146	-13.2791	2008 Aug 02	44.2	28.2
6	UGC 03957	1	801072010	115.2433	55.4290	2006 Apr 16	10.8	7.6
7	IC 1365	1	801075010	318.5228	2.5728	2006 May 09	10.8	6.9
8	ABELL 0754	1	802063010	137.2113	-9.6361	2007 May 29	78.5	50.5
9	Hydra A	1	805007010	139.3695	-11.9475	2010 Nov 08	35.7	22.0
		2	805008010	139.6720	-11.9467	2010 Nov 09	34.9	20.5
10	ABELL 0085	1	801041010	10.4739	-9.4292	2007 Jan 05	89.9	56.2
11	ABELL 2665	1	801076010	357.7161	6.1352	2006 Dec 09	9.4	4.9
12	ABELL 3667	1	801094010	302.5617	-56.3599	2006 May 03	71.7	44.4
		2	801095010	302.8177	-56.5600	2006 May 06	17.3	11.9
		3	801095020	302.8690	-56.6666	2006 Oct 30	12.0	7.1
		4	801096010	303.1410	-56.7974	2006 May 06	20.9	17.9
		5	805036010	303.4605	-57.0338	2010 Apr 12	52.5	33.1
13	ABELL 2319	1	801040010	290.3341	43.8780	2006 Oct 27	90.0	72.7
		2	806014010	290.2404	44.0121	2011 Dec 30	104.8	90.9
14	ABELL 0133	1	805019010	15.4513	-21.8877	2010 Jun 07	40.8	24.6
		2	805020010	15.6732	-21.6726	2010 Jun 05	50.2	35.7
		3	805021010	15.9075	-21.8935	2010 Jun 09	42.9	29.0
		4	805022010	15.6819	-22.1029	2010 Jun 08	36.7	21.8
15	ABELL S1101	1	801093010	348.4959	-42.7314	2006 Apr 26	64.5	41.0
16	ABELL 2256	1	801061010	256.0138	78.7112	2006 Nov 10	78.3	72.6
17	ABELL 1831	1	801077010	209.8007	27.9693	2006 Jul 21	8.9	5.7
18	ABELL 1795	1	800012010	207.2241	26.6010	2005 Dec 10	10.4	8.1
		2	800012020	207.2221	26.7993	2005 Dec 10	22.1	17.5
		3	800012030	207.2230	26.9995	2005 Dec 11	40.0	31.4
		4	800012040	207.2228	26.4007	2005 Dec 11	40.1	35.7
		5	800012050	207.2227	26.2001	2005 Dec 12	38.4	30.1

Table C.1: *continued.*

ID	Cluster		ObsID[a]	R.A.[b] [J2000.0]	Decl.[b] [J2000.0]	Date[c]	Exposure[d] [ksec]	Exposure[e] [ksec]
18	ABELL 1795	6	804082010	207.4803	26.8793	2009 Jun 28	35.5	27.0
		7	804083010	206.9673	26.3143	2009 Jun 29	23.3	22.7
		8	804084010	206.8240	26.6950	2009 Jun 26	26.1	23.3
		9	804085010	206.9975	26.5902	2009 Jun 27	24.3	22.6
19	ABELL 3112	1	803054010	49.4785	-44.2477	2008 May 23	52.2	32.0
20	ZwCl 1742.1+3306	1	801079010	266.0474	32.9693	2006 Aug 14	14.9	10.4
21	ABELL 2029	1	804024010	227.7409	5.7498	2010 Jan 28	4.2	2.9
		2	804024020	227.8527	6.0108	2010 Jan 28	26.0	17.2
		3	804024030	227.6311	5.4874	2010 Jan 28	17.9	14.1
		4	804024040	228.0053	5.6496	2010 Jan 29	25.7	15.7
		5	804024050	227.4808	5.8608	2010 Jan 30	21.9	13.5
22	ABELL 2495	1	801080010	342.5777	10.9124	2006 Nov 22	0.2	0.1
		2	801080020	342.5662	10.9218	2007 Jun 09	11.9	9.8
23	ABELL 2061	1	801081010	230.3095	30.6453	2006 Jul 27	13.9	9.5
24	ABELL 2255	1	804041010	258.2484	64.1467	2010 Feb 07	44.5	37.5
25	ABELL 2249	1	801082010	257.4600	34.4851	2007 Jan 14	22.8	21.9
26	ZwCl 0040.8+2404	1	801083010	10.9622	24.4059	2006 Jul 28	12.9	9.0
27	ABELL 2597	1	807073010	351.4175	-11.9496	2012 Nov 30	35.5	24.3
		2	807073020	351.1561	-12.0446	2012 Dec 01	50.1	35.9
		3	807073030	351.5123	-12.2071	2012 Dec 02	42.0	25.6
		4	807073040	351.2512	-12.2980	2012 Dec 03	40.9	25.9
28	ABELL 2142	1	801055010	239.5312	27.2879	2007 Jan 04	39.5	33.3
		2	802030010	239.3897	27.3899	2007 Aug 04	30.5	19.6
		3	802031010	239.2185	27.5666	2007 Sep 15	57.7	41.4
		4	802032010	239.0356	27.7434	2007 Aug 29	16.8	13.4
29	ABELL 2244	1	802078010	255.6885	34.0502	2007 Oct 19	60.6	51.0
30	PKS 0745-19	1	802062010	116.8852	-19.2901	2007 May 11	21.3	14.1
		2	802062020	116.6543	-19.2063	2007 May 11	27.4	17.9
		3	802062030	116.9737	-19.0727	2007 May 12	26.8	18.8
		4	802062040	117.1155	-19.3739	2007 May 13	32.9	28.1
		5	802062050	116.7966	-19.5079	2007 May 14	25.5	19.9
		6	805083010	117.0925	-18.8008	2010 Nov 14	37.2	25.7
		7	805084010	116.7033	-18.9048	2010 Apr 29	21.3	14.8
		8	805085010	116.3632	-19.0871	2010 Apr 30	29.3	22.6
		9	805086010	116.4685	-19.4632	2010 May 01	23.7	21.8
		10	805087010	116.6522	-19.7838	2010 Nov 15	31.3	19.9
31	ABELL 1068	1	806028010	160.1718	40.1411	2011 Oct 26	43.5	24.5
		2	806028020	160.4236	39.9791	2011 Oct 27	43.7	24.8
		3	806028030	160.2123	39.7867	2011 Oct 29	44.6	32.1
		4	806028040	159.9611	39.9499	2011 Oct 30	42.5	27.3
32	ABELL 1413	1	800001010	178.8303	23.6485	2005 Nov 15	107.4	76.1
		2	805059010	178.8510	23.2234	2010 May 29	32.8	19.9
		3	805060010	178.6363	23.4218	2010 May 30	32.8	20.5
		4	805061010	179.0207	23.4251	2010 May 31	41.0	27.8
33	ABELL 3364	1	806067010	86.8402	-31.7251	2011 Apr 18	19.8	12.9
		2	806067020	87.0888	-31.8215	2011 Apr 19	30.0	21.7
		3	806067030	86.7248	-31.9341	2011 Apr 19	30.8	27.2
		4	806067040	86.9739	-32.0342	2011 Apr 20	31.9	22.6
34	ABELL 2204	1	801091010	248.0963	5.6404	2006 Sep 17	34.8	32.9
		2	805056010	248.3552	5.4547	2010 Sep 01	40.7	29.7

Table C.1: *continued.*

ID	Cluster		ObsID[a]	R.A.[b] [J2000.0]	Decl.[b] [J2000.0]	Date[c]	Exposure[d] [ksec]	Exposure[e] [ksec]
34	ABELL 2204	3	805057010	248.1003	5.3993	2010 Aug 27	39.7	27.5
		4	805058010	248.3129	5.7152	2010 Aug 28	36.2	25.4
35	ABELL 2104	1	801001010	234.9146	-3.2969	2007 Jan 21	19.9	16.1
		2	801002010	235.0318	-3.1802	2007 Jan 19	13.8	7.2
		3	801003010	235.1486	-3.2970	2007 Jan 18	20.4	12.2
		4	801004010	235.0317	-3.4139	2007 Jan 20	11.3	6.7
36	ABELL 1914	1	805091010	216.5507	38.0175	2010 Jun 15	25.7	20.8
		2	805091020	216.5784	38.0421	2011 Jan 04	11.4	9.8
		3	805092010	216.7383	37.7630	2010 Jun 16	28.6	24.1
		4	805092020	216.7700	37.7885	2011 Jan 04	17.1	9.3
		5	805093010	216.2252	37.8719	2010 Jun 17	28.5	24.7
		6	805093020	216.2544	37.8950	2011 Jan 05	12.8	10.4
		7	805094010	216.4138	37.6152	2010 Jun 18	25.2	23.5
		8	805094020	216.4424	37.6372	2011 Jan 05	17.4	12.2
37	ABELL 2218	1	100030010	249.0001	66.2030	2005 Oct 01	32.5	27.6
		2	800019010	249.0052	66.2050	2005 Oct 26	31.8	27.9
		3	100030020	244.4769	65.4468	2005 Oct 02	43.8	39.1
		4	800020010	249.9091	65.2119	2005 Oct 27	14.9	11.7
38	ABELL 0665	1	807072010	128.1540	65.9045	2012 Apr 09	35.0	20.9
		2	807072020	127.5519	65.9953	2012 Apr 10	51.4	36.0
		3	807072030	127.3329	65.7462	2012 Apr 10	50.4	43.1
		4	807072040	127.9330	65.6581	2012 Apr 11	52.8	43.1
39	ABELL 1689	1	803024010	198.0484	-1.2633	2008 Jul 23	38.0	24.0
		2	803025010	197.9560	-1.5158	2008 Jul 24	43.5	33.4
		3	803026010	197.7048	-1.4241	2008 Jul 25	44.1	34.7
		4	803027010	197.7965	-1.1735	2008 Jul 26	42.0	33.0
40	ABELL 0383	1	805062010	42.1211	-3.4616	2010 Jul 11	40.4	34.2
		2	805063010	41.9447	-3.4083	2010 Jul 12	31.6	25.2
		3	805064010	41.9643	-3.6473	2010 Jul 13	32.0	25.6
41	ABELL 1246	1	804028010	170.9992	21.4865	2009 Nov 16	34.1	24.7
		2	804029010	171.1280	21.4191	2009 Nov 28	69.5	45.4
42	ABELL 2163	1	803022010	244.0260	-6.0591	2009 Feb 08	109.7	69.6
		2	803071010	243.8156	-6.2315	2008 Aug 18	51.8	33.9
43	ABELL 0963	1	802010010	154.2645	39.1732	2007 Nov 24	20.1	13.5
		2	802011010	154.4148	39.0556	2007 Nov 23	27.9	15.7
		3	802012010	154.2641	38.9388	2007 Nov 28	24.5	18.3
44	ABELL 0773	1	806027010	139.6885	51.8172	2011 May 01	42.6	34.4
		2	806027020	139.6415	51.5835	2011 May 02	35.1	26.2
		3	806027030	139.2619	51.6127	2011 May 03	47.6	35.3
		4	806027040	139.3092	51.8461	2011 May 03	49.9	37.8
45	ABELL 2219	1	804011010	250.0709	46.7200	2009 Apr 03	95.7	62.9
46	ABELL 2390	1	804012010	328.3984	17.7035	2009 May 04	71.4	54.2
47	ABELL 2667	1	806029010	357.9715	-25.9262	2011 Jun 09	44.3	24.3
		2	806029020	357.7341	-26.0226	2011 Jun 10	40.0	27.2
		3	806029030	357.8478	-26.2362	2011 Jun 12	52.3	35.1
		4	806029040	358.0843	-26.1324	2011 Jun 13	43.8	27.6
48	ABELL 1835	1	805037010	210.4410	2.9038	2010 Jul 05	48.0	31.6
		2	805038010	210.2863	2.6798	2010 Jul 07	43.8	29.6
		3	805039010	210.0673	2.8311	2010 Jul 08	47.1	27.8
		4	805040010	210.2225	3.0556	2010 Jul 13	41.8	26.9

Table C.1: *continued.*

ID	Cluster		ObsID[a]	R.A.[b] [J2000.0]	Decl.[b] [J2000.0]	Date[c]	Exposure[d] [ksec]	Exposure[e] [ksec]
49	SDSS CE J016.7	1	801050010	16.7077	1.0407	2007 Jan 10	20.8	14.4
50	ABELL S1150	1	803057010	356.9535	-35.5892	2008 May 31	6.0	5.4
51	SDSS CE J355.9	1	803001010	355.9117	0.3303	2008 Jun 27	41.5	25.6
52	ABELL 2537	1	805090010	347.0895	-2.1864	2010 Jun 21	120.8	79.4
53	Bullet Cluster	1	801089010	104.7040	-55.9330	2006 Dec 26	88.6	57.9
54	ABELL 2744	1	802033010	3.5397	-30.3446	2007 May 19	133.5	82.0
		2	805015010	3.5132	-30.5508	2010 Dec 10	69.8	47.8
55	MS 1512.4+3647	1	802034010	228.6059	36.6198	2007 Dec 29	268.9	208.6
56	SPT-CL J0234-5831	1	804003010	38.6494	-58.5096	2010 Jan 16	12.3	7.4
57	SPT-CL J0411-4819	1	805024010	62.816	-48.3247	2010 Sep 22	5.5	4.8
58	LCDCS 0829	1	801013010	206.8560	-11.8093	2006 Jun 30	62.0	40.0
		2	801013020	206.8558	-11.8095	2006 Jul 15	77.7	58.9
59	MACS J0717+3745	1	806006010	109.4283	37.7329	2011 Oct 07	83.9	69.5
60	SPT-CL J2337-5942	1	806073010	354.3472	-59.7060	2011 Apr 23	33.8	21.4
61	SPT-CL J2341-5119	1	806072010	355.3013	-51.3330	2011 May 22	87.8	59.4
62	SPT-CL J0546-5345	1	806071010	86.6400	-53.7518	2011 Aug 08	79.3	50.9

[a] *Suzaku* observation identifier.
[b] Nominal pointing position of the observation in Equinox 2000.0.
[c] Start time of the observation in universal time coordinated.
[d] Cleaned exposure time of each observation in the case of COR$>$ 0 GV.
[e] Cleaned exposure time of each observation in the case of COR$>$ 8 GV.

Table C.2: *Chandra* observation logs.

ID	Cluster		ObsID[a]	R.A.[b] [J2000.0]	Decl.[b] [J2000.0]	Date[c]	Exposure[d] [ksec]
1	ABELL 0262	1	2215	28.194	36.152	2001 Aug 03	28.7
		2	7921	28.194	36.152	2006 Nov 20	110.7
2	Perseus CLUSTER	1	502	49.952	41.508	1999 Sep 20	5.1
		2	503	49.952	41.508	1999 Nov 28	9.0
		3	1513	49.952	41.508	2000 Jan 29	24.9
		4	3209	49.948	41.510	2002 Aug 08	95.8
		5	4289	49.948	41.510	2002 Aug 10	95.4
		6	3404	49.948	41.510	2002 Aug 11	5.3
		7	6139	49.951	41.512	2004 Oct 04	56.4
		8	4946	49.951	41.512	2004 Oct 06	23.7
		9	4948	49.951	41.512	2004 Oct 09	118.6
		10	4947	49.951	41.512	2004 Oct 11	29.8
		11	4949	49.951	41.512	2004 Oct 12	29.4
		12	4950	49.951	41.512	2004 Oct 12	96.9
		13	4952	49.951	41.512	2004 Oct 14	164.2
		14	4951	49.951	41.512	2004 Oct 17	96.1
		15	4953	49.951	41.512	2004 Oct 18	30.1
		16	6145	49.951	41.512	2004 Oct 19	85.0
		17	6146	49.951	41.512	2004 Oct 20	47.1
		18	11716	49.934	41.422	2009 Oct 10	39.6
		19	12025	49.882	41.630	2009 Nov 25	17.9
		20	12033	49.882	41.630	2009 Nov 27	18.9
		21	11713	49.882	41.630	2009 Nov 29	112.2
		22	12036	49.882	41.630	2009 Dec 02	47.9
		23	11715	49.934	41.422	2009 Dec 02	73.4
		24	12037	49.934	41.422	2009 Dec 05	84.6
		25	11714	49.928	41.569	2009 Dec 07	92.0
3	Ophiuchus CLUSTER	1	3200	258.116	-23.370	2002 Oct 21	50.5
4	ABELL 2199	1	498	247.160	39.551	1999 Dec 11	18.9
		2	497	247.160	39.551	2000 May 13	19.5
		3	10804	247.160	39.551	2009 Jun 23	18.8
		4	10803	247.160	39.551	2009 Nov 17	30.2
		5	10748	247.160	39.551	2009 Nov 19	40.6
		6	10805	247.160	39.551	2009 Nov 23	30.3
5	ABELL 0496	1	931	68.408	-13.262	2000 Jul 28	18.9
		2	3361	68.408	-13.262	2001 Oct 04	10.0
		3	4976	68.404	-13.238	2004 Jul 22	75.1
6	UGC 03957	1	8265	115.219	55.431	2006 Dec 24	7.9
7	IC 1365	1	10747	318.493	2.559	2009 Jul 05	10.0
8	ABELL 0754	1	577	137.288	-9.661	1999 Oct 30	44.2
		2	10743	137.438	-9.692	2009 Feb 17	94.1
		3	6793	137.558	-9.928	2006 Jan 18	9.9
		4	6794	137.288	-9.928	2006 Jan 27	9.9
		5	6795	137.017	-9.928	2006 Jan 28	9.7
		6	6796	137.558	-9.661	2006 Jan 18	9.7
		7	6797	137.017	-9.661	2006 Jan 25	10.0
		8	6798	137.558	-9.399	2006 Jan 28	10.0
		9	6799	137.288	-9.394	2006 Jan 28	9.7
		10	6800	137.017	-9.394	2006 Feb 15	10.2
9	Hydra A	1	575	139.524	-12.096	1999 Oct 30	23.9

Table C.2: *Continued.*

ID	Cluster		ObsID[a]	R.A.[b] [J2000.0]	Decl.[b] [J2000.0]	Date[c]	Exposure[d] [ksec]
9	Hydra A	2	576	139.524	-12.096	1999 Nov 02	19.5
		3	2208	139.524	-12.096	2000 Nov 13	9.5
		4	2330	139.524	-12.096	2001 Jan 04	9.6
		5	2331	139.524	-12.096	2001 Feb 04	9.5
		6	2332	139.524	-12.096	2001 Mar 25	9.8
		7	2333	139.524	-12.096	2001 May 08	9.9
		8	2334	139.524	-12.096	2001 May 16	10.0
		9	4969	139.524	-12.095	2004 Jan 13	96.9
		10	4970	139.524	-12.095	2004 Oct 22	98.8
10	ABELL 0085	1	904	10.441	-9.379	2000 Aug 19	38.4
11	ABELL 2665	1	12280	357.709	6.156	2011 Jan 17	9.9
12	ABELL 3667	1	513	303.210	-56.849	1999 Sep 22	44.8
		2	889	302.958	-56.759	2000 Sep 09	50.3
		3	5751	303.280	-56.890	2005 Jun 07	128.9
		4	6292	303.280	-56.890	2005 Jun 10	46.7
		5	5752	303.280	-56.890	2005 Jun 12	60.4
		6	6295	303.280	-56.890	2005 Jun 15	49.5
		7	5753	303.280	-56.890	2005 Jun 17	103.6
		8	6296	303.280	-56.890	2005 Jun 19	49.4
13	ABELL 2319	1	3231	290.300	43.945	2002 Mar 15	14.4
14	ABELL 0133	1	2203	15.672	-21.878	2000 Oct 13	35.5
		2	3183	15.670	-21.878	2002 Jun 24	44.5
		3	3710	15.670	-21.878	2002 Jun 26	44.6
		4	9897	15.674	-21.881	2008 Aug 29	69.2
		5	12177	15.453	-22.062	2010 Aug 31	50.1
		6	12179	15.735	-22.141	2010 Sep 03	51.1
		7	12178	15.999	-22.002	2010 Sep 07	46.8
		8	13391	15.757	-22.233	2011 Aug 16	46.4
		9	13442	15.350	-21.818	2011 Aug 23	176.7
		10	13443	15.359	-21.812	2011 Aug 26	69.7
14	ABELL 0133	11	14333	15.774	-21.613	2011 Aug 31	134.8
		12	13445	15.514	-22.193	2011 Sep 02	65.2
		13	13444	15.774	-21.613	2011 Sep 03	38.3
		14	13449	15.424	-21.662	2011 Sep 06	68.2
		15	13447	15.983	-21.744	2011 Sep 08	69.1
		16	13446	15.480	-21.587	2011 Sep 09	58.4
		17	14338	15.480	-21.587	2011 Sep 10	117.5
		18	14343	15.993	-21.710	2011 Sep 12	35.3
		19	13448	15.993	-21.710	2011 Sep 13	146.1
		20	13392	15.639	-21.563	2011 Sep 16	49.9
		21	13451	15.947	-22.196	2011 Sep 16	70.1
		22	13518	15.739	-21.901	2011 Sep 17	49.6
		23	13454	16.030	-21.897	2011 Sep 19	91.8
		24	14346	16.030	-21.897	2011 Sep 21	85.9
		25	14345	15.322	-22.089	2011 Sep 23	33.7
		26	13452	15.322	-22.089	2011 Sep 24	142.1
		27	13450	15.975	-22.161	2011 Oct 05	108.2
		28	14347	15.975	-22.161	2011 Oct 09	68.7
		29	14354	15.635	-22.148	2011 Oct 10	38.6
		30	13453	15.841	-21.604	2011 Oct 13	69.0

Table C.2: *Continued.*

ID	Cluster		ObsID[a]	R.A.[b] [J2000.0]	Decl.[b] [J2000.0]	Date[c]	Exposure[d] [ksec]
14	ABELL 0133	31	13456	15.635	-22.148	2011 Oct 15	135.6
		32	13455	15.983	-21.916	2011 Oct 19	69.6
		33	13457	15.341	-22.086	2011 Oct 21	69.1
15	ABELL S1101	1	1668	348.493	-42.726	2001 Aug 13	10.0
		2	11758	348.494	-42.728	2009 Aug 24	97.7
16	ABELL 2256	1	1386	256.045	78.631	1999 Oct 13	12.4
		2	965	256.045	78.631	1999 Oct 14	11.0
		3	1521	256.045	78.631	2000 Feb 27	3.0
		4	2419	256.045	78.631	2001 Feb 06	12.0
17	ABELL 1831	1	12283	209.820	27.981	2011 Apr 19	9.9
18	ABELL 1795	1	494	207.220	26.591	1999 Dec 20	19.5
		2	493	207.220	26.591	2000 Mar 21	19.6
		3	5286	207.220	26.591	2004 Jan 14	14.3
		4	5287	207.220	26.591	2004 Jan 14	14.3
		5	5288	207.220	26.591	2004 Jan 16	14.6
		6	5289	207.220	26.591	2004 Jan 18	15.0
		7	5290	207.220	26.591	2004 Jan 23	15.0
		8	6159	207.220	26.591	2005 Mar 20	14.9
		9	6160	207.220	26.591	2005 Mar 20	14.8
		10	6161	207.220	26.591	2005 Mar 28	13.6
		11	6162	207.220	26.591	2005 Mar 28	13.6
		12	6163	207.220	26.591	2005 Mar 31	14.9
		13	10432	207.366	26.459	2009 Mar 16	5.1
		14	10433	207.048	26.743	2009 Mar 23	5.1
		15	10900	207.220	26.591	2009 Apr 20	15.8
		16	10901	207.220	26.591	2009 Apr 20	15.5
		17	10898	207.220	26.591	2009 Apr 20	15.7
		18	10899	207.220	26.591	2009 Apr 22	14.9
		19	12027	207.220	26.591	2010 Mar 16	14.9
		20	12029	207.220	26.591	2010 Apr 28	14.7
		21	12028	207.220	26.591	2010 May 10	15.0
		22	12026	207.220	26.591	2010 May 11	14.9
		23	13108	207.220	26.591	2011 Mar 10	14.9
		24	13109	207.220	26.591	2011 Mar 11	14.6
		25	13110	207.220	26.591	2011 Mar 11	14.6
		26	13112	207.220	26.591	2011 Mar 11	14.6
		27	13113	207.220	26.591	2011 Mar 11	14.6
		28	13111	207.220	26.591	2011 Mar 11	14.6
		29	13106	207.220	26.591	2011 Apr 01	9.9
		30	13107	207.220	26.591	2011 Apr 01	9.6
		31	13412	207.219	26.591	2011 May 22	14.9
		32	13413	207.219	26.591	2011 May 29	14.9
		33	13414	207.219	26.591	2011 May 29	14.6
		34	13415	207.219	26.591	2011 May 29	14.6
		35	13416	207.220	26.591	2011 May 30	14.6
		36	13417	207.219	26.591	2011 Jun 02	14.9
		37	14270	207.220	26.591	2012 Mar 25	14.3
		38	14271	207.220	26.591	2012 Mar 25	14.0
		39	14272	207.220	26.591	2012 Mar 25	14.6
		40	14273	207.220	26.591	2012 Mar 26	14.6

Table C.2: *Continued.*

ID	Cluster		ObsID[a]	R.A.[b] [J2000.0]	Decl.[b] [J2000.0]	Date[c]	Exposure[d] [ksec]
18	ABELL 1795	41	14268	207.220	26.591	2012 Mar 26	9.9
		42	14274	207.220	26.591	2012 Apr 02	14.9
		43	14275	207.220	26.591	2012 Apr 07	14.9
		44	14269	207.220	26.591	2012 Apr 08	9.9
		45	15485	207.220	26.591	2000 Jun 06	9.9
		46	15486	207.220	26.591	2013 Apr 22	9.7
		47	15488	207.220	26.591	2013 Apr 10	14.6
		48	15489	207.220	26.591	2013 Apr 08	14.6
		49	15490	207.220	26.591	2013 Apr 17	14.9
19	ABELL 3112	1	2216	49.490	-44.238	2001 May 24	7.3
		2	2516	49.490	-44.238	2001 Sep 15	16.9
		3	6972	49.490	-44.238	2006 Apr 18	29.8
		4	7323	49.490	-44.238	2006 Apr 21	28.4
		5	7324	49.490	-44.238	2006 Apr 23	25.4
		6	13135	49.490	-44.238	2011 Mar 14	42.3
20	ZwCl 1742.1+3306	1	11708	266.060	32.991	2009 Nov 26	45.4
21	ABELL 2029	1	891	227.734	5.744	2000 Apr 12	19.8
		2	4977	227.734	5.744	2004 Jan 08	77.9
		3	6101	227.734	5.745	2004 Dec 17	9.9
		4	10434	227.576	5.897	2009 Apr 01	5.1
		5	10435	227.860	5.897	2009 Apr 01	4.7
		6	10436	227.576	5.615	2009 Apr 01	4.7
		7	10437	227.860	5.615	2009 Apr 01	4.7
22	ABELL 2495	1	12876	342.600	10.899	2010 Dec 23	7.9
23	ABELL 2061	1	10449	230.352	30.652	2009 Nov 17	31.4
24	ABELL 2255	1	894	258.173	64.069	2000 Oct 20	39.4
		2	7690	258.173	64.069	2007 Jul 02	5.1
25	ABELL 2249	1	12284	257.424	34.424	2010 Nov 14	9.9
26	ZwCl 0040.8+2404	1	11735	10.967	24.406	2009 Sep 06	19.8
27	ABELL 2597	1	922	351.332	-12.124	2000 Jul 28	39.4
		2	6934	351.332	-12.124	2006 May 01	52.2
		3	7329	351.332	-12.124	2006 May 04	60.1
28	ABELL 2142	1	1196	239.582	27.229	1999 Aug 20	11.4
		2	1228	239.582	27.229	1999 Aug 20	12.1
		3	5005	239.563	27.245	2005 Apr 13	44.6
		4	7692	239.585	27.246	2007 May 07	5.0
29	ABELL 2244	1	4179	255.678	34.060	2003 Oct 10	57.0
		2	7693	255.678	34.060	2007 Jul 27	5.1
30	PKS 0745-19	1	1383	116.880	-19.294	1999 Oct 11	8.9
		2	510	116.880	-19.294	1999 Oct 14	45.3
		3	1509	116.880	-19.294	2000 Mar 04	39.4
		4	508	116.880	-19.296	2000 Aug 28	28.0
		5	2427	116.880	-19.294	2001 Jun 16	17.9
		6	6103	116.882	-19.296	2004 Sep 24	10.3
		7	12881	116.880	-19.294	2011 Jan 27	118.1
31	ABELL 1068	1	1652	160.185	39.953	2001 Feb 04	26.8
		2	13598	159.872	39.934	2012 Mar 13	5.0
32	ABELL 1413	1	537	178.826	23.408	2000 Jun 23	9.6
		2	1661	178.826	23.408	2001 May 16	9.7
		3	5003	178.825	23.405	2004 Mar 06	75.1

Table C.2: *Continued.*

ID	Cluster		ObsID[a]	R.A.[b] [J2000.0]	Decl.[b] [J2000.0]	Date[c]	Exposure[d] [ksec]
32	ABELL 1413	4	5002	178.790	23.513	2005 Feb 03	36.7
		5	12195	179.114	23.459	2011 Feb 06	5.0
		6	12194	178.845	23.708	2012 Feb 19	5.0
		7	12196	178.566	23.457	2012 Feb 19	4.7
		8	13128	178.856	23.156	2012 Feb 25	5.0
		9	7696	178.825	23.405	2007 Jul 10	5.1
33	ABELL 3364	1	9419	86.907	-31.874	2008 Jul 04	19.8
34	ABELL 2204	1	499	248.196	5.576	2000 Jul 29	10.1
		2	6104	248.197	5.576	2004 Sep 20	9.6
		3	7940	248.197	5.576	2007 Jun 06	77.1
		4	12898	248.057	5.360	2011 Jan 13	5.0
		5	12897	248.403	5.432	2011 Jun 06	5.0
		6	12896	248.043	5.687	2011 Jul 16	5.0
		7	12895	248.342	5.781	2012 Jan 12	5.0
35	ABELL 2104	1	895	235.029	-3.290	2000 May 25	49.2
36	ABELL 1914	1	542	216.509	37.835	1999 Nov 21	8.1
		2	3593	216.505	37.828	2003 Sep 03	18.9
		3	12197	216.407	37.594	2010 Sep 09	4.7
		4	12892	216.172	37.897	2011 Oct 31	5.0
		5	12894	216.574	38.086	2011 Nov 25	5.0
		6	12893	216.823	37.757	2011 Dec 04	5.0
37	ABELL 2218	1	553	248.983	66.212	1999 Oct 19	5.9
		2	1454	248.983	66.212	1999 Oct 19	11.4
		3	1666	248.970	66.214	2001 Aug 30	48.6
		4	7698	248.970	66.214	2007 Jun 13	5.1
38	ABELL 0665	1	531	127.739	65.854	1999 Dec 29	9.0
		2	3586	127.722	65.834	2002 Dec 28	29.7
		3	13201	127.747	65.841	2011 Jan 06	48.7
		4	12286	127.747	65.841	2011 Jan 09	47.1
		5	7700	127.749	65.841	2006 Dec 30	5.1
39	ABELL 1689	1	540	197.873	-1.336	2000 Apr 15	10.3
		2	1663	197.873	-1.336	2001 Jan 07	10.7
		3	5004	197.873	-1.341	2004 Feb 28	19.9
		4	6930	197.873	-1.342	2006 Mar 06	76.1
		5	7289	197.873	-1.342	2006 Mar 09	75.1
		6	7701	197.874	-1.342	2007 Mar 07	5.0
40	ABELL 0383	1	2320	42.013	-3.528	2000 Nov 16	19.3
		2	2321	42.013	-3.528	2000 Nov 16	19.5
		3	524	42.013	-3.528	2000 Sep 08	10.0
41	ABELL 1246		11770	170.995	21.480	2009 Oct 30	5.0
42	ABELL 2163	1	545	243.941	-6.149	2000 Jul 29	9.5
		2	1653	243.941	-6.149	2001 Jun 16	71.2
		3	2455	243.979	-6.450	2001 Jun 17	8.7
43	ABELL 0963	1	903	154.264	39.048	2000 Oct 11	36.3
		2	7704	154.264	39.048	2007 Feb 18	5.1
44	ABELL 0773	1	533	139.472	51.727	2000 Sep 05	11.3
		2	3588	139.471	51.729	2003 Jan 25	9.4
		3	5006	139.471	51.729	2004 Jan 21	19.8
		4	13592	139.697	51.527	2012 Feb 09	5.0
45	ABELL 2219	1	896	250.100	46.710	2000 Mar 31	42.3

Table C.2: *Continued.*

ID	Cluster		ObsID[a]	R.A.[b] [J2000.0]	Decl.[b] [J2000.0]	Date[c]	Exposure[d] [ksec]
45	ABELL 2219	2	7892	250.085	46.708	2007 Sep 27	5.1
46	ABELL 2390	1	501	328.402	17.696	1999 Nov 05	9.1
		2	500	328.402	17.696	2000 Oct 08	9.8
		3	4193	328.403	17.696	2003 Sep 11	95.1
47	ABELL 2667	1	2214	357.913	-26.084	2001 Jun 19	9.7
48	ABELL 1835	1	495	210.258	2.878	1999 Dec 11	19.5
		2	496	210.258	2.878	2000 Apr 29	10.7
		3	49896	210.258	2.859	2000 Aug 25	9.7
		4	511	210.258	2.859	2000 Aug 26	125.3
		5	6880	210.259	2.879	2006 Aug 25	117.9
		6	6881	210.259	2.879	2005 Dec 07	36.3
48	ABELL 1835	7	7370	210.259	2.879	2006 Jul 24	39.5
49	SDSS CE J355.9	1	5786	355.915	0.328	2005 Oct 17	29.8
50	ABELL 2537	1	4962	347.092	-2.192	2004 Sep 09	36.2
		2	9372	347.092	-2.191	2008 Aug 11	38.5
51	Bullet Cluster	1	554	104.658	-55.950	2000 Oct 16	25.8
		2	3184	104.582	-55.939	2002 Jul 12	87.5
		3	5355	104.583	-55.942	2004 Aug 10	27.4
		4	5356	104.583	-55.942	2004 Aug 11	97.2
		5	5357	104.583	-55.942	2004 Aug 14	79.1
		6	5358	104.583	-55.942	2004 Aug 15	32.0
		7	5361	104.583	-55.942	2004 Aug 17	82.6
		8	4984	104.583	-55.942	2004 Aug 19	76.1
		9	4985	104.583	-55.942	2004 Aug 23	27.5
		10	4986	104.583	-55.942	2004 Aug 25	41.5
52	ABELL 2744	1	2212	3.554	-30.378	2001 Sep 03	24.8
		2	7915	3.581	-30.392	2006 Nov 08	18.6
		3	8477	3.581	-30.392	2007 Jun 10	45.9
		4	8557	3.581	-30.392	2007 Jun 14	27.8
		5	7712	3.580	-30.385	2007 Sep 10	8.1
53	MS 1512.4+3647	1	800	228.593	36.607	2000 Jun 06	
54	LCDCS 0829	1	506	206.879	-11.753	2000 Mar 05	8.9
		2	507	206.879	-11.753	2000 Apr 29	10.0
		3	2222	206.879	-11.753	2001 May 10	92.7
		4	3592	206.879	-11.754	2003 Sep 03	57.7
		5	13999	206.879	-11.754	2012 May 14	54.4
		6	14407	206.879	-11.754	2012 Mar 16	63.2
55	MACS J0717+3745	1	4200	109.379	37.758	2003 Jan 08	59.0
		2	1655	109.379	37.761	2001 Jan 29	19.9
56	SPT-CL J2337-5942	1	11859	354.355	-59.708	2010 Jan 10	19.8
57	SPT-CL J2341-5119	1	11799	355.287	-51.321	2009 Aug 01	50.3
		2	9345	355.287	-51.321	2009 Aug 02	29.6
58	SPT-CL J0546-5345	1	9332	86.650	-53.756	2009 Jan 09	14.9
		2	10851	86.650	-53.756	2009 Feb 01	8.5
		3	10864	86.650	-53.756	2009 Feb 04	5.8
		4	9336	86.650	-53.756	2009 May 04	28.2
		5	11739	86.650	-53.756	2010 Jul 04	12.8

[a] *Chandra* observation identifier.
[b] Nominal pointing position of the observation in Equinox 2000.0.
[c] Start time of the observation in universal time coordinated.
[d] Cleaned exposure time of each observation.

Bibliography

[1] Abell, G. O. 1958, ApJS, 3, 211

[2] Abell, G. O., Corwin, H. G. Jr., & Olowin, R. P. 1989, ApJS, 70, 1

[3] Akamatsu, H., Hoshino, A., Ishisaki, Y., Ohashi, T., Sato, K., Takei, Y., & Ota, N. 2011, PASJ, 63, S1019

[4] Anders, E., & Ebihara, M. 1982, Metic, 17, 180

[5] Anders, E., & Grevesse, N. 1989, Geochim. Cosmochim. Acta, 53, 197

[6] Anderson, M. E., Bregman, J. N., Butler, S. C., & Mullis, C. R. 2009, ApJ, 698, 317

[7] Arimoto, N. & Yoshii, Y. 1987, A&A, 173, 23

[8] Arnaboldi, M. 2004, IAUS, 217, 54

[9] Arnaud, M., Rothenflug, R., Boulade, O., Vigroux, L., & Vangioni-Flam, E. 1992, A&A, 254, 49

[10] Aschenbach, B. 1985, RPPh, 48, 579

[11] Baldi, A., Ettori, S., Molendi, S., Balestra, I., Gastaldello, F., & Tozzi, P. 2012, A&A, 537, 1

[12] Balestra, I., Tozzi, P., Ettori, S., Rosati, P., Borgani, S., Mainieri, V., Norman, C., & Viola, M. 2007, A&A, 462, 429

[13] Baumgartner, W. H., Loewenstein, M., Horner, D. J., & Mushotzky, R. F. 2005, ApJ, 620, 680

[14] Bautz, L. P., Morgan, W. W. 1970, ApJ, 162, 149

[15] Blanton, M. R., et al. 2003, ApJ, 592, 819

[16] Borgani, S., Fabjan, D., Tornatore, L., Schindler, S., Dolag, K., & Diaferio, A. 2008, Space Sci. Rev., 134, 379

[17] Burns, J. O., Hallman, E. J., Gantner, B., Motl, P. M., & Norman, M. L. 2008, ApJ, 675, 1125

[18] Byram, E. T., Chubb, T. A., & Friedman, H. 1966, AJ, 71, 379

[19] Chartas, G., Brandt, W. N., Gallagher, S. C., & Garmire, G. P. 2002, ApJ, 579, 169

[20] Chen, Y., Reiprich, T. H., Bohringer, H., Ikebe, Y., & Zhang, Y.-Y. 2007, A&A, 466, 805

[21] Chilingarian, I. V., Melchior, A.-L., & Zolotukhin, I. Y. 2010, MNRAS, 405, 1409

[22] Chilingarian, I. V., & Zolotukhin, I. Y. 2012, MNRAS, 419, 1727

[23] Clemens, M. S., Alexander, P., & Green, D. A. 2000, MNRAS, 312, 236

[24] Cora, S. A., Tornatore, L., Tozzi, P., & Dolag, K. 2008, MNRAS, 96

[25] Crenshaw, D. M., Kraemer, S. B., & Gabel, J. R. 2003, AJ, 126, 1690

[26] De Grandi, S., Ettori, S., Longhetti, M., & Molendi, S. 2004, A&A, 419, 7

[27] de Plaa, J., Werner, N., Bleeker, J. A. M., Vink, J., Kaastra, J. S., & M'endez, M. 2007, A&A, 465, 345

[28] De Young, D. S. 1986, ApJ, 307, 62

[29] Dickey, J. M., & Lockman, F. J. 1990, ARA&A, 28, 215

[30] Dressler, A. 1980, ApJ, 236, 351

[31] Elbaz, D, & Cesarsky, C. J. 2003, Sci, 300, 270

[32] Esquej, P. 2012, MNRAS, 423, 185

[33] Ezawa, H., Fukazawa, Y., Makishima, K., Ohashi, T., Takahara, F., Xu, H., & Yamasaki, N. Y. 1997, ApJ, 490, L33

[34] Fabjan, D., Tornatore, L., Borgani, S., Saro, A., & Dolag, K. 2008, MNRAS, 386, 1265

[35] Fields, D. L., Mathur, S., Krongold, Y., Williams, R., & Nicastro, F. 2007, ApJ, 666, 828

[36] Finoguenov, A., Arnaud, M., & David, L. P. 2001, ApJ, 555, 191

[37] Finoguenov, A., David, L. P., & Ponman, T. J. 2000, ApJ, 544, 188

[38] Frank, K. A., Peterson, J. R., Andersson, K., Fabian, A. C., & Sanders, J. S. 2013, ApJ, 764, 46

[39] Freeman, P. E., Kashyap, V., Rosner, R., & Lamb, D. Q. 2002, ApJS, 138, 185

[40] Fukazawa, Y., Ohashi, T., Fabian, A. C., Canizares, C. R., Ikebe, Y., Makishima, K., Mushotzky R. F., & Yamashita, K. 1994, PASJ, 46, L55

[41] Fukazawa, Y., Makishima, K., Tamura, T., Ezawa, H., Xu, H., Ikebe, Y., Kikuchi, K., & Ohashi, T. 1998, PASJ, 50, 187

[42] Fukazawa, Y., Makishima, K., Tamura, T., Nakazawa, K., Ezawa, H., Ikebe, Y., Kikuchi, K., & Ohashi, T. 2000, MNRAS, 313, 21

[43] Gal-Yam, A., Maoz, D., & Sharon, K. 2002, MNRAS, 332, 37

[44] Goto, T., et al. 2002, PASJ, 54, 515

[45] Grevesse, N. & Sauval, A. J. 1998, Space Science Reviews, 85, 161

[46] Gu, L., Yagi, M., Nakazawa, K., Yoshida, M., Fujita, Y., Hattori, T., Akahori, T., & Makishima, K. 2013, ApJ, 777, 36

[47] Gunn, J. E., & Gott, J. R., III 1972, ApJ, 176, 1

[48] Hasinger, G., Schartel, N., & Komossa, S. 2002, 573, 77

[49] Hayashida, K. 1989, PhD thesis, The University of Tokyo

[50] Henry, J. P., Evrard, A. E., Hoekstra, H., Babul, A. & Mahdavi, A. 2009, ApJ, 691, 1307

[51] Hoshino, A., et al. 2010, PASJ, 62, 371

[52] Hudson, D. S., Mittal, R., Reiprich, T. H., Nulsen, P. E. J., Andernach, H., & Sarazin, C. L. 2010, A&A, 513, 37

[53] Ishisaki, Y., et al. 2007, PASJ, 59, S113

[54] Iwamoto, K., Brachwitz, F., Nomoto, K., Kishimoto, N., Umeda, H., Hix, W. R., & Thilemann, F.-K. 1999, ApJS, 125, 439

[55] Jones, C. & Forman, W. 1984, ApJ, 38

[56] Kaastra, J. S. & Mewe, R. 1993, A&A, 97, 443

[57] Kawaharada, 2006, PhD thesis, The University of Tokyo

[58] Kawaharada, M., et al. 2010, ApJ, 714, 423

[59] Kelley, R. L., et al. 2007, PASJ, 59, 77

[60] King, I. 1962, AJ, 67, 471

[61] Kokubun, M., et al. 2007, PASJ, 59, 53

[62] Komiyama, M., Sato, K., Nagino, R., Ohashi, T., & Matsushita, K. 2009, PASJ, 61, S337

[63] Koyama, K., et al. 2007, PASJ, 59, S23

[64] Koyama, K., Takano, S., & Tawara, Y. 1991, Nature, 350, 135

[65] Kushino, A., Ishisaki, Y., Morita, U., Yamasaki, N. Y., Ishida, M., Ohashi, T., & Ueda, Y. 2002, PASJ, 54, 327

[66] Leccardi, A., & Molendi, S. 2008, A&A, 487, 461

[67] Lodders, K. 2003, ApJ, 591, 1220

[68] Loewenstein, M. 2006, ApJ, 648, 230

[69] Lumb, D. H., Warwick, R. S., Page, M., & De Luca, A. 2002, A&A, 389, 93

[70] Mannucci, F., Della Valle, M., & Panagia, N. 2006, MNRAS, 370, 773

[71] Maoz, D., Mannucci, F., & Brandt, T. D. 2012, MNRAS, 426, 3282

[72] Mathews, W. G., & Baker, J. C. 1971, ApJ, 170, 241

[73] Matsushita, K., et al. 2007, PASJ, 59, S327

[74] Matteucci, F. 1994, A&A, 288, 57

[75] Maughan, B. J., Jones, C., Forman, W., & Van Speybroeck, L. 2008, ApJS, 174, 117

[76] Mihos, J. C., Harding, P., Feldmeier, J., & Morrison, H. 2005, ApJ, 631, 41

[77] Mitchell, R. J., Culhane, J. L., Davison, P. J. N., & Ives, J. C. 1976, 175, 29

[78] Mitsuda, K., et al. 2007, PASJ, 59, S1

[79] Mittal, R., Hudson, D. S., Reiprich, T. H., & Clarke, T. 2009, A&A, 501, 835

[80] Mohr, J. J., Mathiesen, B., & Evrard, A. E. 1999, ApJ, 517, 627

[81] Murakami, H., Komiyama, M., Matsushita, K., Nagino, R., Sato, T., Sato, K., Kawaharada, M., Nakazawa, K., Ohashi, T., & Takei, Y. 2011, PASJ, 63, S963

[82] Nagashima, M., Lacey, C. G., Baugh, C. M., Frenk, C. S., & Cole, S. 2005, MNRAS, 358, 1247

[83] Nakamura, T., Umeda, H., Iwamoto, K., Nomoto, K., Hashimoto, M., Hix, W., R., & Thielemann F.-K. 2001, ApJ, 555, 880

[84] Nakazawa, K., et al. 2009, PASJ, 61, 339

[85] Nesvadba, N. P. H., Lehnert, M. D., Eisenhauer, F., Gilbert, A., Tecza, M., & Abuter, R. 2006, ApJ, 650, 693

[86] Nomoto, K., Tominaga, N., Umeda, H., Kobayashi, C., & Maeda, K. 2006, Nucl. Phys. A, 777, 424

[87] Okabe, N., & Umetsu, K. 2008, PASJ, 60, 345

[88] Okumura, Y., Tsunemi, H., Yamashita, K., Matsuoka, M., Koyama, K., Hayakawa, S., Masai, K., & Hughes, J. P. 1988, PASJ, 40, 639

[89] Ota, N. 2000, PhD thesis, The University of Tokyo

[90] Pipino, A., & Matteucci, F. 2004, MNRAS, 347, 968

[91] Planck Collaboration 2011a, A&A, 536, 1

[92] Planck Collaboration 2011b, A&A, 536, 11

[93] Raymond, J. S. & Smith, B. W. 1977, ApJS, 35, 419

[94] Renzini, A., Ciotti, L., D 'Ercole, A., & Pellegrini, S. 1993, ApJ, 419, 52

[95] Rybicki, G. B. & Lightman, A. P. 1979, New York, Wiley-Interscience

[96] Sakuma, E., Ota, N., Sato, K., Sato, T., & Matsushita, K. 2011, PASJ, 63, S979

[97] Salpeter, E. E. 1955, ApJ, 121, 161

[98] Sarazin, C. L. 1988, X-ray emission from clusters of galaxies, Cambridge university press

[99] Sato, K. 2007, PhD thesis, Tokyo Metropolitan University

[100] Sato, K., et al. 2007a, PASJ, 59, 299

[101] Sato, K., Kawaharada, M., Nakazawa, K., Matsushita, K., Ishisaki, Y., Yamasaki, N. Y., & Ohashi, T. 2010, PASJ, 62, 1445

[102] Sato, K., Matsushita, K., & Gastaldello, F. 2009b, PASJ, 61, S365

[103] Sato, K., Matsushita, K., Ishisaki, Y., Yamasaki, N. Y., Ishida, M., & Ohashi, T. 2009a, PASJ, 61, S353

[104] Sato, K., Matsushita, K., Ishisaki, Y., Yamasaki, N. Y., Ishida, M., Sasaki, S., & Ohashi, T. 2008, PASJ, 60, S333

[105] Sato, K., Tokoi, K., Matsushita, K., Ishisaki, Y., Yamasaki, N. Y., Ishida, M., & Ohashi, T. 2007b, ApJ, 667, L41

[106] Schechter, P. 1976, ApJ, 203, 297

[107] Serlemitsos, P. J., et al. 2007, PASJ, 59, S9

[108] Shimoda, Y., Kawaharada, M., Sato, K., Ohashi, T., Ishisaki, Y., Mitsuishi, I., Akamatsu, H., & Tashiro, M. S. 2013, PASJ, 65, 111

[109] Smith, R. K., Brickhouse, N. S., Liedahl, D. A., & Raymond, J. C. 2001, ApJ, 556, L91

[110] Snowden, S. L., Mushotzky, R. F., Kuntz, K. D., & Davis, D. S. 2008, A&A, 478, 615

[111] Strolger, L.-G., et al. 2004, ApJ, 613, 200

[112] Sutherland, R. S. & Dopita, M. A. 1993, ApJS, 88, 253

[113] Takahashi, T., et al. 2007, 59, 35

[114] Tamura, T., Maeda, Y., Mitsuda, K., Fabian, A. C., Sanders, J. S., Furuzawa, A., Hughes, J. P., Iizuka, R., Matsushita, K., & Tamagawa, T. 2009, ApJ, 705, 62

[115] Tanaka, Y., Inoue, H., & Holt, S. S. 1994, PASJ, 46, L37

[116] Tauber, J. A., et al. 2010, A&A, 520, 1

[117] Tawa, N., et al. 2008, PASJ, 60, S11

[118] Tokoi, K., et al. 2008, PASJ, 60, S317

[119] Travaglio, C., Hillebrandt, W., Reinecke, M., & Thielemann, F.-K. 2004, A&A, 425, 1029

[120] Veilleux, S., Cecil, G., & Bland-Hawthorn, J. 2005, 43, 769

[121] Vikhlinin, A., Kravtsov, A., Forman, W., Jones, C., Markevitch, M., Murray, S. S., & Van Speybroeck, L. 2006, ApJ, 640, 691

[122] Weisskopf, M. C., Brinkman, B., Canizares, C., Garmire, G., Murray, S., & Van Speybroeck, L. P. 2002, PASP, 114, 1

[123] Wolf, M. 1906, Astron. Nachr, 170, 211

[124] Xu, H., Makishima, K., Fukazawa, Y., Ikebe, Y., Kikuchi, K., Ohashi, T., & Tamura, T. 1998, ApJ, 500, 738

[125] Yoshino, T., et al. 2009, PASJ, 61, 805

[126] Zubovas, K., Nayakshin, S., King, A., & Wilkinson, M. 2013, MNRAS, 433, 3079

[127] Zwicky, F., Herzog, E., Wild, P., Karpowicz, M., & Kowal, C. T. 1961–1968, CGCG, Vols. 1–6

ACKNOWLEDGEMENT

First of all, I would like to express my best gratitude to Prof. Makoto Tashiro for his continuous support, leading and encouragement throughout the five years of my graduate course. I also deeply appreciate Dr. Madoka Kawaharada (ISAS/JAXA) for his continuous advice and cooperation. I would like to thank my collaborators: Prof. Takaya Ohashi, Prof. Yoshitaka Ishisaki (Tokyo Metropolitan Univ.), Dr. Kosuke Sato (Tokyo Univ. of Science), Dr. Hiroki Akamatsu (SRON), Dr. Ikuyuki Mitsuishi (Tokyo Metropolitan Univ.), Dr. Nobuhiro Okabe (IPMU).

I thank all the *Suzaku* and *Chandra* team members for their support of these two projects. This research has made use of the NASA/IPAC Extragalactic Database (NED) which is operated by the Jet Propulsion Laboratory, California Institute of Technology, under contract with the National Aeronautics and Space Administration. Funding for SDSS-III has been provided by the Alfred P. Sloan Foundation, the Participating Institutions, the National Science Foundation, and the U.S. Department of Energy Office of Science. The SDSS-III web site is http://www.sdss3.org/. This research made use of the "K-corrections calculator" service available at http://kcor.sai.msu.ru/. This work is financially supported by Grant-in-Aid for Japan Society for the Promotion of Science Fellows, the Hayakawa Satio Foundation, and the fellowship researcher program of ISAS/JAXA.

I wish to thank all the members, past and present of our laboratory. I particularly appreciate following members: Dr. Akira Endo, he taught palatability of sake to me; Dr. Hiromi Seta, she is my teacher of *Suzaku* analysis and experiment of PSP onboard *ASTRO-H* satellite; Dr. Wataru Iwakiri, he lent me a lot of CDs of folk songs; Dr. Tomomi Kouzu and Dr. Atsushi Harayama, they organized many drinking parties in spite of my final grade of doctoral course; Tetsuya Yasuda, Sawako Takeda, and Sunao Yamaguchi, I will never forget the travels to Komaki and Taiwan for Yasuda, United States for Takeda, and Germany and United States for Yamaguchi.

I also thank to the all PSP team members and the SXS team members. I could be wonderful experiences: Shimanami-kaido cycling, spectate of major leagues, band sessions with Kevin and Rich's band, Yakiniku party every night, and so on.

I want to thank all my friends of department of physics and all members of tea ceremony club. I could spend great time for nine years at Saitama university. I particularly thank Takashi Iino, I never forget our session of the guitar and talking about the rock music. Are you enjoying to play the guitar in the heaven?

Finally, I thank my father, mother, sisters, and my nieces, Kia, Shinki, and Anna, who always allay my fatigue. I also thank wonderful starry sky.